

國 立 交 通 大 學

土 木 工 程 學 系

博 士 論 文

台灣超導及絕對重力觀測：重力基準、地體動力
及環境變遷之應用

**Superconducting and absolute gravity observations in
Taiwan: applications to gravity datum, geodynamics
and environmental change**

研究生：高瑞其

指導教授：黃金維

中華民國一〇〇年七月

Superconducting and absolute gravity observations in Taiwan: applications to gravity datum, geodynamics and environmental change

Student : Ruei-Chi Kao (Ricky Kao)

Advisor : Cheinway Hwang

Abstract

The superconducting gravity (SG) and absolute gravity (AG) observatory in Hsinchu (identified as HS) joined the Global Geodynamics Project (GGP) since 2006. This study is focused on the analysis of gravity datum, geodynamics and environmental change in Taiwan. Most experiments of SG, AG and global positioning system (GPS) are conducted over Taiwan and at HS. Solid and ocean tide gravity effects are estimated from five years of SG data and are compared with models. The performance of HS SG is assessed by comparison of the gravity spectra at HS and at other SG stations. To compare the spectra of residual gravity is from several continuously recording SG stations. We model the gravity variations of non-tectonic origins due to atmosphere, hydrology, and polar motion. The calibration factor (CF) and drifting rate of T48 are $76.087 \pm 0.067 \mu\text{gal voltage}^{-1}$ and $1.3 \pm 0.1 \mu\text{gal year}^{-1}$ ($1 \mu\text{gal} = 10^{-8} \text{ms}^{-2}$). Based on the GPS measuring results, the horizontal rates of plate motion in southeastern Taiwan are about $7\text{-}8 \text{cm year}^{-1}$. A joint Taiwan-France project, called Absolute Gravity for Taiwanese Orogen (AGTO), was initiated in 2006 to study the orogeny of Taiwan using gravimetry and GPS. AGTO measurements show that the average gravity and GPS vertical rate are $-1.39 \pm 4.21 \mu\text{gal year}^{-1}$ and $0.50 \pm 0.94 \text{cm year}^{-1}$, respectively, leading to an average gravity-height ratio ($2.78 \mu\text{gal cm}^{-1}$). Large

(in absolute magnitude) gravity-atmosphere admittances are found during major typhoons. The direct Newtonian and elastic effects due to the atmospheric effects of Kalmaegi typhoon are modeled using the Green's function approach. Typhoon Morakot (August 2008) caused large landslides at AG3 and AG6 (two stations of AGTO) that created gravity changes of 53 μgal and 27 μgal , and sediment thickness changes of 2.45m and 1.25m.

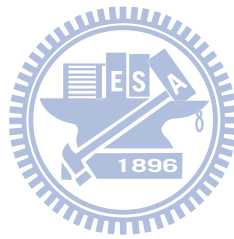


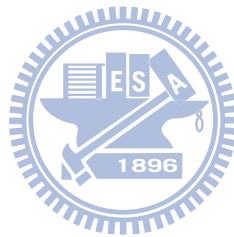
Table of Contents

Abstract	II
Table of Contents	IV
List of Tables	VII
List of Figures	VIII
Chapter 1 Introduction	1
1.1 Background	1
1.2 Literature Review	3
1.3 Outline of dissertation	4
Chapter 2 Principles of superconducting gravimeters and absolute gravimeters at LOGG	6
2.1 Superconducting gravimeter	6
2.1.1 Introduction	6
2.1.2 Observatory SG (OSG) sensor	7
2.1.3 Refrigeration System	9
2.1.4 Integrated electronics	10
2.1.5 User interface PC software	11
2.2 Absolute gravimeter	12
2.2.1 Introduction	12
2.2.2 Specifications of FG5	14
2.2.3 Gravity gradient for gravity reduction	16
2.2.4 Quality assessment of AG measurement	20
Chapter 3 Processing SG data	23
3.1 Filtering and decimation of raw SG data	23
3.2 Calibration factor	25
3.2.1 Estimation of calibration factor using the DDW model gravity	25

3.2.2 Calibration factor from parallel SG and AG gravity observations	27
3.3 Detided gravity	31
3.4 Sub-seismic noise levels of residual gravity from T48.....	33
Chapter 4: Analyses of tidal parameters and ocean tide loading gravity effects.....	35
4.1 Spectral analysis of SG gravity records.....	35
4.2 Tidal analysis.....	36
4.3 Ocean tide loading gravity effects	41
4.4 Comparison with theoretical solid earth tide.....	46
Chapter 5 Modeling temporal gravity changes of non-tectonic origins	50
5.1 Atmospheric pressure effect	50
5.2 Hydrological effect.....	52
5.3 Polar motion effect	52
5.4 Observations and models.....	53
5.5 Rate of gravity change at Hsinchu.....	55
Chapter 6 NGDS and gravity network in Taiwan.....	57
6.1 NGDS and its geological settings.....	57
6.2 An AG network in Taiwan and contribution to GGP.....	61
Chapter 7 Gravity changes from SG and AG in Taiwan.....	63
7.1 Estimation the drift of T48	63
7.2 Gravity changes from project AGTO.....	65
7.3 Gravity changes from MOI AG campaigns	71
Chapter 8 Gravity changes caused by typhoon and earthquake	80
8.1 Observed gravity effects due to typhoons.....	80
8.2 Interpretations of typhoon-induced gravity changes	82
8.2.1 Direct Newtonian effect.....	83
8.2.2 Indirect elastic effect	85
8.2.3 Global atmospheric effect	86



8.3 Observed co-seismic gravity changes due to earthquake.....	89
Chapter 9 Summary and future work.....	93
References	96
Appendix 1	101
Appendix 2	110
Curriculum Vitae	116



List of Tables

Table 2-1: Gravity gradients and standard errors at different times.....	18
Table 2-2: Absolute gravity measurements and result on B1 from FG5 #231 in 2010	21
Table 3-1: Amplitude factors and phases at HS based on DDW at HS	26
Table 3-2: Sessions of parallel superconducting (T48) and absolute (FG5) gravity observations for determining the calibration factor of T48	30
Table 5-1: Amplitudes and phases of the annual gravity change at HS by various factors	54
Table 5-2: Modeled and FG5-observed rates of gravity change (in $\mu\text{gal year}^{-1}$) at HS	56
Table 7-1: The Location of AG and GPS sites	67
Table 7-2: Gravity changes relative to observations in 2006	69
Table 7-3: Gravity changes relative to observations in 2006	71
Table 7-4: Gravity gradients at 15 MOI sites.....	72
Table 7-5: Absolute gravity values and uncertainties in 2005 and 2008 at MOI sites	72
Table 7-6: Rates of gravity change at MOI sites.....	73
Table 8-1: Gravity changes due to typhoons and gravity-atmosphere admittances at HS	81
Table 8-2: Gravity shifts due to earthquakes around Taiwan at HS (2006-2009).....	91

List of Figures

Fig. 1-1 Current and planned SG stations in the world, squares represent the new stations, circles the current stations, diamonds the planned stations (Described in the ggpnews20, 2010).....	2
Fig. 1-2 Layout of NGDS, T48 is installed at B2.....	3
Fig. 2-1 T48 at LOGG, showing the coldhead, integrated electronics with digital data acquisition system (DDAS) and user interface PC (UIPC) software.	7
Fig. 2-2 A cross section scheme of the T48 sensor (GWR, 2011).....	8
Fig. 2-3 Refrigeration system of Sumitomo CNA-11 helium compressor, and Sumitomo RDK-101E coldhead of T48	10
Fig. 2-4 integrated electronics and data acquisition system of T48	11
Fig. 2-5 The UIPC main page, showing 1-s (top panel) and 60-s real-time (grav1), filtered gravity (grav2) and barometer data (baro-1), GPS status, liquid helium status, DAC status and alarm status.....	12
Fig. 2-6 Principle of AG measurement by laser to detect distance and rubidium to detect time (FG5 Manual, 2006).....	13
Fig. 2-7 The schematic of a FG5 system. (FG5Manual, 2006).....	15
Fig. 2-8 Measuring gravity values at different heights for gradient determination.....	18
Fig. 2-9 Gravity gradients and standard errors (vertical bars), and the trends of gradient	19
Fig. 2-10 Gravity values (relative to the mean of all measurements) and standard errors (vertical bars) at pillar B1 observed by the FG5 #224 and #231 gravimeters...22	22
Fig. 3-1 The raw data before (top) and after (bottom) removing discontinuities and disturbances.	24
Fig. 3-2 Filter response functions of the low-pass (left) and high-pass (right) used in the LSQ filters of TSoft	25

Fig. 3-3 Gravity values based on DDW (Dehant et al., 1999) solid earth model from July 1, 2009 to September 30, 2009.....	26
Fig. 3-4 Gravity values converted from voltage records (T48) using the CF estimated with the DDW from July 1, 2009 to September 30, 2009 by Tsoft	27
Fig. 3-5 Four cases of estimating CF of T48 by FG5 #231	29
Fig. 3-6 Signal (top) and residual (bottom) from T48 during liquid helium loss. The residual gravity shows a clear drop associated with the helium loss.....	32
Fig. 3-7 Procedure of solid earth tide from (left), procedure of ocean tide loading (middle), procedure of observed (right) from T48.....	33
Fig. 3-8 Sub-seismic noise levels of residual gravity at HS station, compared with other SG stations (the names are defined on the GGP web page)	34
Fig. 4-1 Tidal spectra of raw gravity records in five years were recorded by T48. Two clusters are present at the semi-diurnal and diurnal wave bands. Tides with periods shorter than the period of M_3 are not shown here.....	35
Fig. 4-2 Comparison the raw gravity records and observed models of T48 and T49 in January 1, 2009.....	40
Fig. 4-3 Difference amplitudes from T48 and T49 (T49 minus T48).....	40
Fig. 4-4 Difference phases from T48 and T49 (T49 minus T48).	41
Fig. 4-5 Amplitudes of ocean tide from tide gauge records at the Hsinchu Harbor (8.6 km to HS), and amplitudes of ocean tide loading from the SG gravity measurements at HS	44
Fig. 5-1 Raw atmospheric pressure over 4/2006-12/2010 (left) and the distribution of the atmospheric pressure (right)	51
Fig. 5-2 Spectra of SG gravity (Red) and atmospheric pressure (Blue).....	51
Fig. 5-3 Observed residual gravity changes (by T48, without the solid earth tide and ocean tide gravity effects) and modeled gravity changes at HS. The time starts from	

April 2006.....	55
Fig. 6-1 Geological settings around the NGDS and distributions of GPS and tide gauge stations. The meanings of the formations are explained by documents in the Central Geological Survey of Taiwan.....	58
Fig. 6-2 A cross-section along the alluvium north of HS showing layers with shallow and deep groundwater. Deep groundwater takes time to fill and will delay groundwater-induced gravity change. The sampling points A, B, C, D and E are shown in Fig. 6-1	58
Fig. 6-3 The variations of coordinate are at the HCHM, TCMS, SHJU and HSIN permanent GPS stations. The numbers in the figure panels are linear rate of displacements from LSQ fits to the coordinate variations.....	60
Fig. 6-4 Absolute gravity sites in Taiwan established by MOI.....	62
Fig. 7-1 Comparison of SG and FG5 measurements are from 2006-2011. The FG5 gravimeter #228 is from France while #224 and #231 are from Taiwan.....	64
Fig. 7-2 AG sites in the project AGTO (circle) and GPS sites (star).....	66
Fig. 7-3 The elevation of AG sites in the project AGTO, AG3 and AG6 are located at the mid-slope of a mountain	67
Fig. 7-4 Formosat-2 images of AG3 and AG6 before and after Morakot.....	67
Fig. 7-5 Accumulation of soil and rock in the riverbed near AG6 due to Morakot (brown), and the original riverbed (green).....	68
Fig. 7-6 Gravity changes relative to observations in 2006 at AGTO sites (each curve represents a year)	70
Fig. 7-7 Gravity changes relative to the observations in 2006 at the AGTO sites (each curve represents a site).....	70
Fig. 7-8 Absolute gravity values and rate at DSIG	75
Fig. 7-9 Absolute gravity values and rate at FLNG.....	75

Fig. 7-10 Absolute gravity values and rate at HCHG	75
Fig. 7-11 Absolute gravity values and rate at JSIG	75
Fig. 7-12 Absolute gravity values and rate at KDNG.....	76
Fig. 7-13 Absolute gravity values and rate at LYUG	76
Fig. 7-14 Absolute gravity values and rate at PKGG	76
Fig. 7-15 Absolute gravity values and rate at SMLG	76
Fig. 7-16 Absolute gravity values and rate at TAES.....	77
Fig. 7-17 Absolute gravity values and rate at TCHG	77
Fig. 7-18 Absolute gravity values and rate at TLGG.....	77
Fig. 7-19 Absolute gravity rate of WFSG station	77
Fig. 7-20 Absolute gravity rate of YHEG station	78
Fig. 7-21 Absolute gravity values and rate at YLIG	78
Fig. 7-22 Absolute gravity values and rate at YMSG.....	78
Fig. 7-23 Two-dimensional (lateral) distribution of gravity rates interpolated from the rates at AG sites	79
Fig.7-24 Horizontal displacement rates (arrows) and vertical displacement rates (color) from GPS. An arrow corresponds to a continuous GPS station.....	79
Fig. 8-1 Weather sensor outputs during Typhoon Morakot (top) and SG gravity data in Hsinchu with and without atmospheric pressure effects.....	81
Fig. 8-2 Weather sensor outputs during Typhoon Kalmaegi (top) and SG gravity data in Hsinchu with and without atmospheric pressure effects.	82
Fig. 8-3 A plane view (left) and perspective view of the 3-D atmospheric pressure model for Morakot.....	87
Fig. 8-4 A plane view (left) and perspective view of the 3-D atmospheric pressure model for Kalmaegi	88
Fig. 8-5 Atmospheric gravity effects of Typhoon Kalmaegi from different	

contributions88

Fig. 8-6 Co-seismic gravity change, given as a jump (step function) in the SG gravity records at HS, due to the earthquake on September 6.90

Fig. 8-7 Magnitude 9.0 – near the east coast of Honshu, Japan earthquake on March 11, 2011.....92



Chapter 1 Introduction

1.1 Background

Taiwan, like many other regions in the western Pacific, is prone to attack from such hazards as landslide, typhoon and earthquake, which may create mass changes and in turn gravity changes. Such gravity changes are usually over a small area, and cannot be sensed by the gravity sensor of a satellite gravity mission such as GRACE, but might be detected by a highly-sensitive, ground-based gravimeter such as SG. In April 2006, two single-sphere observatory SGs (OSGs), serial numbers T48 and T49, were installed at tunnel B of Mt. 18-Peak in Hsinchu City, Taiwan. At the same time, two absolute gravimeters (AGs), serial numbers 224 and 231, were introduced in Taiwan. All the gravimeters belong to Ministry of the Interior (MOI) and setup in tunnels of the national gravity datum service (NGDS).

T48 and T49 were manufactured by GWR and have a nominal sensitivity of one ngal and a stability of $6 \mu\text{gal year}^{-1}$ or better ($1 \text{ ngal} = 10^{-11} \text{ m s}^{-2}$). The HS SG station is now included in the SG network of GGP (Fig. 1-1). The GGP's objective in the global geodetic observing system (GGOS) is to provide high quality SG data for geodynamic research. Most of the AG measurements collected with the two AGs (FG5 #224 and FG5 #231) are carried out by the laboratory of geodesy and geodynamics (LOGG, <http://www.logg.org.tw/>, Fig. 1-2). The latitude, longitude and elevation of LOGG are 24.79258°N , 120.98554°E and 87.6 m , respectively. LOGG is about 8.6 km from the Taiwan Strait, where the average depth is 80 m . Here the ocean tide amplitude and phase change rapidly (Jan et al., 2004).

HS is the closest station to the Tropic of Cancer in GGP and will be most sensitive to gravity change due to the motion of the earth's inner-core in the summer solstice, making HS the best for testing the universality of free fall (Shiomi, 2006). Real-time

data of typhoons, earthquakes and continuous GPS observations around Taiwan, accessible at the central weather bureau (CWB, <http://www.cwb.gov.tw/>) of Taiwan, are used in connection to SG. The introduction of these gravimeters motivates this study, which will focus on the regional characteristics of Taiwan. Specifically, this study will emphasize gravity datum establishment, geodynamics and atmospheric events.

GPS is an important tool to aid the interpretation of gravity data and it will be also covered in this study. The study will monitor and analyze the mechanisms of gravity changes and GPS changes from 2006 to 2011. The events of typhoons and earthquakes affect gravity changes and may contribute most to gravity and geometric changes in some cases. They will be also investigated using SG, AG and GPS in this dissertation.

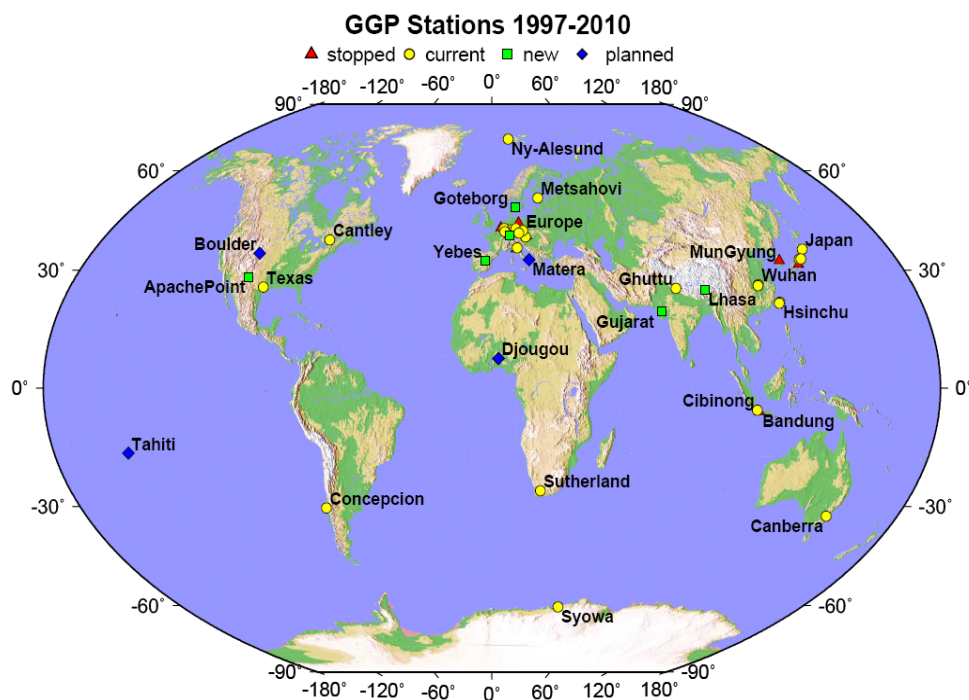


Fig. 1-1 Current and planned SG stations in the world, squares represent the new stations, circles the current stations, diamonds the planned stations (Described in the ggpnews20, 2010)

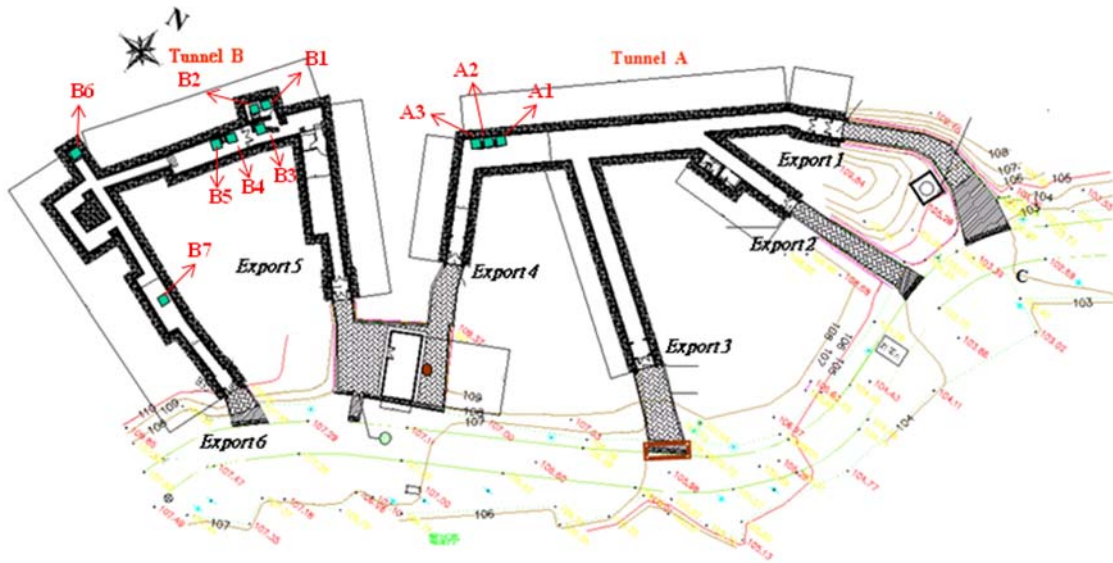


Fig. 1-2 Layout of NGDS, T48 is installed at B2

1.2 Literature Review

There are many phenomena that cause environmental changes in Taiwan. This study uses gravimeters to monitor selected phenomena. Because of this, we need a gravity datum as the basis for analyzing the mechanisms of such phenomena. SG is highly sensitive to gravity changes due to solid earth tide, ocean tide loading, atmosphere, groundwater, soil moisture, tilt variation and other environmental changes (e.g. Warburton and Goodkind, 1977; Crossley et al., 1995; Dal Moro and Zadro, 1998; Neumeyer et al., 2004; Boy and Hinderer, 2006). It is necessary to explain the physical significance of SG and to identify the standard operating procedure (SOP) for SG data processing. After removing data noises, including spikes, gaps and steps of SG, we use the parallel observations of AG and SG values for data comparison and calibration (Van Ruymbecke, 1989; Richter et al., 1995; Falk et al., 2001). Currently, the most commonly used technique for calibration of SG record is based on parallel observations of SG and AG (Sato et al., 1996; Francis et al., 1998; Imanish et al., 2002). If AG is not available, the CF of SG is usually determined by comparison between the

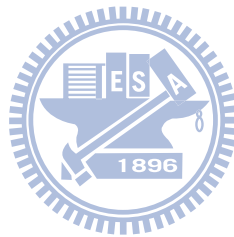
theoretical solid earth tide and SG raw measurements (voltage). The nominal drifting rate of SG is $6 \mu\text{gal year}^{-1}$ claimed by GWR instrument (Warburton and Brinton 1995), but the drifting rate could vary from one SG to another.

With SG, it is possible identify gravity changes of non-tectonic origins, such as those due to typhoons and earthquakes (Imanishi et al., 2002). The gravity-atmosphere admittances for various atmospheric conditions in typhoons will vary and is a potential application of SG (Kim et al., 2011). The impact of typhoon-generated gravity changes could be large during the developing stage than during the mature and decaying stages of the typhoon (Kim et al., 2011). About 90% of the atmospheric effects were attributed to local atmospheric variations within 50 km of the station (Mukai et al., 1995). Selected co-seismic gravity perturbations have been detected and analyzed using SG to demonstrate the sensitivity of SG, and the SG results have been compared with those obtained by seismometers (Imanishi et al., 2004; Hwang et al., 2009; Kim et al., 2009; Nawa et al., 2009). In addition, AG and continuous GPS measurements have been used to study mass transfer and vertical movement due to mountain building (Segall and Davis, 1997; Jacob et al., 2008).

1.3 Outline of dissertation

This dissertation is organized into 9 chapters. Chapter 2 is to present the principles of SG and AG, including an in-depth introduction of instruments, specifications and software. Chapter 3 describes data processing of SG, including filtering, CF, modeling the solid earth tide and ocean tide loading. Chapter 4 describes the effect of ocean tide loading, tidal analysis, and comparison with theoretical solid earth tide. Chapter 5 shows the environment effects on gravity observations. Chapter 6 presents the geological settings around the NGDS, it is the key work for establishing an AG reference and data preparation for the GGP. Chapter 7 shows the result from gravity

observations of the project “AGTO” in southern Taiwan, jointly conducted by France and Taiwan. The motivation of AGTO is to see mass changes due to middle-to-long term tectonic motion from repeated gravimetric and continual GPS measurements. The gravity and vertical trends of 25 AG stations and 313 permanent GPS stations will be presented. Chapter 8 presents an extensive discussion on global atmospheric and local atmospheric effects on gravity. The gravity effects from Typhoon Kalmaegi and Morakot are described in detail in this chapter. Finally, a summary, conclusions and suggestions are presented in the final chapter.



Chapter 2 Principles of superconducting gravimeters and absolute gravimeters at LOGG

2.1 Superconducting gravimeter

2.1.1 Introduction

The following discussion is largely based on the existing literature and internet information of SG (i.e., <http://www.gwrinstruments.com>). Since every SG or AG gravimeter is unique when it is manufactured, the purpose of this chapter is to present information that is mostly exclusive to the SG and AG gravimeters at LOGG. In the dewar of T48 (Fig. 2-1), there is a spherical proof mass levitated by the forces from a magnetic field generated by a pair of superconducting coils. Continued currents generate the magnetic field that is superconducting below a temperature of 9.3 K in two niobium coils (GWR, 2011). There are magnet coils without resistive loss and decay in time between the two niobium coils. Compared to a relative gravimeter using metal spring, the sensor of magnet force gradient of SG can detect a very weak signal. Small changes in gravity produce large displacements of the proof mass. The displacement transducers set around the proof mass to detect the weak gradient in the stable magnetic field. T48 and T49 at LOGG have the features described above, and can contribute to applications as follows:

- (1) Resolving density of mass change related to elevation change measured by GPS.
- (2) Continuous gravity monitoring of geophysical phenomena such as solid earth tide, ocean tide loading, atmospheric loading, hydrology, and Earth rotation.
- (3) Validation of satellite gravity observations from CHAMP, GRACE and GOCE.
- (4) Real-time monitoring of volcanoes.
- (5) Monitoring long-term crustal motion and sea level anomaly.
- (6) Calibrating AG measurements.

(7) Establishing a high-accuracy gravity reference station (together with AG).

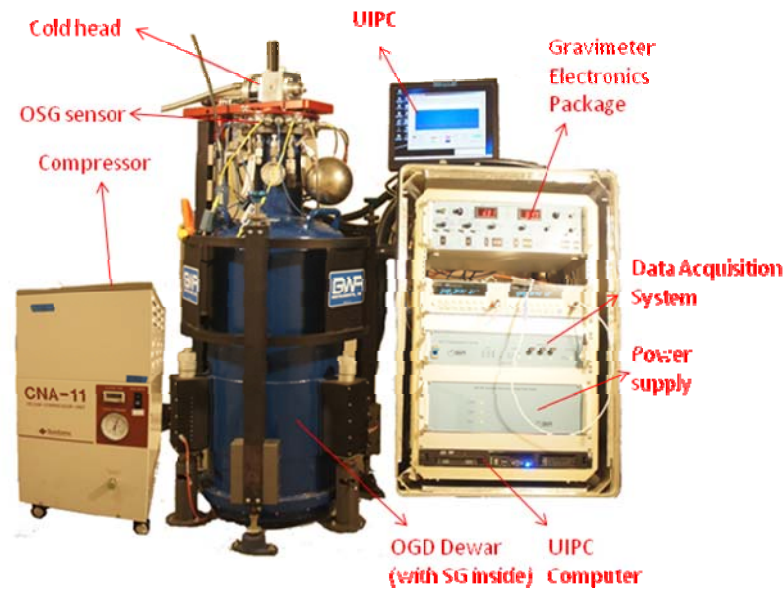


Fig. 2-1 T48 at LOGG, showing the coldhead, integrated electronics with digital data acquisition system (DDAS) and user interface PC (UIPC) software.

2.1.2 Observatory SG (OSG) sensor

An OSG is equipped with all the necessary units designed to store the electronic signals, and maintain the SG automatically at low temperature (Fig. 2-1). The analog controller is integrated with the DDAS and generates gravity output in digital format. The gravimeter sensing unit (GSU, Fig. 2-2) is built around a 2.5 cm diameter spherical proof mass which is made in a stable magnetic field and different from a conventional gravimeter. Since the sphere is superconducting with perfect diamagnetism, the surface currents on the sphere are not affected by any magnetic fields from GSU's interior. The interaction is between the applied magnetic field and the surface currents of sphere which produce the levitation force.

A superconducting magnetic shield is built around GSU to exclude the effects from the external magnetic field. The thermal shield sensor is put around the vacuum chamber where and temperature is stable in a few K. This sensor makes the gravity unit

insensitive to environmental effects such as changes in external humidity, temperature and atmospheric pressure. The OSG sensor specifications of T48 and T49 are as follows (GWR, 2011):

- (1) Precision: 0.1 to $0.3 \mu\text{gal Hz}^{-1/2}$
- (2) Drift: Typically less than $6 \mu\text{gal year}^{-1}$ after the initial 6 to 12 months of stabilization period
- (3) Calibrate: The manufacture, GWR, does not provide with calibration data of the GSU sensor. Users generally either perform a coarse calibration by parallel observing with AG and SG or fitting the observed gravity signal to the theoretical model of solid earth tide.
- (4) Stable Calibration Factor: Comparing the OSG signal with models of solid earth tide, the scale factor is considered to be constant with variations smaller than 0.01% over several years.

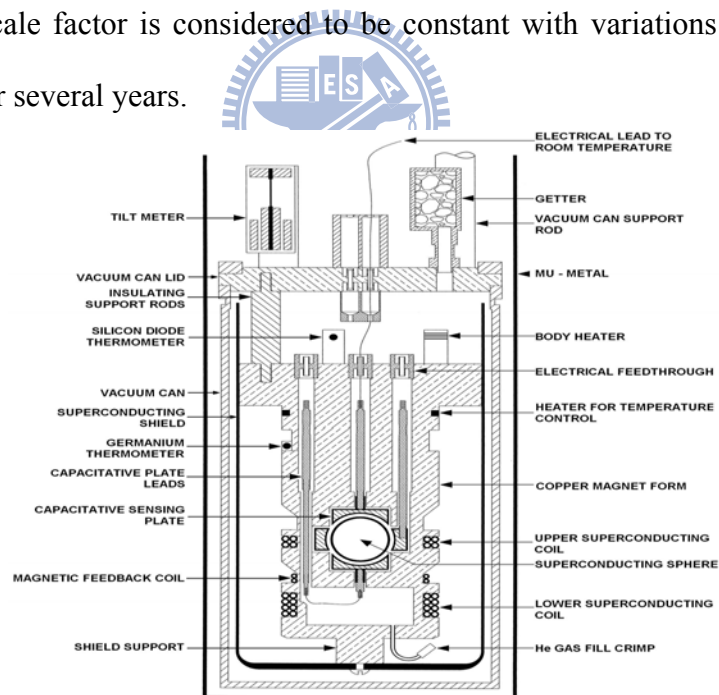


Fig. 2-2 A cross section scheme of the T48 sensor (GWR, 2011)

2.1.3 Refrigeration System

The super-insulated dewar of a SG is operated in the 4 K cryogenic refrigeration system. This design removes the need to refill the dewar with liquid helium after the system is cooled down. When unrefrigerated, the loss rate of liquid helium is less than 5% per day and has chance to refill the dewar in 20 days. This capacity offers sufficient helium reserves so that the instrument can continue to operate under power failures or refrigeration maintenance.

The helium refrigeration system is an independent system separated from the liquid helium dewar. The relative pressure of helium gas in the dewar is controlled in a range from 0 to 0.5 PSI, but the refrigeration system needs to operate at 350 PSI. These two helium gas circuits do not contact with each other. The refrigeration system consists of a helium compressor, coldhead (Fig. 2-3), vibratile diaphragm and flexible interconnected hoses. The application of the 4 K refrigeration system allows a much longer continuous interval of data collection. Noise related to the liquid helium is small and there are only occasional disturbances due to scheduled service of the coldhead. In summary, the refrigeration system specifications of T48 and T49 are as follows (GWR, 2011):

- (1) Capacity: 35 liters
- (2) Dimensions: 42 cm diameter x 114 cm high
- (3) Total height installed on support feet: dewar is 116cm, dewar with coldhead is 130cm
- (4) Minimum height required to transfer liquid helium (with standard equipment): 180 cm
- (5) Hold time between refills (un-refrigerated): 20 days minimum
- (6) Weight of dewar with GSU installed: 60 kg
- (7) Concrete pier required: 80 cm x 80 cm



Fig. 2-3 Refrigeration system of Sumitomo CNA-11 helium compressor, and Sumitomo RDK-101E coldhead of T48

2.1.4 Integrated electronics

The integrated electronics and data acquisition package (IEDP, Fig. 2-4) are used to control and monitor the SG, as well as provide SG-log data. The sub units of IEDP are listed as follows (GWR, 2011):

- (1) Gravimeter electronics package(GEP-3)
 1. Gravimeter control electronics
 2. Tilt control electronics
 3. Temperature control electronics
 4. Auxiliary electronics
 5. GEP-3 remote control card, A/D converter and Setup circuitry
- (2) Data acquisition system (DDAS-3)
 1. Data acquisition controller (DAC)
 2. UIPC software
 3. High resolution 7½ digit resample of “Agilent 34420A nano-volt meter”
 4. Trimble GPS receiver

5. Optical isolators and lightening arrestors for digital data
 6. DDIG-3 - OSG dual digitizer package
- (3) DPS-4 - Current supply for initializing levitation magnets
 - (4) VOTS-3 - Voltage transfer standard package
 - (5) TREE-3 - Temperature regulated electronics enclosure
 - (6) PRE-5 - Paroscientific met-3 meteorological measurement system

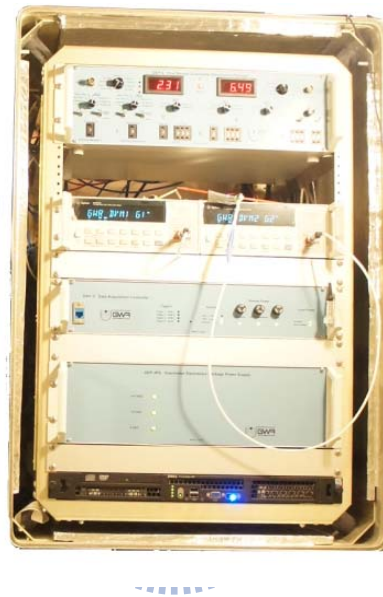


Fig. 2-4 integrated electronics and data acquisition system of T48

2.1.5 User interface PC software

The user interface PC (UIPC) is part of the DDAS-3 data acquisition system, and contains a custom software program. The operator has the full right to control the SG functions, including the specification of atmospheric instrument, operation procedures, data logging and archiving. The UIPC software for all data channels is displayed in graphical and archiving in the monthly data. The operator needs to enter notes when the system has changed. A general alarm system is automatic described to trigger when any channels exceed normal limits and email notification to the operator in a number of ways. We can write the automated FTP routine in the operation system to

automatically upload data to different archival sites on a daily basis. The graphical user interface (GUI) of configurations is in Fig. 2-5.

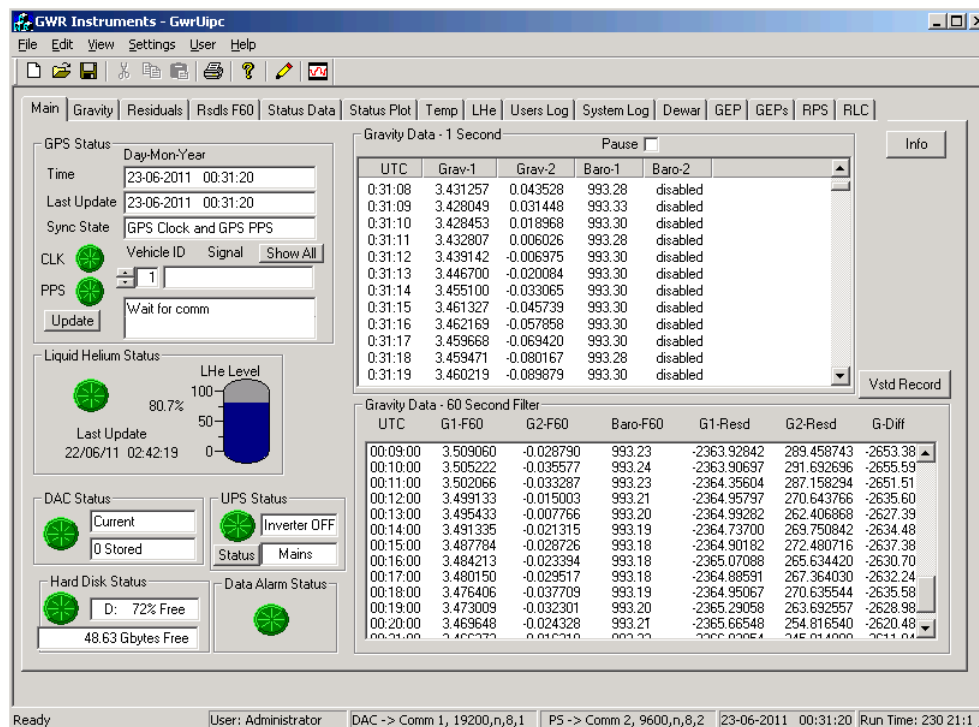


Fig. 2-5 The UIPC main page, showing 1-s (top panel) and 60-s real-time (grav1), filtered gravity (grav2) and barometer data (baro-1), GPS status, liquid helium status, DAC status and alarm status.

2.2 Absolute gravimeter

2.2.1 Introduction

An AG determines the vertical acceleration based on the measurements of travelling distance and time of a free falling corner cube. It provides the direct measurement of absolute gravity. As shown in Fig. 2-6, the optical fringes go through zero and the precise time are recorded by an atomic clock. A least-square (LSQ) fit to the time and distance pairs is used to determine the gravity.

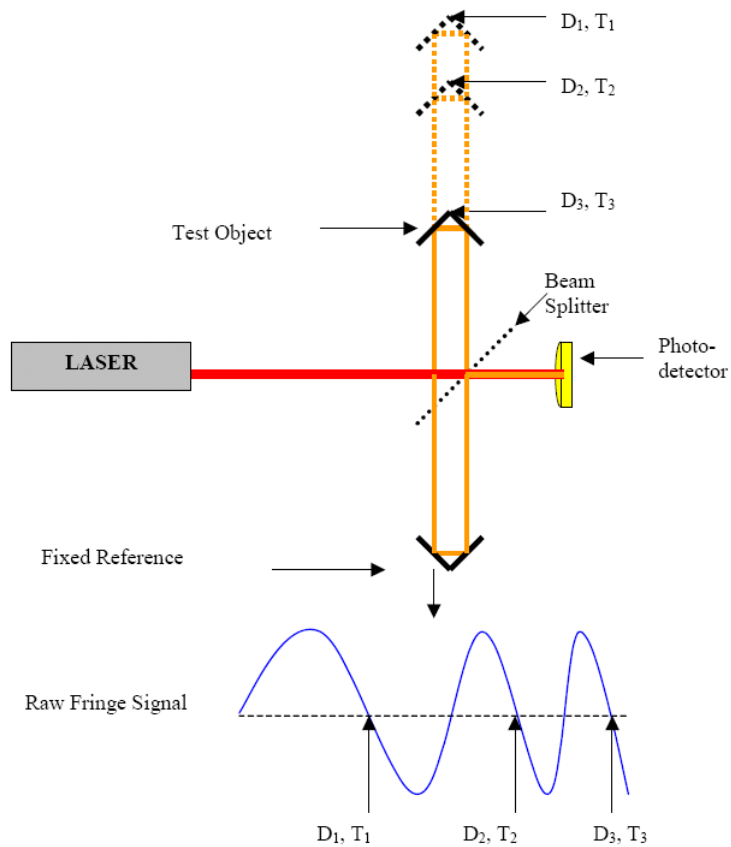


Fig. 2-6 Principle of AG measurement by laser to detect distance and rubidium to detect time (FG5 Manual, 2006)

The following example shows how an absolute gravity value is measured by an absolute gravimeter. The traveling distance of a free-fall test mass in the dropping chamber is expressed as (FG5, 2006)

$$x_i = x_0 + v_0 t_i + \frac{1}{2} g t_i^2 \quad (2-1)$$

where x_0 is the origin height, t_i is the travel time, v_0 is the initial velocity, and g is the gravity. With three distance measurements, $x_1 = D_1 - D_0$, $x_2 = D_2 - D_0$, $x_3 = D_3 - D_0$, where D_0 is the top position of vacuum chamber, we have

$$\begin{aligned}
x_1 &= v_0 t_1 + \frac{1}{2} g t_1^2 \\
x_2 &= v_0 t_2 + \frac{1}{2} g t_2^2 \\
x_3 &= v_0 t_3 + \frac{1}{2} g t_3^2
\end{aligned}
\tag{2-2}$$

By setting $S_1 = x_2 - x_1$, $S_2 = x_3 - x_1$, $t_1 = T_2 - T_1$, $t_2 = T_3 - T_1$, and removing v_0 , we have

$$g = \frac{2\left(\frac{S_2}{t_2} - \frac{S_1}{t_1}\right)}{t_2 - t_1}
\tag{2-3}$$

where g is the absolute gravity value. The accuracy of the distance measurements by laser interferometer is about 10^{-8} ms^{-2} and the accuracy of the time measurement by a rubidium clock is 10^{-13} s . These accuracies combine to yield an accuracy of μgal for a gravity measurement.

2.2.2 Specifications of FG5

At LOGG, there are two FG5 gravimeters with serial numbers are 224 and 231.

Each of the gravimeters consists of (Fig. 2-7):

- (1) Dropping (or Vacuum) Chamber
- (2) Interferometer Base
- (3) Superspring
- (4) Laser
- (5) System Controller
- (6) Electronics.

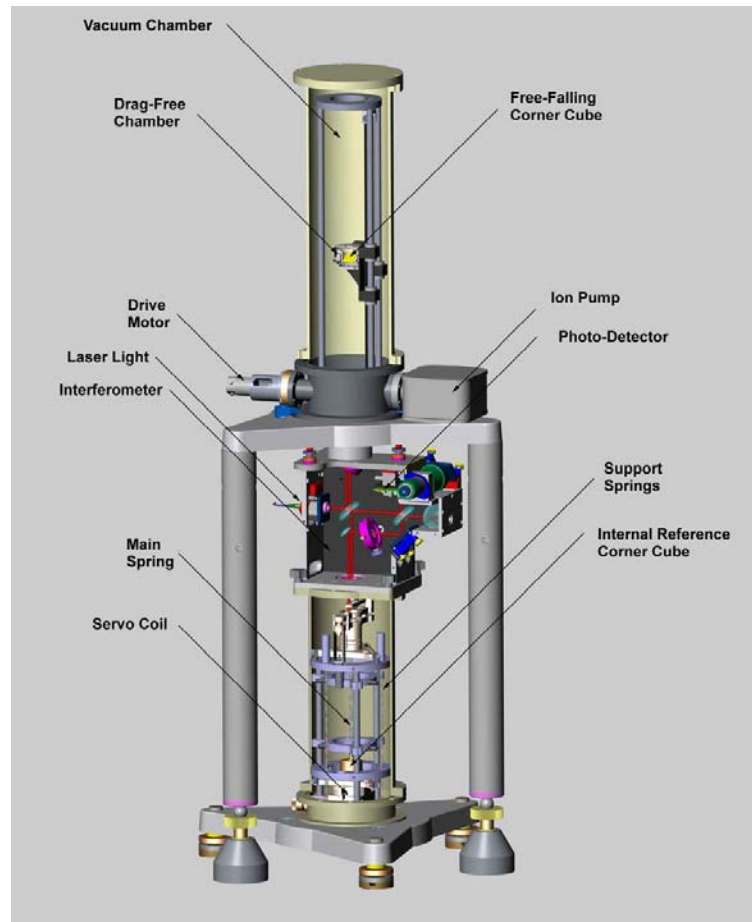


Fig. 2-7 The schematic of a FG5 system. (FG5Manual, 2006)

The system specifications of FG5 are as follows:

- (1) Power: 100-240 V AV
 - (2) Weight
 - 1. Interferometer Base & Laser: 20 kg
 - 2. Dropper: 25 kg
 - 3. Superspring: 20 kg
 - 4. Turbo Pump: 15 kg
 - 5. Dropper Tripod: 20 kg
 - 6. Superspring Tripod: 12 kg
 - 7. Electronic Rack: 15 kg
- Total: 127 kg

(3) Transit case dimensions

1. Interferometer base (IB) & Laser: 64 x 56 x 38 (cm)
2. Dropper: 64 x 38 x 80 (cm)
3. Superspring: 31 x 30 x 57 (cm)
4. Turbo pump: 37 x 37 x 47 (cm)
5. Dropper tripod: 77 x 56 x 28 (cm)
6. Superspring tripod: 64 x 56 x 38 (cm)
7. Electronic rack: 64 x 56 x 38 (cm)
8. Computer: 38 x 32 x 7 (cm)

(4) Operating temperature: 15-30 °C

The corner cube is allowed to free-fall inside the vacuum dropping chamber. Interferometer base is used to monitor the position of the corner cube which is falling in the dropping chamber. The superspring is an active long-period isolation device used to provide an inertial reference for the gravity measurement. The computer allows the user to operate user interface, control the system, change the processing of data, and stores the results. The system provides high accuracy timing for the measurement which is necessary when doing the high precision absolute gravimetry.

2.2.3 Gravity gradient for gravity reduction

Gravity gradient is needed to reduce the height effect on gravity observations. For example, a raw FG5 observation may refer to a reference point along the dropping chamber and it may be reduced to a gravity value at the pillar marker or at a desired height for later applications. The relationship between vertical position z and gravity g is:

$$\frac{d^2 z}{dt^2} = g + g_\gamma z \quad (2-4)$$

where t is traveling time of the test mass, g and g_γ are gravity and gravity gradient.

The traveling distance is a function of time, velocity and gravity:

$$z(t) = \frac{1}{2} g(t^2 + \frac{g_\gamma t^4}{12}) + v(t + \frac{g_\gamma t^3}{6}) + x(1 + \frac{g_\gamma t^2}{2}) \quad (2-5)$$

where x and v are the initial position and velocity. In this study, a GRAVITON-EG gravimeter is used to measure gravity gradients.

A GRAVITON-EG is a fully automated and portable gravimeter for determination of relative gravity. For gravity gradient determination, a GRAVITON-EG is set up at different heights (Fig. 2-8), where the gravity values are measured. The ratio between the differences in gravity and height is the gravity gradient. The measured gravity gradients at pillar A1, A2, A3 and B1 of LOGG (Fig. 1-2) are listed in Table 2-1 and are used for gradient reductions for AG measurements at LOGG. Six campaigns of gravity gradient measurements are illustrated in Fig. 2-9. We find that gravity gradient measurements at A3 are more stable than those at A1, A2 and B1. Because a gradient is computed as the ratio:

$$g_r = \frac{g_2 - g_1}{h_2 - h_1} \quad (2-6)$$

where g_2 , g_1 are the measured gravity values at different height h_2 , h_1 . We can determine the standard error of gravity gradient as :

$$\sigma_{g_r} = \frac{\sqrt{\sigma_{g_1}^2 + \sigma_{g_2}^2}}{h_2 - h_1} \quad (2-7)$$

where σ_{g_r} is the standard error of each site. The gravity gradients at A1, A2, A3 and B1 range from -2.69 to -2.57 $\mu\text{gal cm}^{-1}$. Such variations are due to different accuracies of the GRAVITON-EG that are largely results of environmental noises. For example, a large rainfall, a strong wind and a busy traffic will lead to large gravity perturbations that result in a degraded gravity measuring accuracy. The mean values in Table 2-1 are used for gravity reduction.

Table 2-1: Gravity gradients and standard errors at different times

pillar \ time	A1 ($\mu\text{gal cm}^{-1}$)	A2 ($\mu\text{gal cm}^{-1}$)	A3 ($\mu\text{gal cm}^{-1}$)	B1 ($\mu\text{gal cm}^{-1}$)
1	-2.60 ± 0.19	-2.60 ± 0.19	-2.38 ± 0.17	-2.52 ± 0.18
2	-2.50 ± 0.18	-2.54 ± 0.18	-2.36 ± 0.17	-2.69 ± 0.19
3	-2.59 ± 0.19	-2.63 ± 0.19	-2.39 ± 0.17	-2.60 ± 0.19
4	-2.52 ± 0.18	-2.70 ± 0.19	-2.72 ± 0.20	-2.68 ± 0.19
5	-2.51 ± 0.18	-2.62 ± 0.19	-2.80 ± 0.20	-2.73 ± 0.20
6	-2.69 ± 0.19	-2.63 ± 0.19	-2.82 ± 0.20	-2.89 ± 0.21
mean	-2.57 ± 0.08	-2.62 ± 0.08	-2.58 ± 0.07	-2.69 ± 0.08

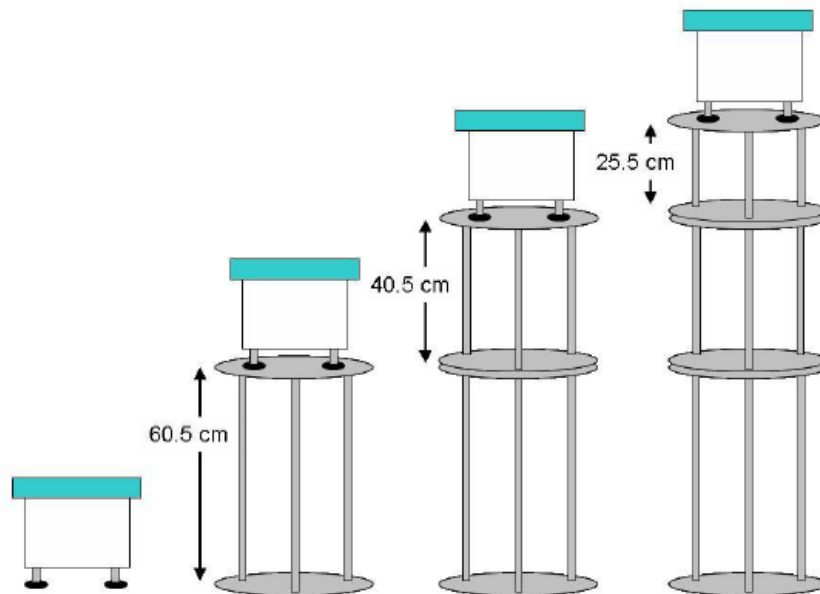


Fig. 2-8 Measuring gravity values at different heights for gradient determination

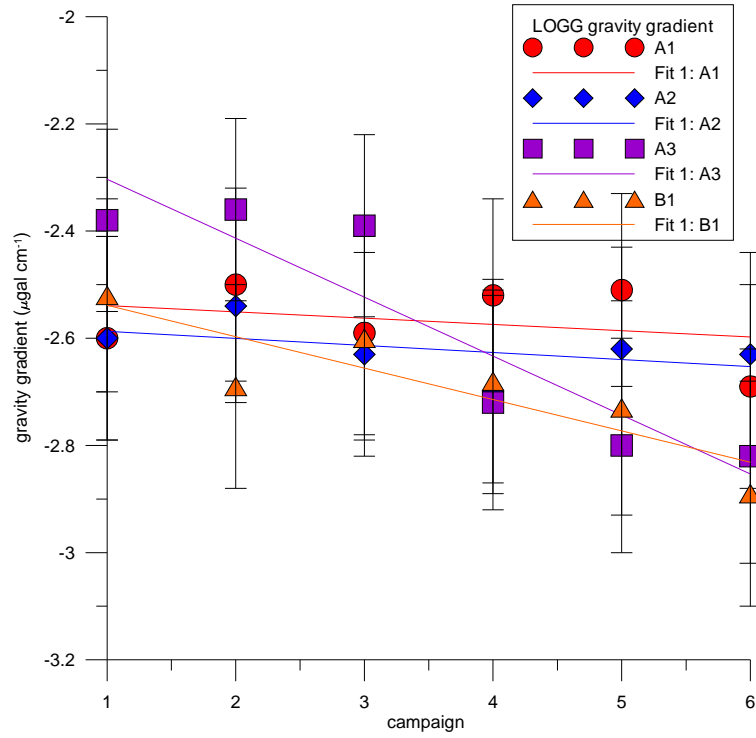
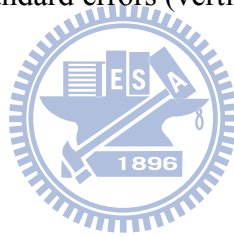


Fig. 2-9 Gravity gradients and standard errors (vertical bars), and the trends of gradient



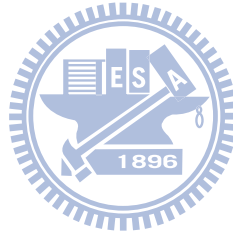
2.2.4 Quality assessment of AG measurement

The estimated precision of an AG gravity value is based on the repeated measurements from the total drops, plus the standard errors (uncertainties). First, the standard error of a single gravity measurement is estimated from repeated measurement at the same location as :

$$\sigma = \sqrt{\frac{\sum_{i=1}^n (g_i - \bar{g})^2}{n-1}} \quad (2-8)$$

where σ is the standard error, n is the number of measurements, g_i is the measurement, and \bar{g} is the average of the measurements. The standard error of the mean value is

$$\sigma_{\bar{g}} = \frac{\sigma}{\sqrt{n}} \quad (2-9)$$



In addition to measurement errors, the uncertainties in models include the environmental gravity effects. A corrected mean gravity is:

$$\bar{g}' = \bar{g} - \sum_{i=1}^k C_i \quad (2-10)$$

where C_i are the environmental gravity effects. If the gravity effects are uncorrelated, the total standard error (or total uncertainty) is

$$\sigma_{g'} = \sqrt{\sigma_g^2 + \sum_{i=1}^k \sigma_{C_i}^2} \quad (2-11)$$

where $\sigma_{C_i}^2$ are the error variance of the model corrections. The g software can estimate the total uncertainties based on repeat measurements and the built-in correction models.

FG5 #231 has been set up at LOGG to measure gravity values on B1 and T48 is set up on B2. More than 70 AG observation records have been collected on B1 from 2006 to 2011. The gravity gradient of B1 is $-2.69 \mu\text{gal cm}^{-1}$ (see Table 2-1) and it is used for the reduction of raw FG5 records to ground values. The mean gravity from 2006 to 2011 is $978,901,463 \mu\text{gal}$. Fig. 2-10 shows the gravity values with standard errors. The total standard errors (uncertainties) range from 0.14 to $0.53 \mu\text{gal}$, and such variations in the total standard errors are mostly due to background noises/vibrations that affect the laser frequency.

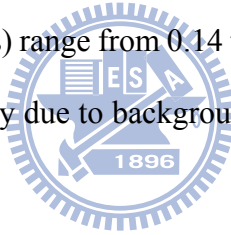


Table2-2: Absolute gravity measurements and result on B1 from FG5 #231 in 2010

Time	Drop number	Gravity (μgal)	Standard error of mean (μgal)	Total uncertainty (μgal)
January 27, 2010	2977	978,901,199	0.25	2.06
January 31, 2010	21976	978,901,199	0.16	2.03
March 6, 2010	2591	978,901,192	0.53	2.08
March 15, 2010	3786	978,901,194	0.48	2.08
July 23, 2010	28310	978,901,187	0.14	2.03
September 16, 2010	2989	978,901,202	0.18	2.02

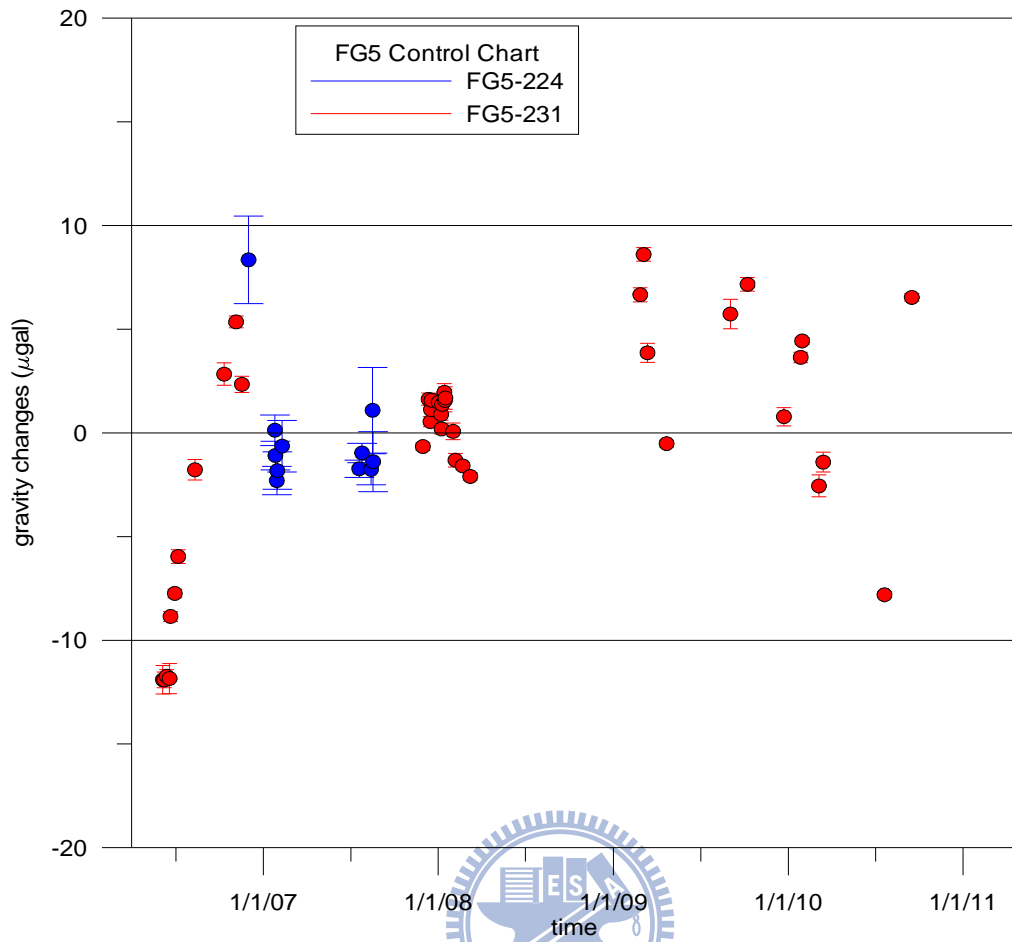


Fig. 2-10 Gravity values (relative to the mean of all measurements) and standard errors (vertical bars) at pillar B1 observed by the FG5 #224 and #231 gravimeters

Chapter 3 Processing SG data

3.1 Filtering and decimation of raw SG data

The gravity records (measured in voltage) at the 1-s (one-second) interval from T48 have been recorded from April 1, 2006 to present. The data contains noises and signals of various origins such as earthquakes or other disturbances caused by human interferences. The raw data should be screened and repaired before use. In this study, the spikes and other disturbances were removed using TSoft software, which is the standard software provided by the International Center for Earth Tides (ICET, <http://www.astro.oma.be/ICET/>) for SG data processing. Fig. 3-1 illustrates the time series before and after fixing a discontinuity in the data record. The discontinuity is like a cycle slip in GPS phase data. The discontinuity removal is based on the comparison between the predicted and observed values after the discontinuity. This discontinuity fixing is very important to an un-interrupted, long-term record of SG observations that are used to validate/calibrate satellite gravity observations from missions like GRACE. In particular, it is only possible to obtain reliable inter-annual change of gravity from SG with SG records without step functions (discontinuities) in the records.

In case of data loss due to instrument or helium problems, the data gaps are filled by theoretical values from the Dehant-Defraigne-Wahr (DDW) solid earth model. The data are then LSQ fitted to generate records at the 1-m (one-minute) and 1-h (one-hour) intervals using a filtering procedure, which, together with the raw 1-m data, are uploaded to GGP. The 1-m and 1-h data are used for subsequent processes and analyses.

TSoft can accept different sample rates, which are specified in two steps. The first step is to define the new sample rate and change the interpolation type. There are three types of interpolator in Tsoft: linear, cubic and cumulative interpolators. The second

step is to choose the LSQ-filter types. The LSQ-filter removes outliers and performs filtering. It can also decimate 1-s data (the smallest sampling interval of SG) to a larger interval (e.g., one-minute or one-hour). Before data decimation, filtering must be applied to the raw data to remove aliasing at a coarse (than 1-s) interval. The LSQ-filter in TSoft includes a low-pass and high-pass filter. A filter consists of two parameters: the cut-off frequency or central frequency f_0 , and the band width f_w (see also Fig. 3-2). The cutoff frequency is the frequency beyond which the signal components are truncated to zero. In fact, filtering and re-sampling of the raw gravity records are made simultaneously. If the raw data contain discontinuity, gap and spike, Tsoft will first remove them and then performs filtering and re-sampling.

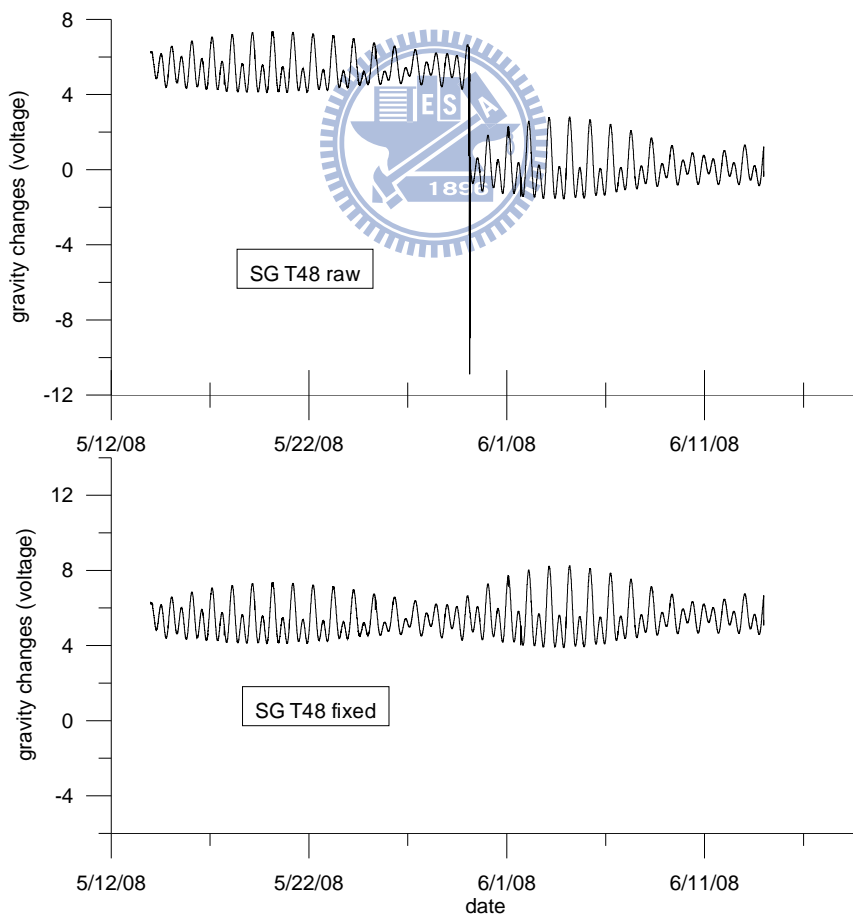


Fig. 3-1 The raw data before (top) and after (bottom) removing discontinuities and disturbances.

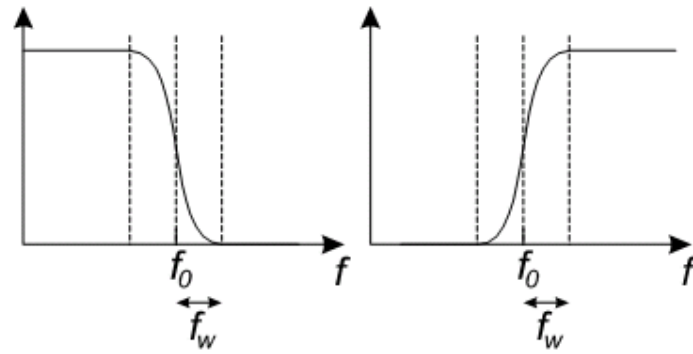


Fig. 3-2 Filter response functions of the low-pass (left) and high-pass (right) used in the LSQ filters of TSoft

3.2 Calibration factor

3.2.1 Estimation of calibration factor using the DDW model gravity

The CF of a SG is a number that converts a voltage measurement from SG to a gravity measurement. A method to estimate CF is by comparing gravity values from a solid earth tide model and voltage records of a SG. In this study, first we use TSoft to generate theoretical gravity values using the DDW solid earth tide model (Dehant et al., 1999) at a given location. By specifying the latitude of a given location, DDW may yield the theoretical amplitude factors and phases for various tidal components, which are used to compute theoretical gravity values. The modeled gravity values are then compared with the SG records (in voltage) to determine the CF of the SG gravimeter that generates the voltage records.

The amplitude factors and phases at selected frequency ranges based on the DDW solid earth tide at HS are listed in Table 3-1. Fig. 3-3 shows the theoretical gravity values from July 1, 2009 to September 30, 2009, which shows dominating variations at the semi-diurnal and diurnal bands. Fig. 3-4 shows the gravity values from the voltage records multiplied by the CF estimated. This method of CF estimation is a standard method employed at SG stations without parallel AG and SG measurements.

Table 3-1: Amplitude factors and phases at HS based on DDW at HS

Minimum Frequency (CPD)	Maximum Frequency (CPD)	Amplitude factor	Phase Shift	Group Name
0.000000	0.002427	1.00000	0.0000	long
0.002428	0.249951	1.15811	0.0000	Mf
0.721500	0.906315	1.15415	0.0000	Q1
0.921941	0.940487	1.15415	0.0000	O1
0.958085	0.998028	1.14926	0.0000	P1
0.999853	1.003651	1.13551	0.0000	K1
1.005329	1.005623	1.26557	0.0000	PSI1
1.007595	1.011099	1.16964	0.0000	PHI1
1.013689	1.216397	1.15613	0.0000	OO1
1.719381	2.182843	1.16174	0.0000	All2
2.753244	3.381478	1.07341	0.0000	M3
3.381379	4.347615	1.03900	0.0000	M4

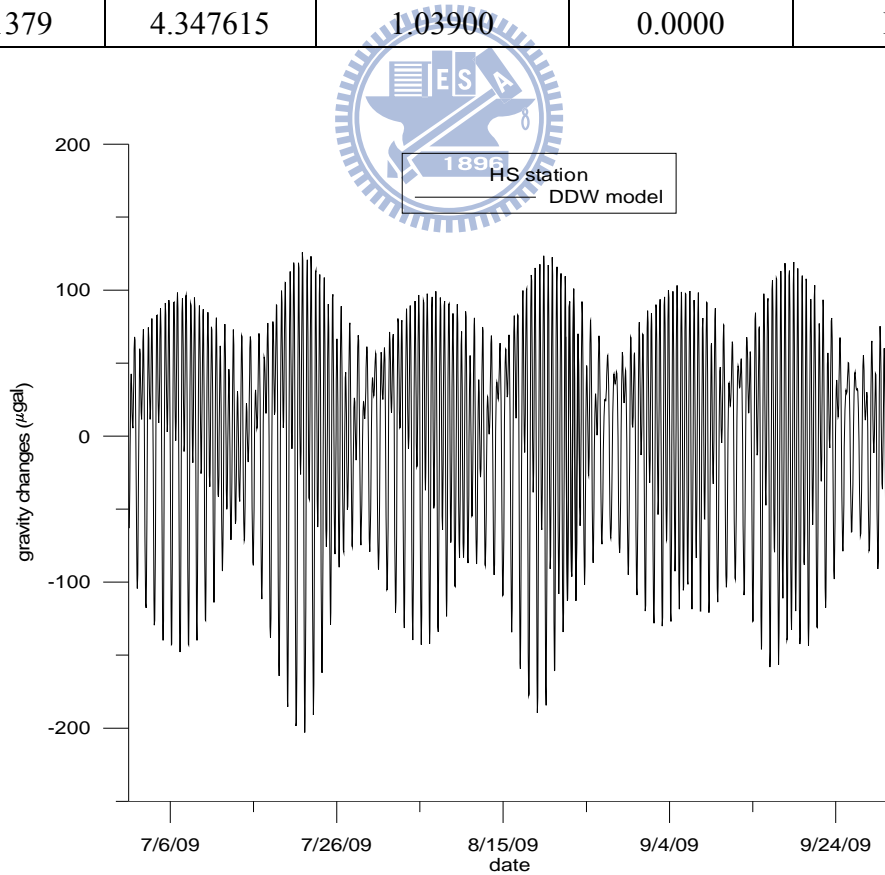


Fig. 3-3 Gravity values based on DDW (Dehant et al., 1999) solid earth model from

July 1, 2009 to September 30, 2009

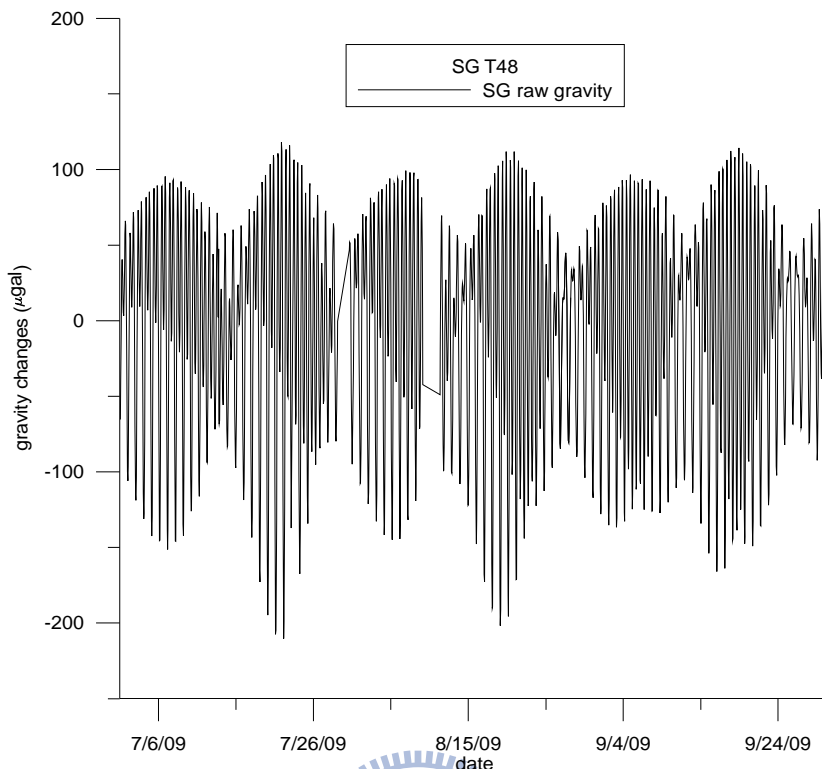


Fig. 3-4 Gravity values converted from voltage records (T48) using the CF estimated with the DDW from July 1, 2009 to September 30, 2009 by Tsoft

3.2.2 Calibration factor from parallel SG and AG gravity observations

If an AG is available at a SG station, the CF of the SG is estimated using parallel observations of SG and AG. In this study, we also use AG to estimate the CF of T48 and T49 at HS. A preliminary result for T48 was reported in Hwang et al. (2009). This method has been demonstrated in various studies (e.g., Francis et al., 1998; Imanishi et al., 2002; and Tamura et al., 2005). In fact, the CF and the drifting rate of a SG are two crucial parameters that must be taken into account when using the SG data at HS.

The CF estimation in the following description will provide useful information to users of the HS SG data. Because T48 contributes data to GGP, we present a detailed result of estimating the CF of T48 and T49 below. T48 records used for CF estimation contain major jumps of up to 1000 μgal due to helium re-filling problems. Therefore,

careful treatments of the raw data must be made before computing CF. We determine an optimal CF of T48 using parallel observations of T48 and a FG5 #231 given in Table 3-2. The pillars for T48 and FG5 are separated by about 1 meter. In total, 17 sessions of parallel observations were collected in summary of first phase. The following model is adopted for the determination of the CF:

$$g(t) = f_c V(t) + b - s(t) \quad (3-1)$$

where f_c is the CF, b is an offset, s is the drifting rate of T48, g and V are records from FG5 and T48 (or T49), respectively. Given the observations (g and V), the standard LSQ technique is used to compute f_c and b . FG5 and SG sense the same gravity effects of solid earth tide and ocean tide, as well as any other time-varying gravity effects, to produce gravity variations, which are exactly what we need for determining the CF. Before the LSQ solution, the outliers in the SG and FG5 data, which occur mostly during heavy rainfall, earthquakes and abrupt changes of air pressure due to typhoons, were removed. As an example, Fig. 3-5 shows the four cases of T48 and FG5 data for estimating the CF from the session of June 5, 2006 to February 2, 2008. The variation in the FG5 gravity records are mainly caused by solid earth tide and are almost linearly correlated with the SG records in voltage (correlation coefficient 0.953). The FG5 was not continuous measurement in case 1 due to an earthquake. The raw data whose difference with the filtered data exceed 3 times of standard error were removed. The FG5 #231 did not record continuous measurement in case 2, and again due to an earthquake. However, in case 3, the FG5 collected continuous measurement despite a big earthquake. In case 4, the FG5 records were continuous without earthquake interruptions. The residuals of FG5 observations from

the LSQ adjustment (raw FG5 gravity values minus fitted gravity values) roughly follow the normal distribution, suggesting that the linear model in Eq. (3-1) is adequate, and the estimated parameters in Table 3-2 are unbiased.

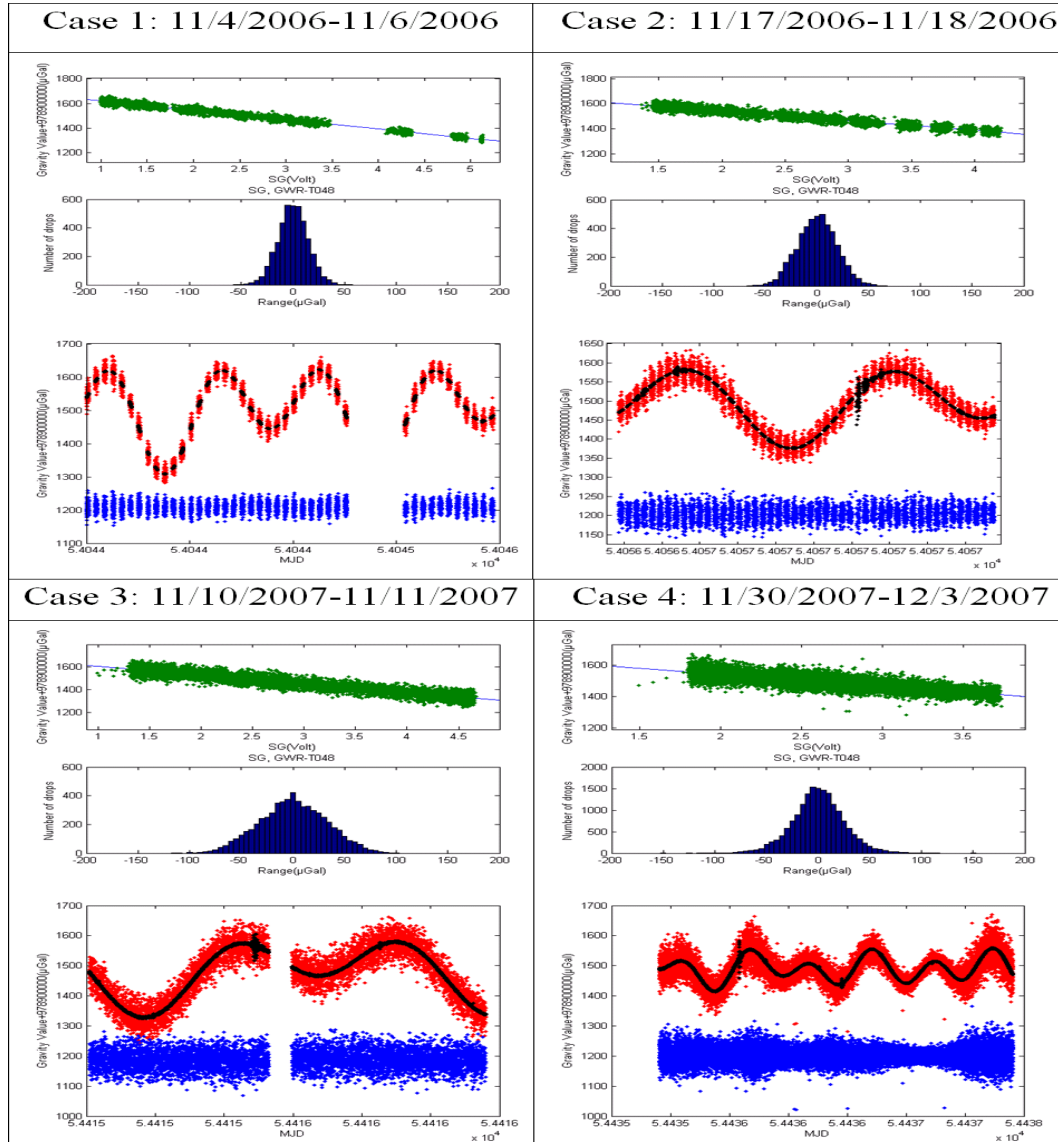


Fig. 3-5 Four cases of estimating CF of T48 by FG5 #231

In Table 3-2, there are three phases of T48 records and a new phase begins at the time of a major helium problem fixing. Phase 1 is from April 1, 2006 to March 15, 2008. Phase 2 is from March 16 to May 30, 2008. Phase 3 is from June 1, 2008 to present. The result in Table 3-2 shows different CF values are found in different measurement phases. This suggests that a major helium fixing will change the condition inside the dewar. In

theory, the position of the spherical proof mass will be moved after the major helium fixing, leading to a varying CF. Using all data in Table 3-2, we obtain a CF of $-76.087 \mu\text{gal voltage}^{-1}$ for T48.

Table 3-2: Sessions of parallel superconducting (T48) and absolute (FG5) gravity observations for determining the calibration factor of T48

FG5 #231 (GMT)	drops	CF ($\mu\text{gal voltage}^{-1}$)	offset ¹ Eq. (3-1)
June 9-10, 2006	1614	-75.984 ± 0.373	1701.521 ± 1.220
June 13-14, 2006	1436	-76.350 ± 0.360	1701.220 ± 1.023
June 21-23, 2006	4318	-76.032 ± 0.150	1701.265 ± 0.439
June 30- July 2, 2006	4216	-76.621 ± 0.242	1702.087 ± 0.710
July 7-11, 2006	4004	-76.807 ± 0.232	1701.646 ± 0.675
October 11-12, 2006	1259	-77.383 ± 0.433	1701.485 ± 1.276
November 4-6, 2006	3344	-76.030 ± 0.155	1698.591 ± 0.461
November 17-18, 2006	2746	-75.622 ± 0.349	1693.337 ± 0.980
March 2-3, 2007	3087	-76.506 ± 0.184	1685.009 ± 0.546
March 4-7, 2007	3023	-76.499 ± 0.417	1686.692 ± 1.190
November 10-11, 2007	1722	-75.876 ± 0.472	1679.035 ± 1.409
November 30- December 3, 2007	7038	-75.838 ± 0.366	1696.695 ± 1.106
December 16-18, 2007	7758	-75.504 ± 0.264	1695.724 ± 0.731
January 2, 2008	2058	-75.465 ± 0.566	1695.689 ± 1.543
January 7-9, 2008	9938	-76.169 ± 0.092	1697.120 ± 0.270
February 6-7, 2008	2978	-75.407 ± 0.353	1696.310 ± 1.060
February 21-23, 2008	8901	-76.227 ± 0.122	1697.254 ± 0.263
<i>Summary of first phase</i>	<u>42183</u>	<u>-76.087 ± 0.067</u>	<u>1695.809 ± 0.201</u>
April 5-7, 2008	10375	-76.502 ± 0.088	1440.698 ± 0.274
<i>Summary of second phase</i>	<u>10375</u>	<u>-76.502 ± 0.088</u>	<u>1440.698 ± 0.274</u>
July 31- August 1, 2008	2449	-76.175 ± 0.212	1440.698 ± 0.274
January 15-20, 2009	12904	-75.617 ± 0.212	1432.257 ± 0.115
April 22-26, 2009	11580	-75.782 ± 0.115	1444.486 ± 0.129
<i>Summary of third phase</i>	<u>27483</u>	<u>-75.547 ± 0.094</u>	<u>1438.228 ± 0.086</u>

¹ A mean of 978900000 μgal is removed.

3.3 Detided gravity

The gravity effect from the solid earth tide is a dominating signal in SG measurements. To assess gravity effects due to hydrological changes and other geodynamic phenomena, such a gravity effect should be removed from the raw SG gravity records. A gravity record without the solid earth tide effect is called detided gravity or residual gravity in this section. Both the raw and residual gravity records will contain the same step functions and other anomalous values, but the latter has a larger gravity magnitude. The step functions are removed manually in Tsfot from the raw data. After removing step functions from the raw data and calculating the residual, one should see whether the residual contains periodic signals. If periodic signals are present in the residual, it is likely that the fitted solid earth tide model is not sufficiently good. The anomalous gravity values such as the ones shown in Fig. 3-6, which are due to helium fixing, cannot be used to generate tidal parameters. Such a detided gravity (residual) can also be used to compute ocean tide loading gravity effects and other periodic gravity signals.

Depending on the purpose, there are different cases of detided gravity, which are defined and summarized in Fig. 3-7.

(1) Case 1: T48 solid earth tide

(1-1) The DDW gravity is removed from the corrected gravity to yield tide-free gravity.

(1-2) The difference between corrected gravity and tide-free is computed to obtain refined gravity.

(1-3) The refined gravity is used to compute amplitude factors and phases.

(2) Case 2: T48 ocean tide loading

(2-1) The effects of atmospheric effect, ground water effect, soil moisture effect, and polar motion effect are removed from the corrected gravity (section

5.2).

(2-2) The result of gravity is used to compute ocean tide loading

(3) Case 3: T48 observed tide

(3-1) The raw SG gravity is filtered, decimated, calibrated to yield corrected gravity.

(3-2) The corrected gravity is used to estimate all periodic signal components, which are included all environment effects.

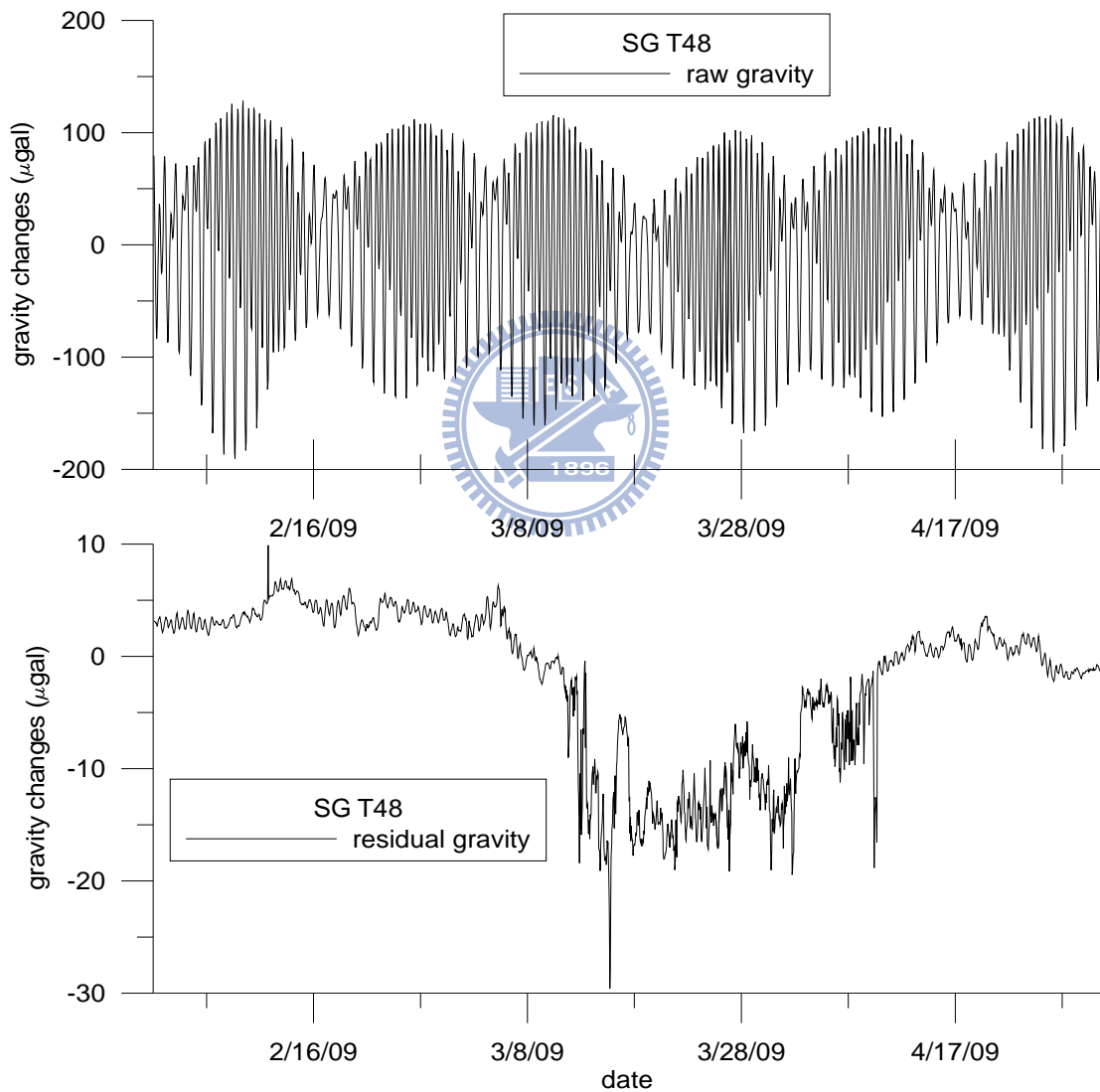


Fig. 3-6 Signal (top) and residual (bottom) from T48 during liquid helium loss. The residual gravity shows a clear drop associated with the helium loss.

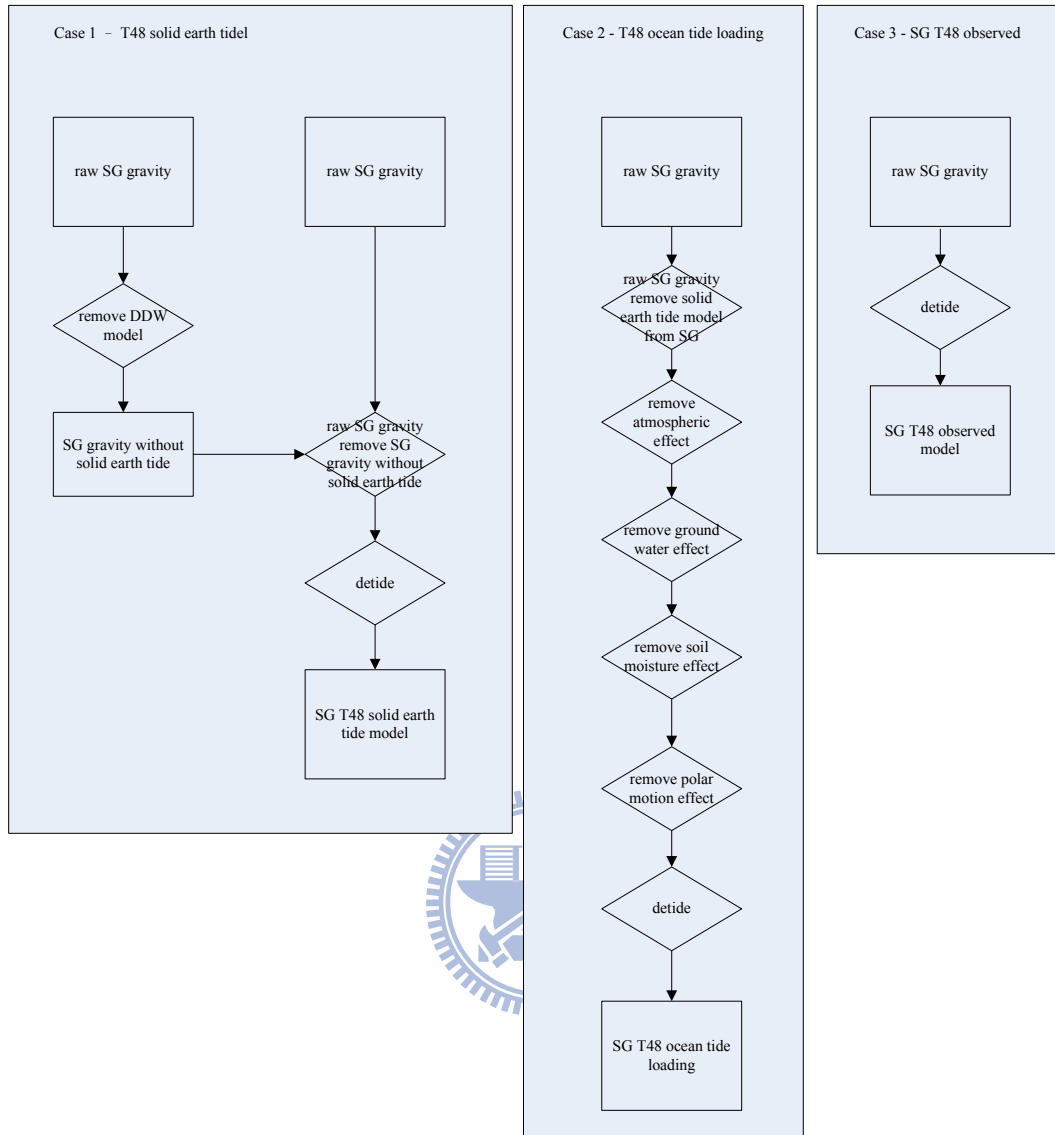


Fig. 3-7 Procedure of solid earth tide from (left), procedure of ocean tide loading (middle), procedure of observed (right) from T48

3.4 Sub-seismic noise levels of residual gravity from T48

Since the beginning of GGP in 1997, the number of SG stations has increased to 30 in 2011. SG has been used principally in tidal studies due to its high sensitivity and low drifting rate. But when searching for elusive signals, like the gravity variations associated with the translational mode of the inner core, stacking data of different sites is needed. Data from GGP allow the comparison of noise levels of different stations.

The noise level with the New Low Noise Model (NLNM, Peterson, 1993) is used as a reference model to give an estimation of the quality of a SG (Rosat and Hinderer, 2011). NLNM is a model that shows the lowest noise level of a seismometer. Here we compare the spectra of residual gravity from several continuously recording SG stations like HS, Bad Homburg (BH), Membach (MB), Canberra (CB), Medicina (MC), Sutherland (SU) and Strasbourg (ST) (Fig. 3-8).

We use a standard procedure to obtain the power spectral densities (PSDs) of residual gravity over a quiet time period in order to evaluate the combined instrument and site noise in the frequency band of 0.01 to 10 *mHz* at the selected SG stations. Fig. 3-8 shows the spectrum of the residual gravity from T48 measurements in June 2008, along with the spectrum implied by NLNM. At frequencies less than 0.03 *mHz*, the spectra of T48 exceed that of NLNM, suggesting that the SG records at HS yield noises that are larger than theoretical noise level of a seismometer. The PSD of HS is on average larger than those at other stations. This is mainly because the HS station is 8.6 km to the oceans, which creates high-frequency oscillations in the T48 observations.

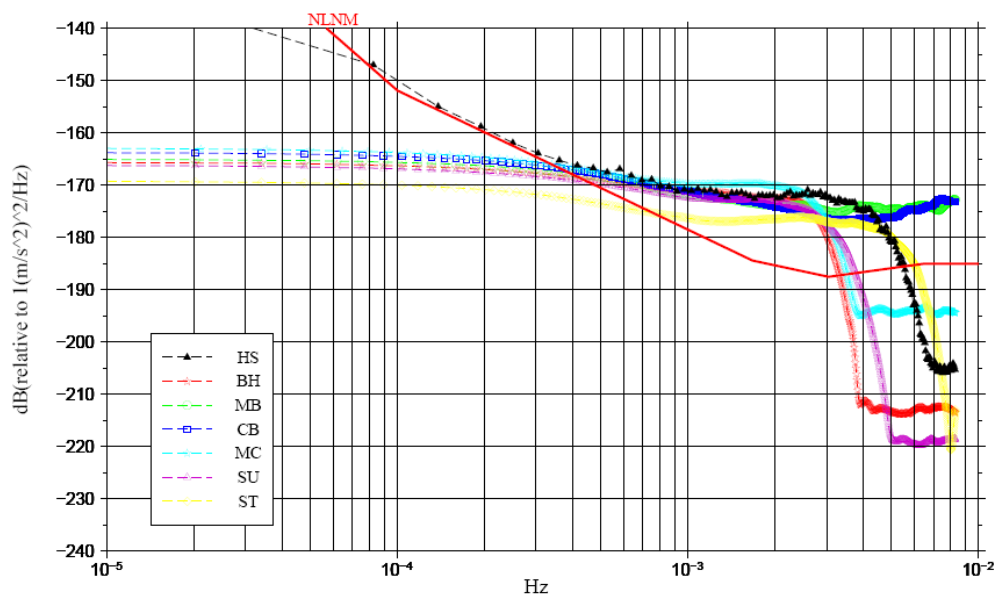


Fig. 3-8 Sub-seismic noise levels of residual gravity at HS station, compared with other SG stations (the names are defined on the GGP web page)

Chapter 4: Analyses of tidal parameters and ocean tide loading gravity effects

4.1 Spectral analysis of SG gravity records

We use Tsoft to decimate the T48 records to the 1-h records for tidal analysis. Fig. 4-1 shows the spectrum of the raw SG gravity records. As expected, we observe the six leading tidal components of M_2 , K_1 , S_2 , O_1 , N_2 and P_1 . Note that the distinct signal component labeled M_3 in Fig. 4-1 at a frequency of about $2.9 \text{ cycle day}^{-1}$, which is due to the M_3 ocean tide modulated by the complex bathymetry and coastal lines around the Taiwan Strait. This shows that, as pointed out by Hinderer and Crossley (2004), and Boy et al. (2004), SG provides interesting and important data to study non-linear tides over such a shallow-water area as the Taiwan Strait.

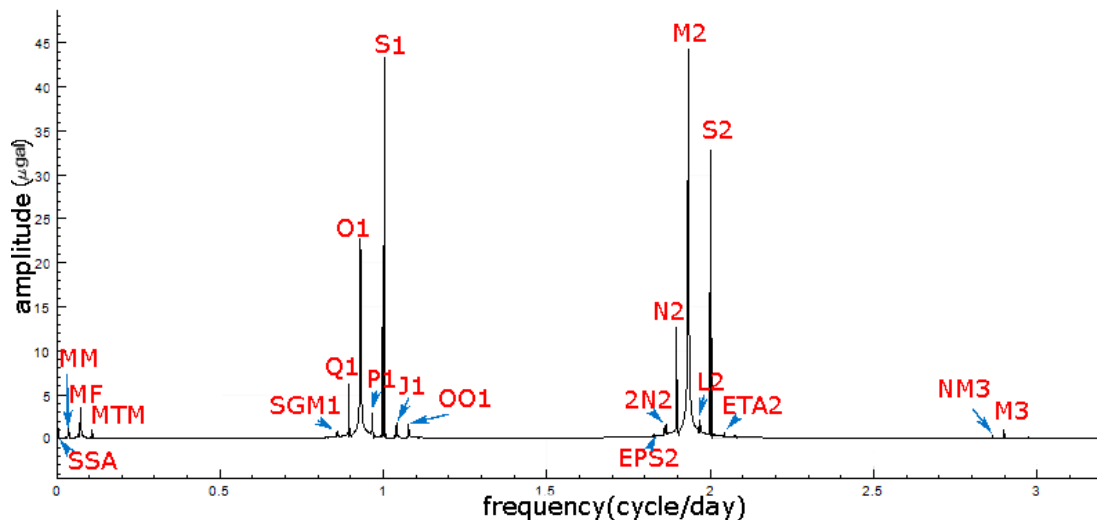


Fig. 4-1 Tidal spectra of raw gravity records in five years were recorded by T48. Two clusters are present at the semi-diurnal and diurnal wave bands. Tides with periods shorter than the period of M_3 are not shown here.

4.2 Tidal analysis

Hourly data of SG are generally used to estimate the gravimetric solid earth tide. These measurements contain information about other instrumental parameters (e.g. temperature, atmospheric pressure), external mass changes and measurement errors. For tidal analysis, the observation equation of an hourly SG measurement is expressed as:

$$R(t) + v(t) = \sum_{i=1}^n d_i F_i(t) + \sum_{j=1}^m \delta_j A_j(\text{model}) \cos(w_j t + \Phi_j(\text{model}) + \Delta\Phi_j) + D(t) \quad (4-1)$$

where $R(t)$ is the SG recorded value, $v(t)$ is the residual, d_i is the regression coefficient, δ_j and $\Delta\Phi_j$ are amplitude ratios and phase shifts Φ_j of the tidal wave j , w is the circular frequency, A_j is amplitude, F_i and $D(t)$ are the state parameters and the drift (Torge, 1989).

Chojnicki (1973) uses a low-pass filter to remove long-periodic tides and other long-wave effects from gravity observations. In this study, we used two years of T48 (2006-2008) and T49 (2008-2010) data to compute tidal parameters and extract ocean tide loading gravity effects. We compared two computer programs, ETERNA (Wenzel, 1996) and BAYTAP-G (Tamura et al., 1991), for tidal analysis. Tables 4-1, 4-2 (by ETERNA) and Table 4-3 (by BAYTAP-G) summarize the amplitude factors, phases

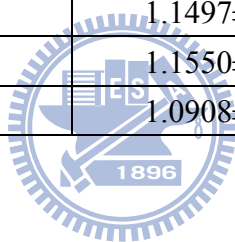
and their standard (formal) errors for selected short-period tides. A phase in Table 4-1, 4-2 or 4-3 is the phase difference between the equilibrium solid earth tide and the actual tide due to the lunar-solar tidal potential. The standard errors in Tables 4-1, 4-2 and 4-3 show that the estimated amplitudes and phases are statistically significant. The tidal parameters obtained from the two computer programs are quite consistent. As expected, the standard errors increase with the tidal periods. The M_2 wave, the most dominant component in the gravity time series, has the least standard error in both amplitude factor and phase. The phase of ψ_1 constituent shows a large formal error exceeding 1° , which may be reduced when a longer SG record than 2 years is available for the analysis.



Fig. 4-2 compares the observed model from SG T48 and T49 with raw gravity signal of SG T48 and T49. Based on Table 4-1 and Table 4-2, the standard errors of the tidal parameters from SG T49 are larger than those from SG T48. The raw gravity of T49 contains more rapid oscillations than T48. The amplitudes of M_2 from T49 and T48 are 71.681 ± 0.024 and 71.452 ± 0.014 μgal , respectively. Fig. 4-3 shows the differences in the amplitudes from T48 and T49, where the M_2 wave shows the largest difference of 0.23 μgal . Fig 4-4 shows the difference in the phases. The phases of T49-derived waves are in general smaller than the T48-derived phases, especially in the diurnal band. The reason for the differences is not clear.

Table 4-1: T48 tidal analysis results by ETERNA (2006-2008)

Wave	Amplitude (μgal)	Amplitude factor	Phase lag ($^{\circ}$)
Q ₁	5.649±0.008	1.2485±0.0018	-1.34±0.08
O ₁	29.061±0.008	1.2298±0.0003	-2.28±0.02
M ₁	2.251±0.007	1.2119±0.0036	-2.50±0.17
P ₁	13.125±0.010	1.1939±0.0009	-2.74±0.04
S ₁	0.317±0.014	1.2178±0.0541	2.54±2.55
K ₁	39.145±0.009	1.1784±0.0003	-2.84±0.01
ψ_1	0.331±0.009	1.2712±0.0355	-5.38±1.60
\emptyset_1	0.584±0.010	1.2348±0.0209	-0.96± 0.97
J ₁	2.191±0.008	1.1791±0.0045	-3.36±0.22
OO ₁	1.173±0.005	1.1544±0.0049	-2.51±0.24
2N ₂	2.314±0.011	1.2232±0.0058	1.86±0.27
N ₂	13.947±0.014	1.1773±0.0012	-3.40±0.06
M ₂	71.452±0.014	1.1548±0.0002	-3.03±0.01
L ₂	1.817±0.018	1.0388±0.0104	-0.81±0.58
S ₂	33.093±0.014	1.1497±0.0005	-1.63±0.02
K ₂	9.033±0.011	1.1550±0.0014	-1.59±0.07
M ₃	1.203±0.003	1.0908±0.0024	-0.31±0.12

**Table 4-2: T49 tidal analysis results by ETERNA (2008-2010)**

Wave	Amplitude (μgal)	Amplitude factor	Phase lag ($^{\circ}$)
Q ₁	5.625±0.023	1.2433±0.0052	-1.86±0.24
O ₁	29.131±0.025	1.2328±0.0010	-2.36±0.05
M ₁	2.377±0.027	1.2800±0.0144	-2.73±0.65
P ₁	13.116±0.028	1.1932±0.0025	-2.59±0.12
S ₁	0.534±0.041	2.054±0.1560	45.57±4.34
K ₁	39.254±0.026	1.1817±0.0008	-2.94±0.04
ψ_1	0.332±0.027	1.2786±0.1029	-19.39±4.61
\emptyset_1	0.600±0.029	1.2676±0.0615	-0.87± 2.78
J ₁	2.236±0.024	1.2032±0.0129	-3.30±0.61
OO ₁	1.195±0.019	1.1762±0.0184	-4.70±0.90
2N ₂	2.307±0.016	1.2195±0.0085	0.92±0.40
N ₂	14.064±0.022	1.1871±0.0018	-3.48±0.09
M ₂	71.681±0.024	1.1585±0.0004	-3.13±0.02
L ₂	1.826±0.024	1.0438±0.0140	-2.50±0.77

Wave	Amplitude (μgal)	Amplitude factor	Phase lag ($^\circ$)
S ₂	33.092±0.023	1.1496±0.0008	-2.39±0.04
K ₂	8.997±0.019	1.1504±0.0025	-1.77±0.12
M ₃	1.205±0.019	1.0922±0.0171	-0.58±0.89

Table 4-3: T48 tidal analysis results by BAYTAP-G (2006-2008)

Wave	Tidal amplitude (μgal)	Amplitude factor	Phase lag ($^\circ$)
Q ₁	5.646±0.017	1.2482±0.0037	-1.45± 0.17
O ₁	29.056±0.016	1.2299±0.0007	-2.28± 0.03
M ₁	2.239±0.011	1.2053±0.0060	-2.51± 0.29
P ₁	13.117±0.016	1.1933±0.0015	-2.65± 0.07
S ₁	0.309±0.004	1.1874±0.0142	-2.12± 0.69
K ₁	39.149±0.014	1.1783±0.0004	-2.83± 0.02
ψ_1	0.309±0.004	1.1888±0.0157	-2.96± 0.76
\emptyset_1	0.563±0.007	1.1896±0.0153	-2.85± 0.74
J ₁	2.193±0.012	1.1801±0.0066	-3.34± 0.32
OO ₁	1.176±0.007	1.1573±0.0068	-2.86± 0.34
2N ₂	1.919±0.003	1.2247±0.0020	1.81± 0.09
N ₂	13.947±0.005	1.1778±0.0004	-3.36± 0.02
M ₂	71.435±0.005	1.1550±0.0001	-3.03± 0.00
L ₂	1.831±0.006	1.0473±0.0033	-0.75± 0.18
S ₂	33.057±0.004	1.1488±0.0001	-1.89± 0.01
K ₂	9.031±0.003	1.1546±0.0004	-1.63± 0.02
M ₃	1.206±0.002	1.0942±0.0018	-0.16± 0.10

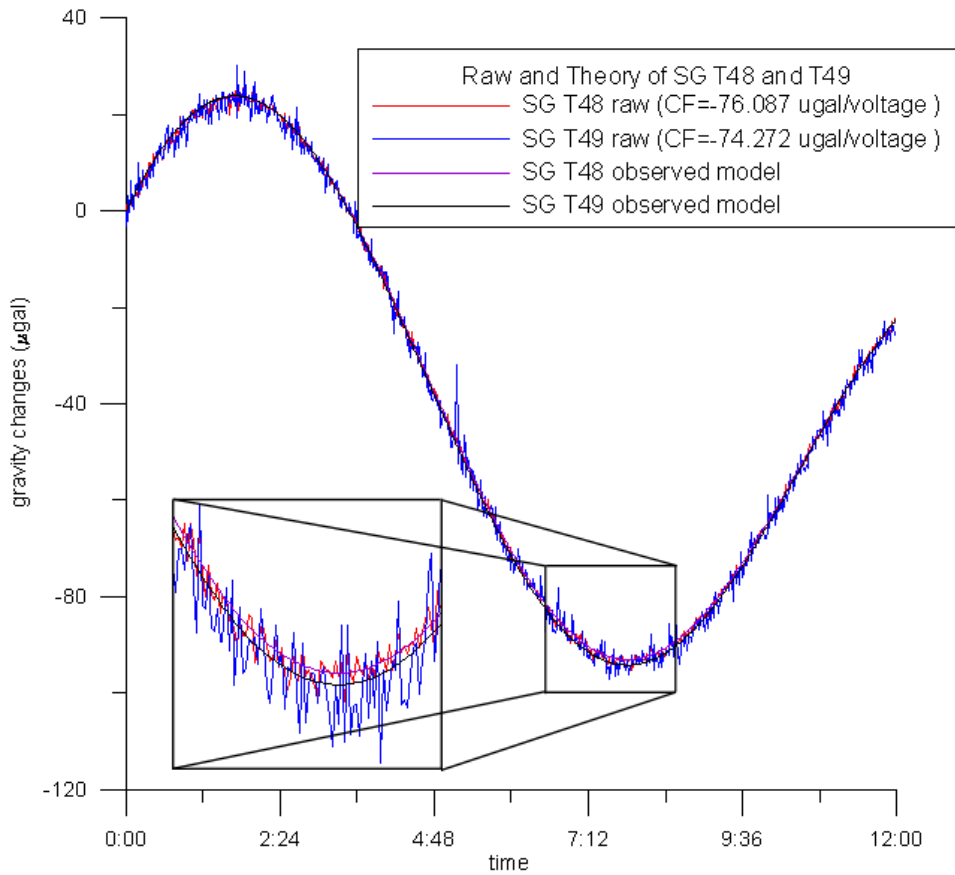


Fig. 4-2 Comparison the raw gravity records and observed models of T48 and T49 in January 1, 2009.

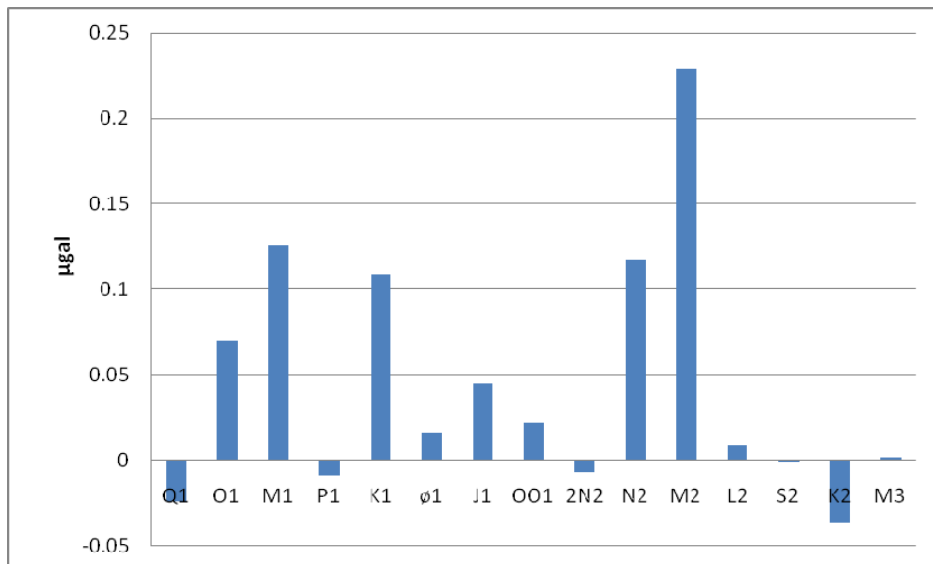


Fig. 4-3 Difference amplitudes from T48 and T49 (T49 minus T48).

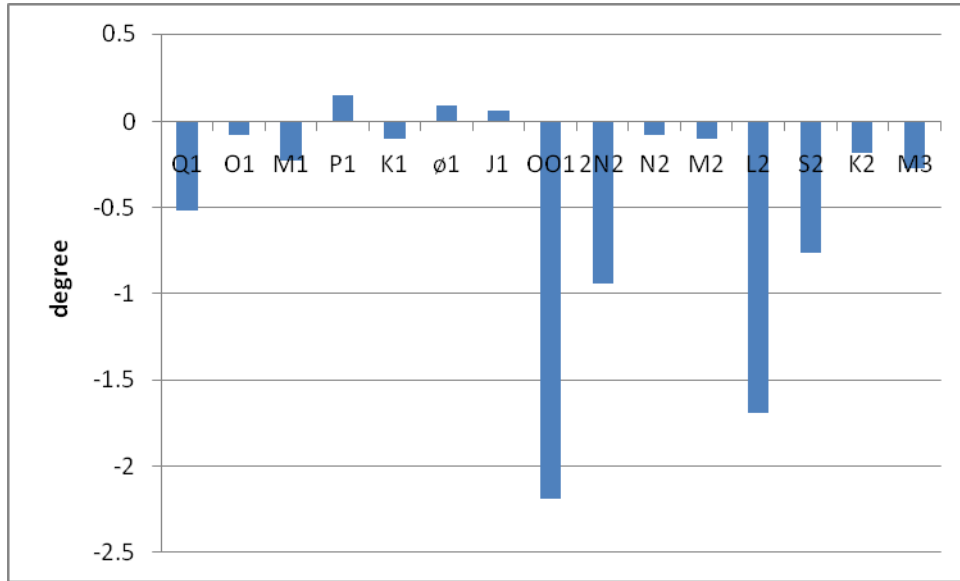


Fig. 4-4 Difference phases from T48 and T49 (T49 minus T48).

4.3 Ocean tide loading gravity effects

In addition to the solid earth tide, the ocean tide loading gravity effects are also clearly identified in SG records, where the ocean tidal amplitude of M_2 is about 1.7 m in HS. The ocean tide loading gravity effects are expressed in the convolution between ocean tide and the Green's function:

$$\Delta g = \frac{G\rho_w}{R^2} \iint \frac{h(\phi, \lambda)(p-u)}{(1+p^2-2pu)^{3/2}} ds - \rho_w \iint h(\phi, \lambda)K(\psi)ds \quad (4-2)$$

where G is the Newtonian gravitational constant, ρ_w is the density of sea water, R is the mean earth radius, h is tidal height (depending on latitude ϕ and longitude λ), ψ

is spherical distance, $u = \cos \psi$, $p = (R + H) / R$, $ds = R^2 \cos \phi d\phi d\lambda$, and K is Greens' function based on the loading love numbers of Farrell (1972). The first and second terms of the right-hand side of Eq. (4-2) represent the effects of attraction and loading, respectively. The detail of our ocean tide loading model and software development used in the study is given by Huang et al. (2009). Note that the Newtonian (attraction) effect depends on station height H through variable p .

In the Taiwan Strait, the amplitude of the M_2 ocean tide increases toward the central part of the Strait and it reaches a maximum (about 2.2 m) at a latitude about 24°N , and then decreases almost linearly northwards to the East China Sea and southwards to the South China Sea. Also, there is a standing M_2 ocean tide near the central Taiwan Strait (Jan et al., 2004). As an example, the M_2 amplitudes at Keelung (25.2°N , near the East China Sea), Hsinchu (24.8°N , near HS) and Pintung (22.0°N , near the South China Sea) are 0.6, 1.6 and 0.2 m, respectively.

SG observations can also be used to estimate ocean tide loading gravity effects, as carried out by Boy et al. (2004). This is achieved by removing an adopted solid earth tide model from the SG data, and all the other known, well modeled signals, so that the residual SG gravity values are assumed to contain the ocean tide loading gravity effects only. However, such an estimated ocean tide loading gravity effects will be highly dependent on the adopted solid earth tide model. As an experiment, we

removed the DDW solid earth tide of Dehant et al. (1999) from the raw SG gravity records. The remaining gravity values were then used to estimate ocean tide loading gravity effects at HS by ETERNA software. The estimated ocean tide loading gravity effects will be then called the “observed” ocean tide loading gravity effects. Fig. 4-5 shows the amplitudes of the “observed” ocean tide loading gravity effects at HS and the amplitudes of the ocean tide at the SHJU tide gauge station. In the amplitude spectra of Fig. 4-5, six leading components are identified: O_1 , P_1 , K_1 , N_2 , M_2 and S_2 . It is interesting to note that the relative magnitudes of these components are different between the ocean tide loading gravity effects and the ocean tide. For ocean tide loading gravity effects, the order is M_2 , O_1 , K_1 , S_2 , N_2 , and P_1 , while for the ocean tide, the order is M_2 , S_2 , N_2 , K_1 , O_1 , and P_1 . For both the ocean tide and its gravity effects, the M_2 component is dominant. For ocean tide, M_2 contributes 47% to the total signal, while for ocean tide loading gravity effect the M_2 contribution is only 23%. In addition to M_3 , several other non-linear tides are also present in Fig. 4-5. The SG observation in HS is used to study non-linear tides in the Taiwan Strait, as done by Boy et al. (2004) for European shallow waters.

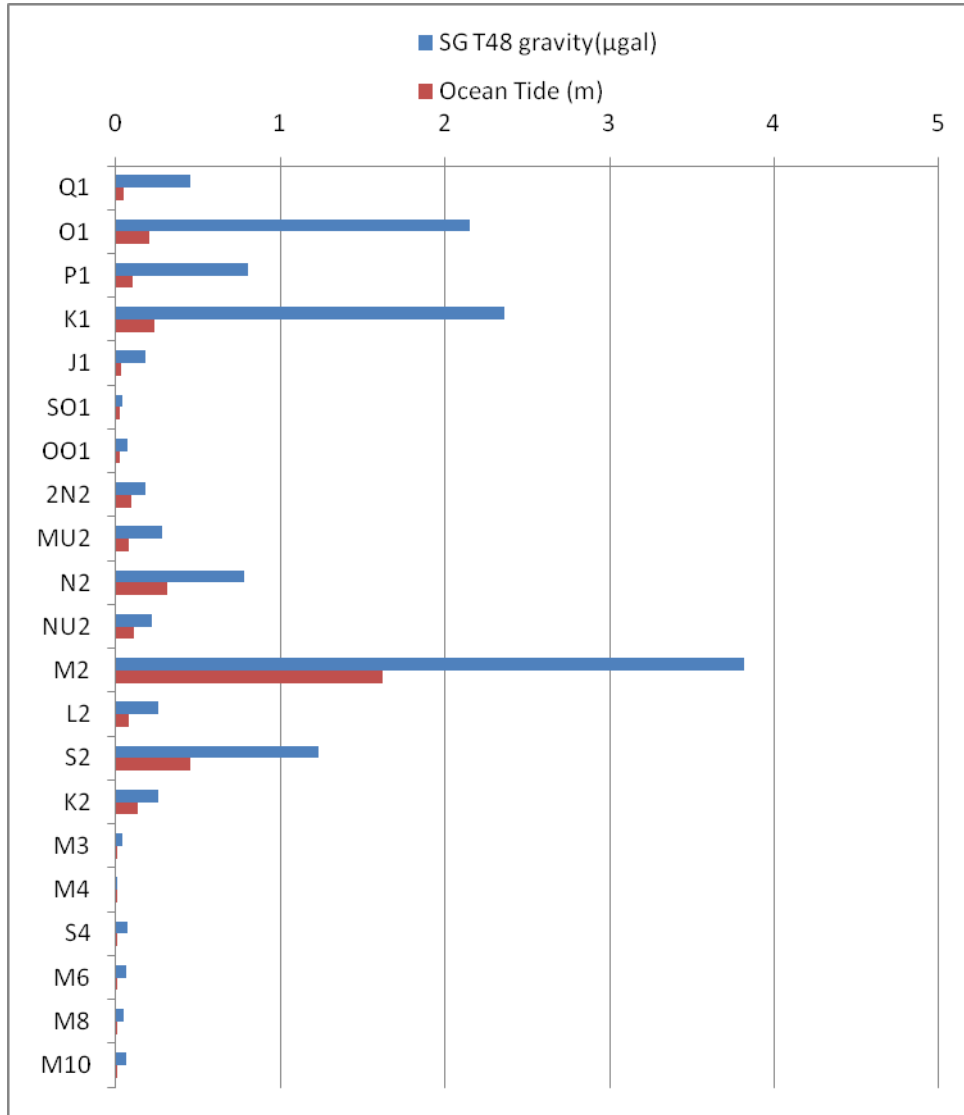


Fig. 4-5 Amplitudes of ocean tide from tide gauge records at the Hsinchu Harbor (8.6 km to HS), and amplitudes of ocean tide loading from the SG gravity measurements at HS

Table 4-4 compares the amplitudes and phases of the observations (T48), NAO.99b (Matsumoto et al., 2000), FES2004 (Lyard et al., 2006) and CSR4.0 (Eanes and Bettadpur, 1996) ocean tide models using ocean tide loading gravity effects for 8 short-period waves. Overall, the ocean tide loading gravity effects from the NAO.99b tide model agrees the best with the SG observations in both amplitudes and phases of

all tidal components. The model assessment by Penna et al. (2007) at TWTF, a continuous GPS station in Taiwan some 30 km north of HS, also shows that, compared to FES2004, the ground displacements predicted with NAO.99b are more consistent with the GPS observed displacements. The discrepancies in amplitude are at the sub- μgal level, except for the M_2 from CSR4.0. Compared with the diurnal tides, the modeled phases of the semi-diurnal tides show relatively large discrepancy and complexity in the Taiwan Strait. Therefore, there is room for improvement of the tide models listed in Table 4-4, especially in the phases of the semi-diurnal tides.

Table 4-4: Amplitudes and phases of ocean tide loading gravity effects at HS from T48 observations and from NAO.99b, FES2004 and CSR4.0 ocean tide models

Wave	T48	NAO.99b	FES2004	CSR4.0
M_2	3.82 ¹	3.76	3.37	2.85
	-98.0 ²	-99.6	-91.8	-122.2
N_2	0.84	0.82	0.75	0.93
	-79.1	-76.7	-58.9	-56.5
S_2	1.12	0.95	0.87	0.82
	-110.5	-114.4	-86.4	-42.7
K_2	0.26	0.24	0.25	0.31
	-103.1	-108.0	-81.9	-30.4
K_1	2.38	2.40	2.15	2.47
	-54.2	-55.1	-51.1	-58.9
O_1	2.10	2.08	2.01	2.13
	-33.2	-30.8	-34.1	-30.6
P_1	0.78	0.78	0.71	0.82
	-53.0	-52.8	-53.1	-56.7
Q_1	0.45	0.44	0.41	0.48
	-17.4	-22.4	-23.8	-23.3

¹amplitude in μgal , ²phase in degree

At a given SG station near the sea, the spatial variation of tidal height is assumed to be linear and the gravity effect of ocean tide is approximated as (Hwang et al., 2009)

$$g_i = C \frac{Gs_0\rho h}{4\pi R} \quad (4-3)$$

where s_0 denotes the radius of the near-zone zone, C denotes the ocean/land ratio near the station, and s_0 denotes the maximum distance that a linear variation of tidal height around the station holds. Based on the amplitude variation of M_2 in the Taiwan Strait (Jan et al., 2004), s_0 is about 10 km. That is, for a station near the sea, the Newtonian gravity effect is proportional to the tidal height. Using the integrations in Eq. (4-2) and the NAO.99b tide model, the largest Newtonian effect of ocean tide is found around Matzu, which is an offshore island in northwestern Taiwan Strait.

4.4 Comparison with theoretical solid earth tide

In order to demonstrate the uniqueness of the HS SG station at its latitude (about 25°N) and the effect of ocean tide loading gravity effects correction, we compared the observed gravity with the theoretical amplitude factors for selected waves in Table 4-5.

The theoretical amplitude factors in Table 4-5 are given by the DDW model of Dehant et al. (1999) for the elastic and inelastic earth, which are derived by the PREM earth model (Dziewonski and Anderson, 1981). The DDW amplitude factors are latitude-dependent and are expressed by

$$\begin{aligned}\delta_i^d &= a_i^d + b_i^d \frac{\sqrt{6}}{4} (7 \sin^2 \phi - 3) \\ \delta_i^s &= a_i^s + b_i^s \frac{\sqrt{3}}{2} (7 \sin^2 \phi - 1)\end{aligned}\tag{4-4}$$

where ϕ is latitude, subscript i stands for the tidal component, and superscripts d and s stand for diurnal and semi-diurnal waves, respectively. The second terms in Eq. (4-4) are the latitude-dependent terms contributing $\sim 0.4\%$ to the amplitude factors; see also Torge (1989). A “relative difference” in Table 4-5 is defined as the ratio between the absolute difference (observation – model) and the observation. Three global ocean tide models (NAO.99b, FES2004 and CSR4.0) were used to correct the ocean tide loading in the SG data.

Table 4-5: Amplitude factors from T48 observations and the DDW model

Wave	Factor from theory		T48 corrected by NAO.99			T48 corrected by FES2004			T48 corrected by CSR4.0		
	elastic	inelastic	factor	Elastic ¹	Inelastic ¹	factor	Elastic ¹	Inelastic ¹	factor	Elastic ¹	Inelastic ¹
ψ_1	1.2344	1.2656	1.3153	6.15	3.78	1.3088	5.68	3.30	1.3200	6.48	4.12
\emptyset_1	1.1672	1.1696	1.2175	4.13	3.93	1.2177	4.15	3.95	1.2186	4.22	4.02
OO_1	1.1547	1.1561	1.1556	0.08	0.043	1.1555	0.07	-0.05	1.1557	0.09	-0.03
K_1	1.1335	1.1355	1.1416	0.71	0.53	1.1420	0.74	0.57	1.1444	0.95	0.78
O_1	1.1527	1.1542	1.1661	1.15	1.02	1.1701	1.48	1.36	1.1646	1.02	0.89
N_2	1.1603	1.1617	1.1724	1.03	0.91	1.1500	-0.90	-1.02	1.1531	0.62	-0.75
P_1	1.1479	1.1493	1.1501	0.19	0.07	1.1541	0.54	0.42	1.1521	0.36	0.24
K_2	1.1603	1.1617	1.1640	0.32	0.20	1.1532	-0.62	-0.74	1.1304	2.65	2.77
Q_1	1.1527	1.1542	1.1379	-1.30	-1.43	1.1459	-0.59	-0.72	1.1308	-1.94	-2.07
M_2	1.1603	1.1617	1.1645	0.36	0.24	1.1564	-0.34	-0.46	1.1802	1.69	1.57
S_2	1.1603	1.1617	1.1623	0.17	0.05	1.1470	-1.16	-1.28	1.1278	2.88	3.01
M_3	1.0724	1.0734	1.0927	1.86	1.77	1.0926	1.85	1.76	1.0926	1.85	1.76

¹ relative difference in %

The amplitude factors corrected for the ocean tide loading effect agree better with the model factors of DDW than the factors from the raw SG data. In general, Table 4-5 shows that the inelastic model of DDW agrees better with the observations of T48 than the elastic model. Among three ocean models compared here, NAO.99b gives the corrected amplitude factors which are most consistent with the factors expected from the theory. In this case, if we take the mean value for the six major tidal components

having an amplitude exceeding $10 \mu\text{gal}$ (i.e. K_1 , O_1 , P_1 , N_2 , M_2 , and S_2), the relative difference for the inelastic model is about 22 % smaller than that for the elastic model, i.e. ratio of $(0.602-0.470)/0.602$. Moreover, for the mean of the same 6 components, we point out that the inelastic amplitude factor from the DDW (i.e. 1.1540) is slightly small compared to that from NAO.99b (i.e. 1.1595). It is necessary to further improve the accuracy of the ocean tide correction, especially for the M_2 and O_1 components, which have large amplitude and are far from the effect of the free core resonance (for example, Wahr, 1981) appearing around the frequency of K_1 and ψ_1 components.



Chapter 5 Modeling temporal gravity changes of non-tectonic origins

5.1 Atmospheric pressure effect

Time-dependent gravity variations sensed by a SG are caused by a number of phenomena. In this chapter, we model the gravity variations that are of non-tectonic origins (Torge, 1989), namely, the gravity effects due to atmosphere, hydrology, and polar motion. First, atmospheric pressure variations affect the gravimeter output in two ways: directly by the gravitational effect and indirectly by the deformation effect (Warburton and Goodkind, 1977). A simple Bouguer plate model of atmospheric pressure gravity effect is:

$$\delta g_p = A \delta p \quad (5-1)$$



where A is gravity-atmosphere admittance and δp is the pressure change. According to Chapter 3, the gravity-atmosphere admittance of T48 is $-0.35 \pm 0.003 \mu\text{gal hPa}^{-1}$ (average over the ETERNA and BAYTAP-G result), which is different from the standard value of $-0.3 \mu\text{gal hPa}^{-1}$ (Torge, 1989).

Atmospheric pressure cause temporal gravity changes which can amount to amplitudes (a few μgal) in the short-term, to a maximum of 20 μgal over several days, and 3 μgal over a season (Torge, 1989). Fig. 5-1 shows the raw atmospheric pressure records over 2006-2010 and the distribution of the pressure. The pressure shows a distinct seasonal variation and daily variation. Two clusters of pressure belonging to winters and summers are present in Fig. 5-1. These variations, and the highs and lows are typical for a sub-tropical as Taiwan where monsoonal winds are present.

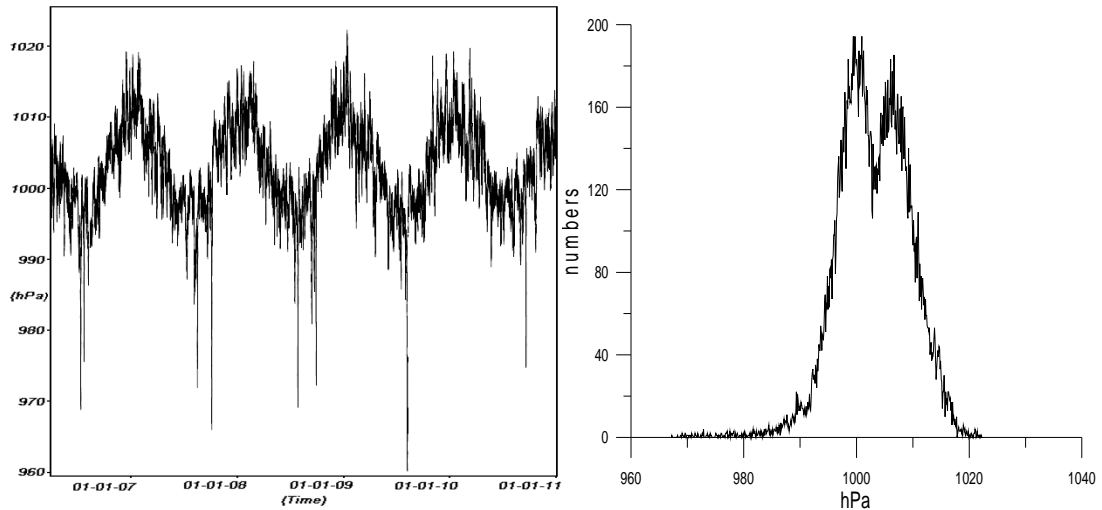


Fig. 5-1 Raw atmospheric pressure over 4/2006-12/2010 (left) and the distribution of the atmospheric pressure (right)

Fig. 5-2 shows the spectra of raw SG gravity and atmosphere pressure effect. Both spectra show evident peaks at frequencies associated with S_1 , S_2 , S_3 and S_4 . The variations of gravity at these frequencies are largely due to the variations of atmospheric pressure, with amplitudes of several μgal .

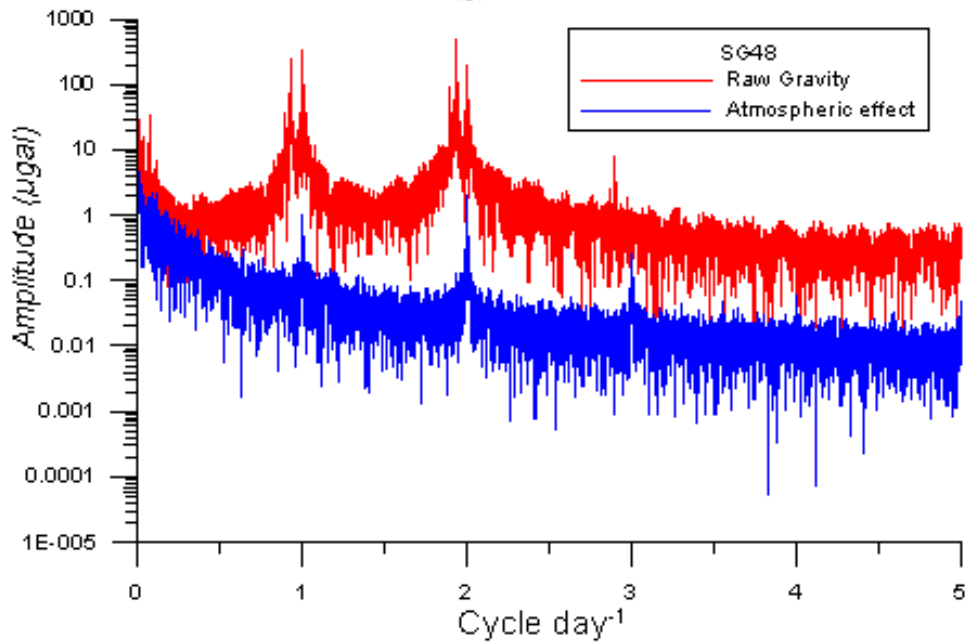


Fig. 5-2 Spectra of SG gravity (Red) and atmospheric pressure (Blue)

5.2 Hydrological effect

The hydrological gravity effect is largely due to variations in groundwater and soil moisture. Based on the model of a Bouguer plate and a homogeneous horizontal layer, the gravity effect of groundwater is computed by

$$\delta g_w = 2\pi G \rho_w P \delta H = 0.42 P \delta H \quad (5-2)$$

where P is the porosity of soil in percentage, ρ_w is the density and δH is groundwater level variation in m and the average of groundwater level is 24.54 m. For the soil moisture effect, we adopt $P=5\%$ as the optimal porosity for the Toukeshan formation so that

$$\delta g_s = 2\pi G \rho_w H \delta P = -0.65 H \delta P \quad (5-3)$$



where H is the depth of unsaturated soil layer and δP is the recorded soil moisture change in percentage. Here we adopt $H = 2$ m and the average of soil moisture is 14.2%. The minus sign in Eq. (5-3) is due to the fact that T48 is housed in a tunnel beneath the unsaturated soil.

5.3 Polar motion effect

Polar motion is the motion of the instantaneous rotating axis of the earth with respect to a mean axis. The motion of the axis results in change of gravity as

$$\begin{aligned} \delta g_p &= \delta_p \omega^2 R \sin 2\phi (x_p \cos \lambda - y_p \sin \lambda) \\ &= 1.164 \times 10^8 \omega^2 R \sin 2\phi (x_p \cos \lambda - y_p \sin \lambda) \end{aligned} \quad (5-4)$$

where ϕ, λ are latitude and longitude, ω is the angular velocity and x_p, y_p are polar motion components in radian, which are available from the international earth rotation service (IERS, <http://www.iers.org/>). The polar motion effect on SG represents a long periodic effect. Based on Torge (1989), and the dominating frequency is associated with the period (403 days) of Chandler wobble. Ocean tides will also lead to polar motion at shorter periods (diurnal and semi-diurnal periods), but their gravity effects are too small to be considered in this study.

5.4 Observations and models

We employ standard models as above to account for the gravity changes due to atmosphere, groundwater, soil moisture and polar motion at SG and AG stations in Taiwan. These models help to explain most of the origins of environmental effects associated with gravity changes and vertical motions from SG, AG and GPS observations at Taiwan. Fig. 5-3 compares the observed (by T48) residual gravity changes and the modeled values at HS. A summary on the non-linear gravity changes based on Fig. 5-3 are given below.

- (1) At the time scales of hours to days, the largest contribution to the observed residual gravity change is from the atmospheric pressure change. In fact, the analysis in Chapter 5-1 shows that the correlations between residual gravity change and atmospheric pressure change at such short time scales are more than 90% in most cases. The episodic changes of gravity due to groundwater have to do with sudden rainfalls. The soil moisture also creates short-period gravity variations, but the pattern of variation is quite irregular. There are no clear short-period gravity variations due to polar motions.

(2) The observed and modeled gravity changes all contain annual variations, but with different amplitudes and phases. Table 5-1 lists these amplitudes and phases. The amplitude of the groundwater gravity effect is the largest, followed by that of the atmosphere gravity effect. The amplitudes of the soil moisture and polar motion-induced annual gravity change are almost equal, and are 1/4 of the groundwater gravity effect. Seasonally, the modeled gravity changes due to atmosphere and groundwater lead the observed residual gravity by 109 and 62 days, while the modeled gravity changes due to soil moisture and polar motion lag behind the observed ones by about 12 days. Disagreements in amplitude and phase between observed gravity change and hydrology-induced gravity change are very common, as shown by Boy and Hinderer (2006) and Neumeyer et al. (2008) at selected GGP stations.

(3) Clearly the models in Eq. (5-1) to Eq. (5-4) have deficiencies, e.g., the 62-day phase difference between the observed and groundwater-induced gravity changes. On the other hand, the SG and AG observed gravity changes may be used to investigate such problems as flow of groundwater and small-scale hydrological process (e.g., Jacob et al., 2008; and Naujoks et al., 2008).

Table 5-1: Amplitudes and phases of the annual gravity change at HS by various factors

Source	Amplitude (μgal)	Phase ($^{\circ}$)
Observation (T48)	6.26	-26.09
Ground water	4.33	-88.32
Atmosphere	3.01	-135.25
Soil moisture	1.45	-14.02
Polar motion	1.54	-13.78

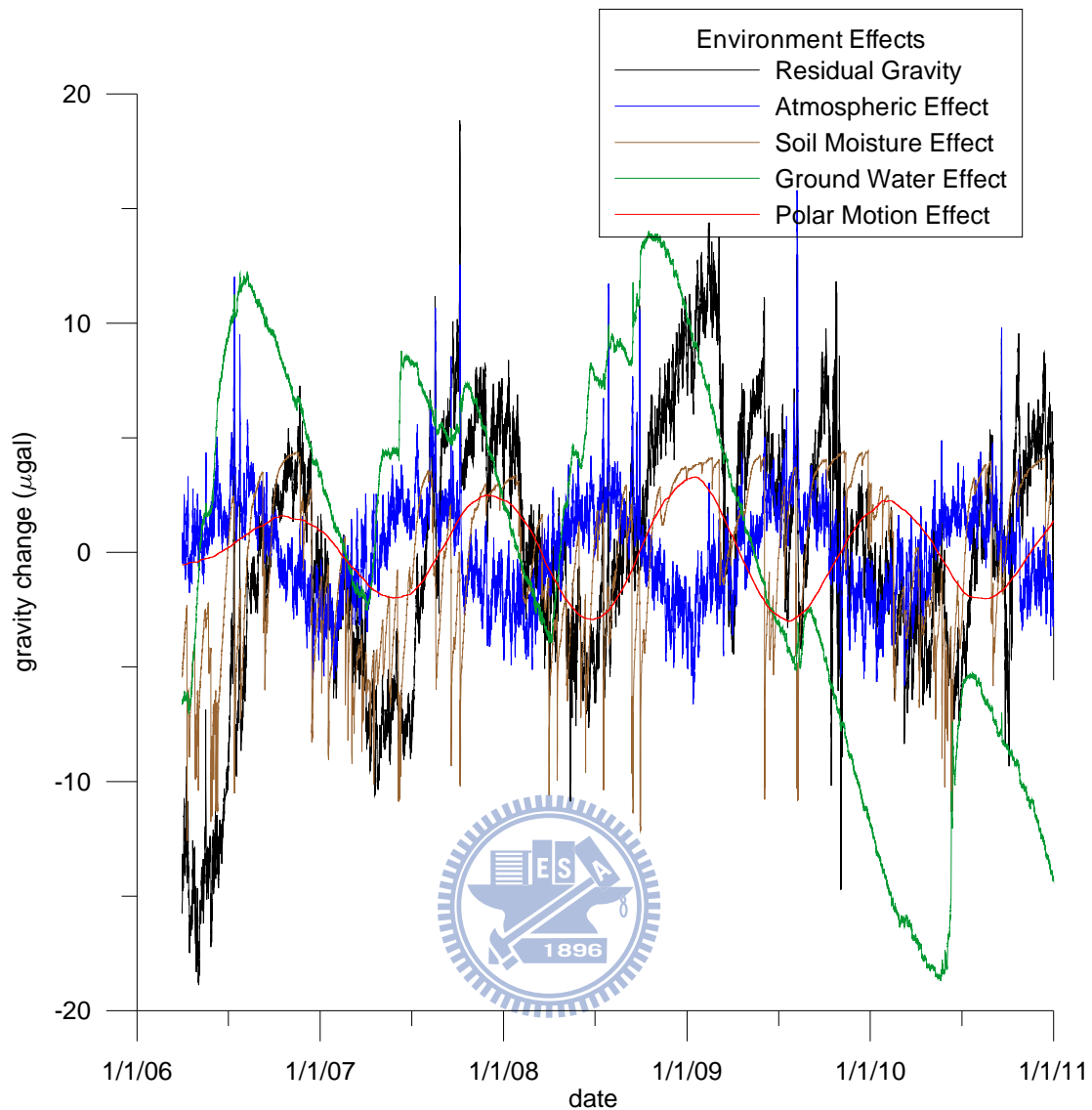


Fig. 5-3 Observed residual gravity changes (by T48, without the solid earth tide and ocean tide gravity effects) and modeled gravity changes at HS. The time starts from April 2006.

5.5 Rate of gravity change at Hsinchu

As shown in Chapter 3, the AG and T48 gravity records all show a long-term trend of gravity change at HS. The drifting rate of AG and SG are $2.2 \pm 0.3 \mu\text{gal year}^{-1}$ and $1.3 \pm 0.1 \mu\text{gal year}^{-1}$ from the AG and T48 measurements based on data from 2006 to 2011. The origins of the trend are now interpreted using the modeled gravity changes given above, plus the vertical displacement from GPS. The rates of the modeled gravity

changes are listed in Table 5-2. The total rate from these models is $-0.8 \pm 1.3 \mu\text{gal year}^{-1}$, which is different from the rate of $3.3 \mu\text{gal year}^{-1}$ based on data over 2006-2008 and is largely caused by the decrease of groundwater after 2008. Therefore, the modeled rates cannot fully account for the observed rate of gravity change. One source of the gravity change not accounted in Table 5-2 at HS is earthquakes around Taiwan. For example, the earthquake occurring on September 6, 2007 created the gravity offset of $0.6 \mu\text{gal}$, which contributes a rate of $0.3 \mu\text{gal year}^{-1}$ to the total rate at HS over five years. Other small earthquakes will also create gravity changes that eventually add to the rate of gravity change at HS. Gravity change due to sea-level rise will also contribute to the rate of gravity change recorded at HS. An example of gravity change due to sea level rise over the Baltic Sea is given by Virtanen and Makinen (2003). At the global scale, a rising rate of 3.1 mm year^{-1} in sea level, as estimated from TOPEX/Poseidon and Jason-1 satellite altimeter data (Nerem et al., 2006), will lead to a rate of $0.2 \mu\text{gal year}^{-1}$ in gravity change based on a simple Bouguer model for the effect of oceanic water mass.

Table 5-2: Modeled and FG5-observed rates of gravity change (in $\mu\text{gal year}^{-1}$) at HS

Source	Rate
Atmosphere	-0.1
Ground water	-2.1
Soil moisture	3.2
Polar motion	-0.1
Free-air motion of site	-0.1
Total	-0.8

Chapter 6 NGDS and gravity network in Taiwan

6.1 NGDS and its geological settings

The MOI established the NGDS in 2006 in Hsinchu. Several meteorological sensors and permanent GPS stations, a groundwater monitoring and a soil moisture sensor are deployed to monitor environment-induced gravity changes near the NGDS. As shown in Fig. 6-1, HS lies south of an alluvium created by two major rivers in Hsinchu. There are three non-active faults near HS. The Hsinchu Fault is within few hundreds of meter to HS and is a normal fault lying in the west-east direction with a total length of 8.6 km. The latest movement of the Hsinchu Fault occurred some 100,000 years ago (Central Geological Survey of Taiwan, <http://www.moeacgs.gov.tw/>), and it is expected that there will be no immediate threat of large ground movement and earthquake at HS due to this fault. HS is at the foot wall of the Hsinchu Fault and is situated on the “Toukeshan formation” that has a distinct geological structure from the alluvium to the north. The alluvium is fan-shaped and contains several soil layers. Fig. 6-2 shows a cross-section of the alluvium (Fig. 6-1). The depths of the layer with shallow groundwater range from 10 m to 40 m. Below this surface layer lies several layers composed of gravel and fine sand that can store groundwater. The amount of groundwater in these layers varies with rainfall, which is largely brought by monsoons and typhoons. As such, the seasonal or shorter time-scale changes of groundwater over the alluvium will create gravity variations at HS.

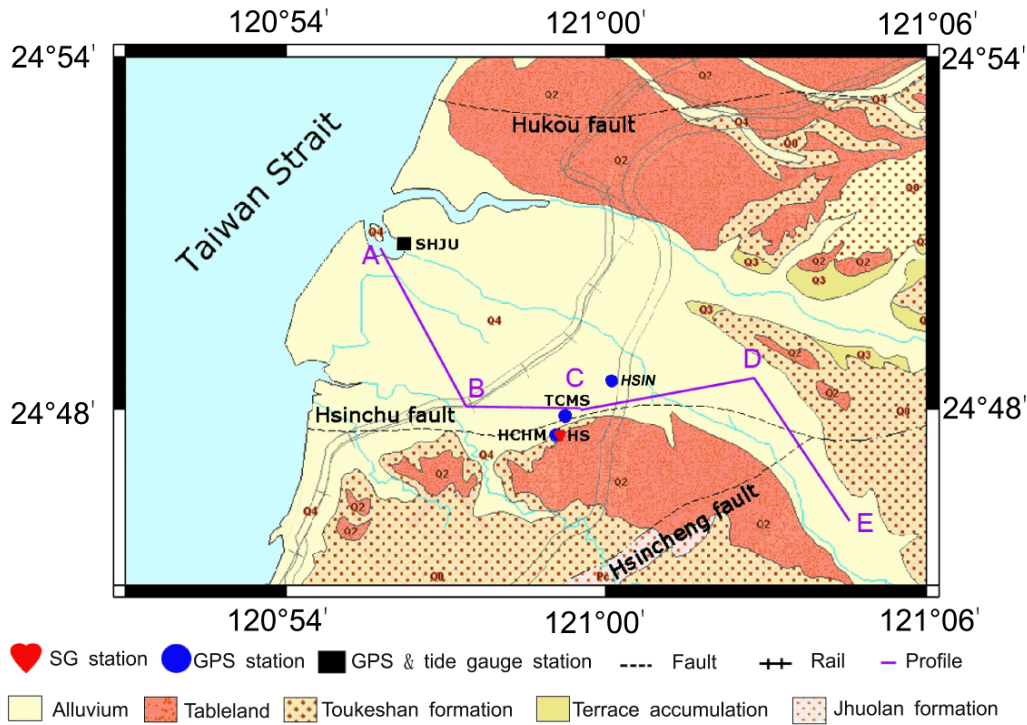


Fig. 6-1 Geological settings around the NGDS and distributions of GPS and tide gauge stations. The meanings of the formations are explained by documents in the Central Geological Survey of Taiwan.

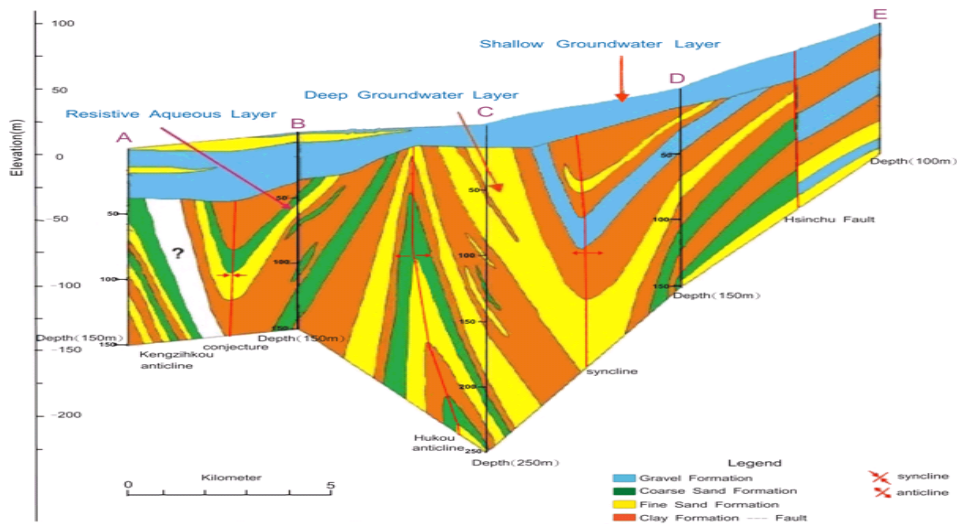


Fig. 6-2 A cross-section along the alluvium north of HS showing layers with shallow and deep groundwater. Deep groundwater takes time to fill and will delay groundwater-induced gravity change. The sampling points A, B, C, D and E are shown in Fig. 6-1

Depending on the spatial scale sought, the groundwater-induced gravity change is often classified into local, regional and global variations (in Chapter 5, a simple Bouguer model is used to account for the hydrological effect). For a precise modeling of the local groundwater effect, the local hydro-geology data must be given. At HS, the basic scenario of the hydro-geological structure is given in Fig. 6-1 and 6-2, but far more details are needed to account for the hydrology-induced gravity changes. The water table at HS alone cannot fully describe the distribution of groundwater over the Toukeshan formation around HS and over the alluvium north of HS. Furthermore, a soil moisture sensor is deployed right above Tunnel B that houses T48. However, the soil moisture data collected here will not be representative of water distribution in unsaturated layers around HS. Despite these difficulties, preliminary models to account for the residual gravity changes at HS due to non-geodynamic origin have presented in Chapter 5.

Compared to the eastern coast of Taiwan, the western coast of Taiwan is relatively quiet in terms of seismic activity. About 75% of earthquakes in Taiwan happen in the eastern coast, and 25% in the western coast (Central Geological Survey of Taiwan). Based on the GPS measuring results and a viscoelastic earthquake cycle model of Johnson et al. (2005), the horizontal rates of plate motion in southeastern Taiwan are about 7-8 cm year⁻¹, while the horizontal rates in the rest of Taiwan are few mm year⁻¹ to few cm year⁻¹. Here we used GPS data from four permanent GPS stations (Fig. 6-3), spanning the same time period (2006-2011) as that of the HS SG data, to study the regional tectonic motion around Hsinchu. Station HCHM is located on the summit of Mt. 18-Peak and is regarded as a co-located station with HS. The vertical rate is -0.2 ± 1.0 cm year⁻¹ and the trend of gravity is 1.3 ± 0.1 μ gal year⁻¹ (chapter 5.5) by T48. T48 Station TCMS is in the International GPS Service (IGS) network. Station SHJU is co-located with the Hsinchu tide gauge station. Using the IGS precised GPS orbits

(<http://igsceb.jpl.nasa.gov/>) and daily coordinates of the four GPS stations were determined and their variations in Fig. 6-3. In general, all permanent GPS stations show a consistent southeastward motion at a speed of about 2- 3 cm year⁻¹, and the pattern of horizontal motion in Fig. 6-3 is similar to that given by Johnson et al. (2005). Unlike the vertical motion, a localized and uniform horizontal motion will not create a significant mass change leading to gravity change.

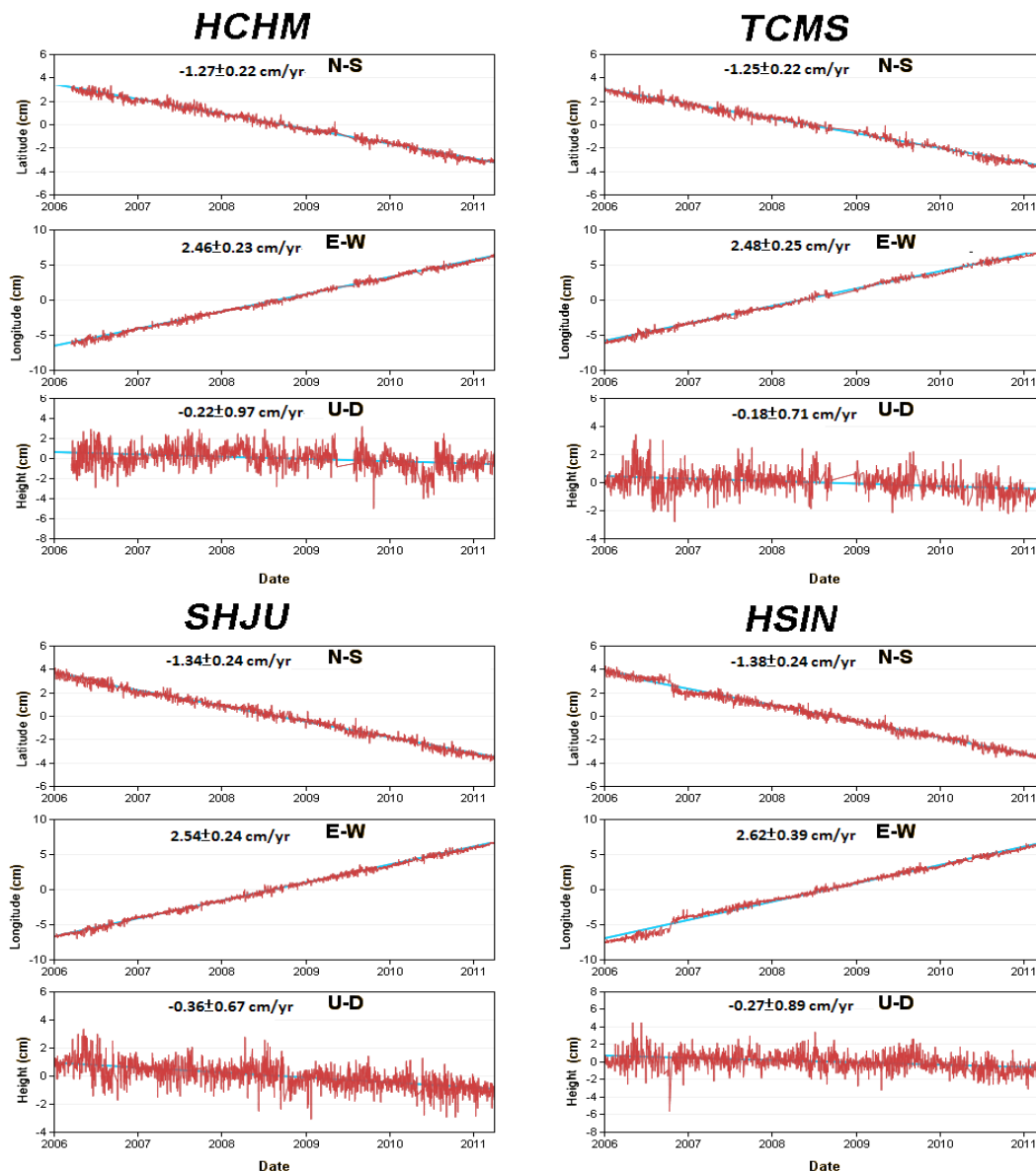
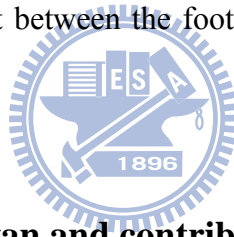


Fig. 6-3 The variations of coordinate are at the HCHM, TCMS, SHJU and HSIN permanent GPS stations. The numbers in the figure panels are linear rate of displacements from LSQ fits to the coordinate variations.

The vertical motions at the four GPS stations range from -0.18 to -0.36 cm year^{-1} . TCMS is several hundreds of meter from HCHM and is located on the top of a building. This station has been installed for over 10 years. Therefore, the subsidence of the buildings will not contribute to the vertical rates detected by GPS from 2006 to 2011. The SHJU tide gauge station, installed in 2004, is situated at the Hsinchu fishing harbor. Again the platform housing the SHJU tide gauge should be stable by 2006. The vertical rate of HCHM is -0.22 ± 0.97 cm year^{-1} . Since there is neither major man-made structure nor groundwater extraction near HCHM, the vertical motion at HCHM (and therefore at HS) should be of tectonic origin. Furthermore, the vertical rate of HCHM (at the foot wall) relative to TCMS (at the hanging wall) is -0.04 ± 1.2 cm year^{-1} , which shows that the relative vertical displacement between the foot wall and the hanging wall of the Hsinchu Fault is small.



6.2 An AG network in Taiwan and contribution to GGP

NGDS also establishes and maintains a network of absolute gravity sites on Taiwan and offshore islands. Fig. 6-4 shows the distribution of the AG sites, including those for the ATGO project. The gravity values at the AGTO sites are collected every November from 2006 to 2010 by a joint Taiwan-France team. Other gravity sites in Fig. 6-4 are occupied by AG irregularly. Measurements on some of the sites in Fig. 6-4 have been suspended. Repeated measurements of gravity values at most of these sites over different times yield gravity changes that were used for geodynamic studies. In Chapter 7, the gravity changes and their preliminary interpretations will be presented.

NGDS is also responsible for delivering SG data at HS to GGP. Taiwan joins GGP since 2006 and the SG data from Taiwan (HS) have been used by most of the SG scientists. In fact, GGP recommends that both AG and SG are submitted to the GGP

data center for a variety of purposes, including CF determination, SG drift estimation and regional plate tectonics study.

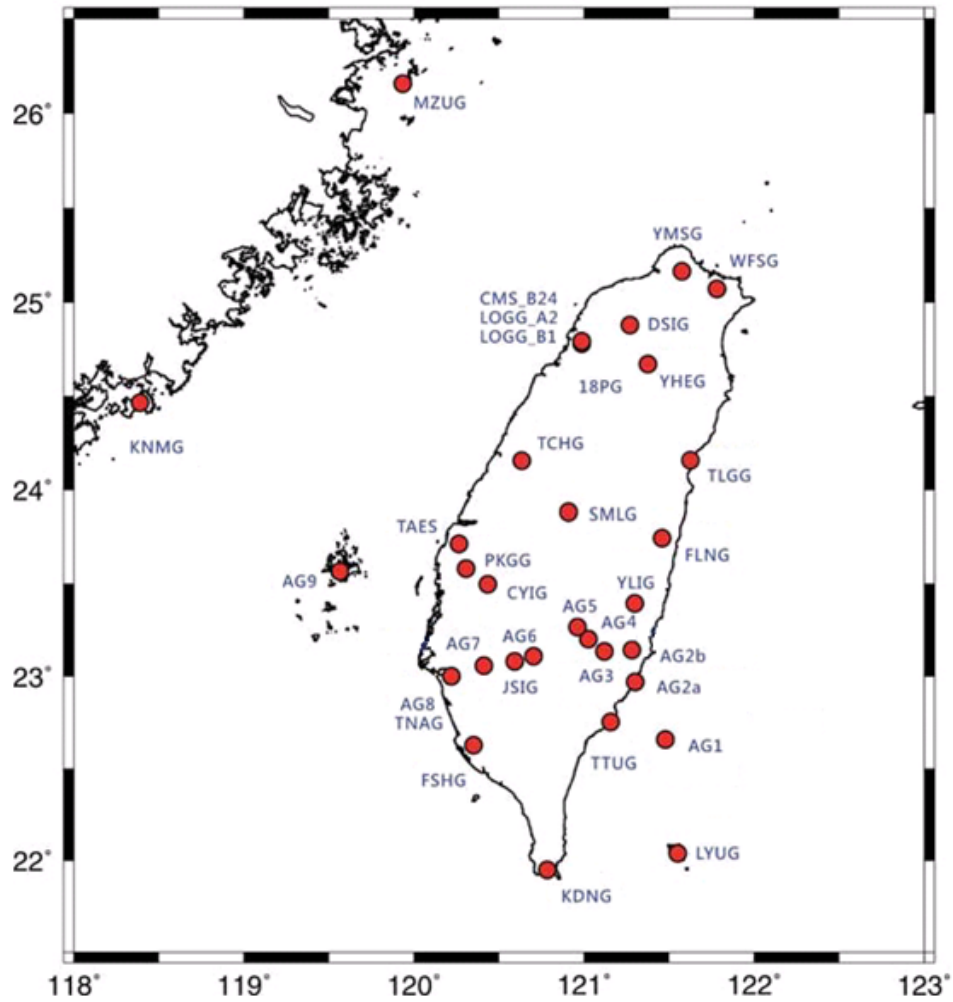
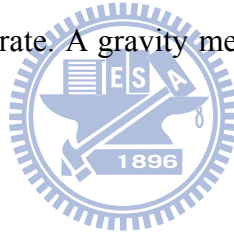


Fig. 6-4 Absolute gravity sites in Taiwan established by MOI

Chapter 7 Gravity changes from SG and AG in Taiwan

7.1 Estimation the drift of T48

This chapter will show results from the gravity measurement campaigns from 2006 to 2011. First, we assess the stabilities of the AG and SG gravimeters by comparing the drifts of both gravimeters at HS. In particular, the SG instrument drift should be determined so that the drift of SG will not lead to a false interpretation of the long-term gravity change at the SG site. Fig. 7-1 shows the parallel FG5 and SG observations at HS from 2006 to 2011, with the solid tide and ocean tide loading gravity effects and anomalous values removed. Some of the gravity values were collected by FG5 #224, FG5 #228 and FG5 #231 when SG was on the field work. These two time series of gravity, sampled at different time intervals, show a dominant annual cycle and an increasing rate. A gravity measurement from FG5 or T48, was modeled as



$$g(t) = g_0 + \dot{g}t + c \cos wt + d \sin wt + e(t) \quad (7-1)$$

where t is time, g_0 is a constant, \dot{g} is the linear rate, c and d are the coefficients of the annual cycle, w is the annual frequency, and e is the measurement noise. LSQ estimations were then employed to determine the four parameters in Eq. (7-1). The amplitude and phase were determined as $\sqrt{c^2 + d^2}$ and $\tan^{-1}(d/c)$. As a result, the amplitudes of the annual cycle from FG5 and T48 are 5.9 and 6.3 μgal , and the phases are -22.9° and -26.1° . The difference in phase is partly due to data errors and partly due to the two different ways of sampling FG5 and SG measurements. The measurements of SG were almost continuous (sampling rate is 1 Hz) from March 2006 to present, but

the measurements of FG5 were taken at the times given in Fig. 7-1, and each FG5 gravity value was the average over several drops. The linear change rates from FG5 and T48 are 2.2 ± 0.7 and $2.4 \pm 0.2 \mu\text{gal year}^{-1}$. If we assume that the rate obtained by the FG5 gravimeters is a true rate of gravity change, the instrumental drift of T48 is estimated to be at a rate of $0.2 \pm 0.7 \mu\text{gal year}^{-1}$. Note that this drifting rate ($0.2 \mu\text{gal year}^{-1}$) is estimated using the absolute gravity observations (FG5 #224, #228, and #231) from three FG5. It differs from the rate ($1.3 \mu\text{gal year}^{-1}$) estimated in Chapter 5. This is explained by the fact that the rate in Eq. (7-1) may also absorb other un-modeled effects in determination of the calibration factor and may not truly reflect the drift of T48. In conclusion, the observed drifting rate of T48 (vs. FG5 rate) is well smaller than the nominal drift of $0.6 \mu\text{gal year}^{-1}$ claimed by the manufacturer. Also, the two FG5 AG appear to function well and is without a instrument drift problem.

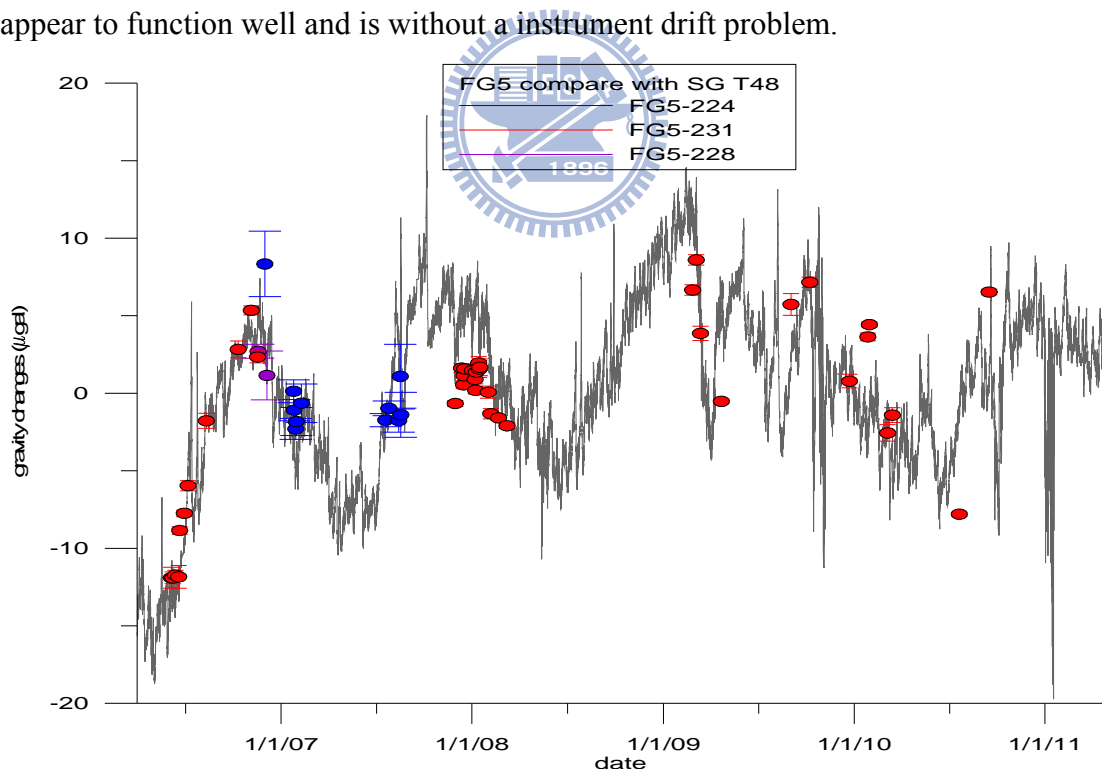


Fig. 7-1 Comparison of SG and FG5 measurements are from 2006-2011. The FG5 gravimeter #228 is from France while #224 and #231 are from Taiwan.

7.2 Gravity changes from project AGTO

Taiwan is located at the converging zone of the Eurasia Plate and the Philippine Sea Plate. The tectonic motions create vertical displacements and mass changes that may be detected by repeated gravimetric and GPS measurements. A joint Taiwan-France project, called AGTO, was initiated in 2006 to study the orogeny of Taiwan using gravimetry and GPS. The AGTO used gravimeters (FG5 #228) from France and from Taiwan (FG5 #224). In this project, ten gravity-GPS sites (Table 7-1) along an east-west transect across southern Taiwan have been selected for gravity and GPS (Fig. 7-2) measurements, which are used to analyze vertical movements and mass transfers due to orogeny. Because the gravity effects of soil moisture and groundwater are mostly seasonal, we collect absolute gravity values in the same month of the years (November) to reduce the hydrological effect. The gravity changes collected over 2006 to 2010 at most sites was explained by the vertical movements from GPS, but large environment-induced gravity effects lead to significant conflicts between the gravimetric and GPS results. For example, typhoon Morakot (August 2008) caused large landslides that led to gravity change of 53 μgal at AG3 and 27 μgal at AG6 (Fig. 7-3). Here orogeny-induced gravity changes are significantly interrupted by such extreme events as typhoon Morakot.

With the river sediment data from Water Resource Agency (WRA) of Taiwan and satellite images of FORMOSAT-2 from National Space Organization (NSPO) before and after Morakot (Fig. 7-4), such gravity changes were used to estimate the sediment thickness based on a simple Bouguer plate model (Torge, 1989):

$$H \times p\% = \frac{24}{\delta\rho} \delta g \quad (7-2)$$

where $\delta\rho$ is the density of sediments in kg/m^3 in the riverbed, $p\%$ is the percentage area of the sediments and δg is the gravity change e in μgal at AG site. The sediment densities range from 1300 to 1800 kg/m^3 . Fig. 7-5 shows the sediments near AG6. Within a radius of one km, there is 40 percent area lying in the riverbed. Based on the gravity changes at AG3 and AG6, the sediment thicknesses of H which was near AG6 range from 1.76 to 2.45 m, and the sediment thicknesses near AG3 range from 0.90 to 1.25 m.

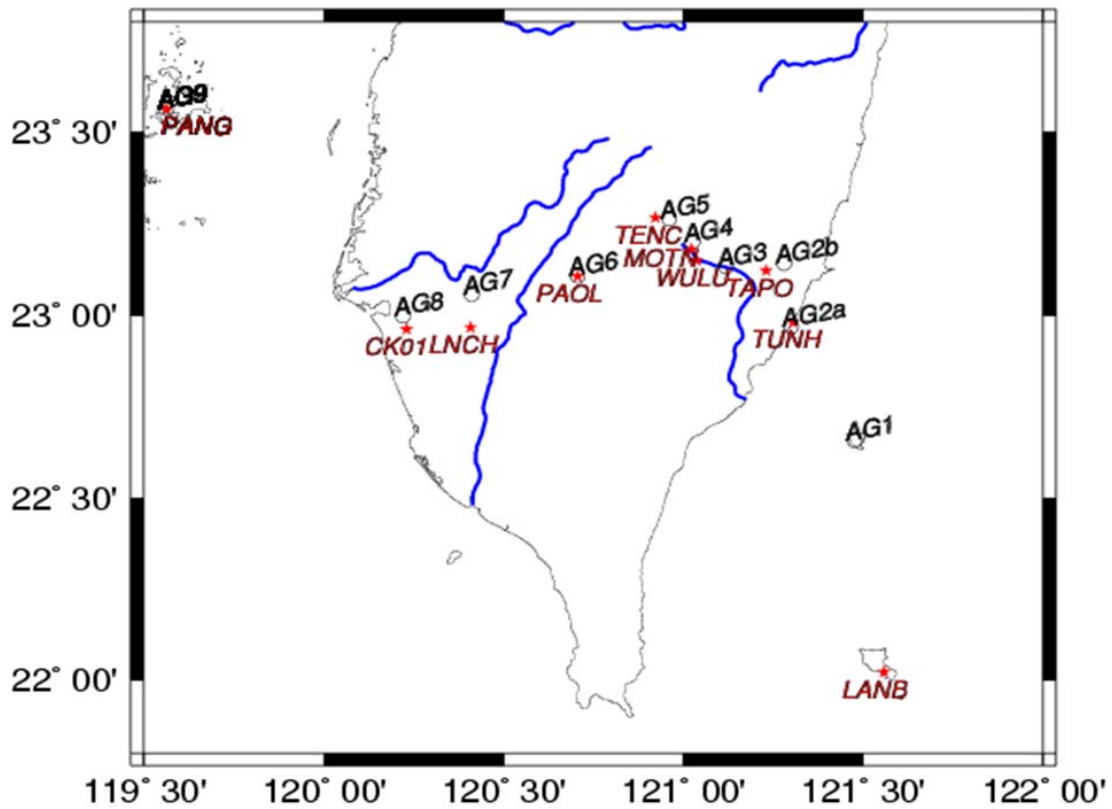


Fig. 7-2 AG sites in the project AGTO (circle) and GPS sites (star)

Table 7-1: The Location of AG and GPS sites

AG	Location (Lat, Lon)	GPS	Location (Lat, Lon)
AG1	(22.658°, 121.476°)	LANB	(121.439°, 22.023°)
AG2a	(22.970°, 121.300°)	TUNH	(121.186°, 22.982°)
AG2b	(23.142°, 121.280°)	TAPO	(121.111°, 23.124°)
AG3	(23.133°, 121.119°)	WULU	(120.917°, 23.151°)
AG4	(23.201°, 121.026°)	MOTN	(120.933°, 23.182°)
AG5	(23.264°, 120.961°)	TENC	(120.802°, 23.269°)
AG6	(23.109°, 120.706°)	PAOL	(120.587°, 23.108°)
AG7	(23.057°, 120.412°)	LNCH	(120.289°, 22.969°)
AG8	(22.999°, 120.220°)	CK01	(120.111°, 22.963°)
AG9	(23.565°, 119.563°)	PANG	(119.543°, 23.565°)

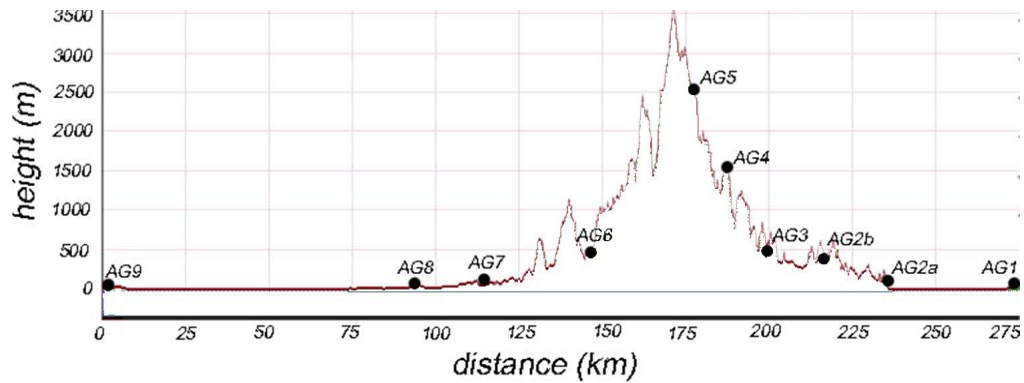


Fig. 7-3 The elevation of AG sites in the project AGTO, AG3 and AG6 are located at the mid-slope of a mountain

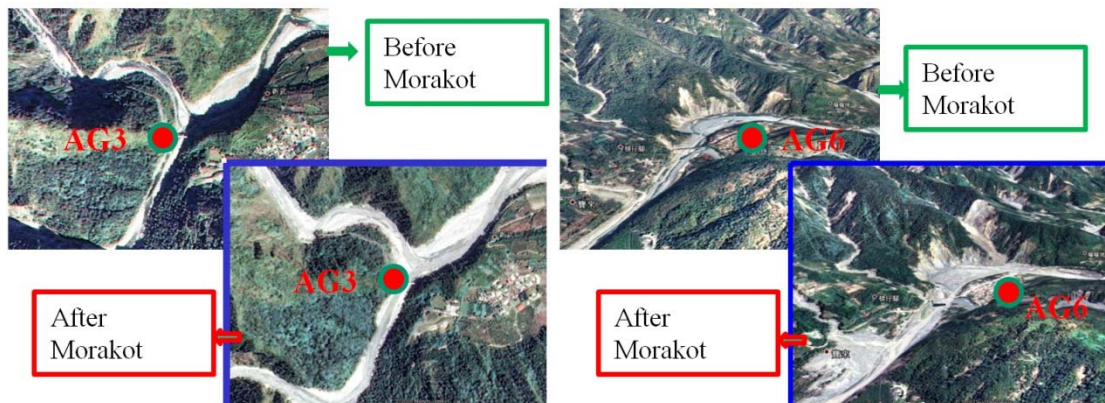


Fig. 7-4 Formosat-2 images of AG3 and AG6 before and after Morakot

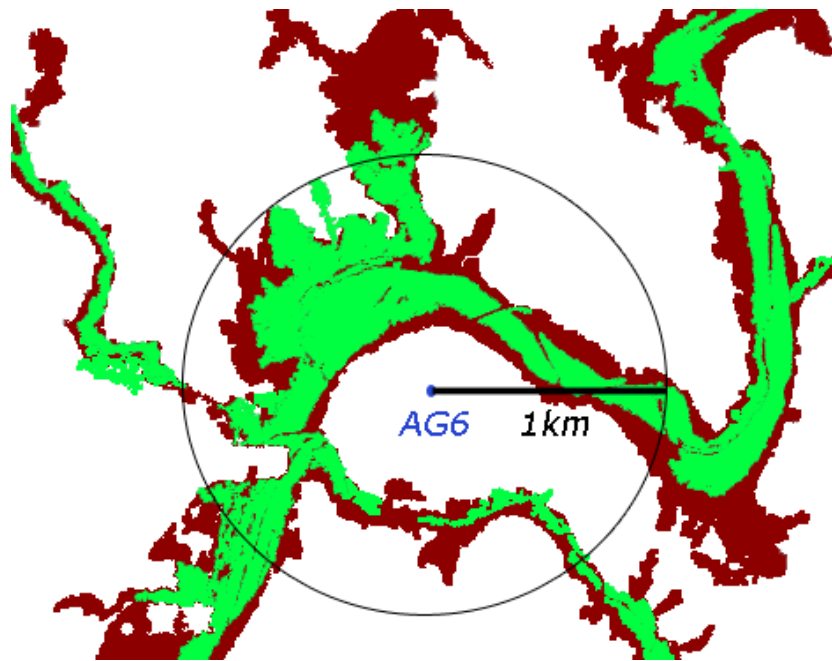


Fig. 7-5 Accumulation of soil and rock in the riverbed near AG6 due to Morakot (brown), and the original riverbed (green)

Typhoon Morakot caused erosions mainly at foothills and high mountains, rather than flat areas. The erosions lead to gravity changes at some of the AGTO sites. This difference in erosion was seen from the gravity changes at ATGO sites. For example, compared to other AGTO sites, the gravity changes at AG3 and AG6 are significantly larger. AG3 and AG6 are situated at foothills. Based on Fig. 7-3, the height difference between AG6 and AG7 is less than 300 m, while the height difference between AG6 and AG5 is over 2000 m. Likewise, the height difference between AG3 and AG2b is less than 200 m, while the height difference between AG3 and AG4 is over 1000 m. The height difference and location (foothill vs. high mounts/flat area) explain partially why the gravity changes at AG3 and AG6 are significantly larger than others.

The atmospheric gravity effect for AG data at the AGTO sites is based on the average admittance of -0.35. Also, there are no groundwater and soil moisture

observations near all AGTO sites to model the hydrological effect. However, because all the observations were made in November, we expect that the hydrological effect is reduced when differencing gravity observations between two successive years at the same site. Table 7-2 summarizes the gravity values relative to the values in 2006; see also Fig. 7-6. Some of the gravity values are suspicious and outliers, e.g., the gravity value at AG8 in 2007. The large gravity values at AG3 and AG6 in 2009 are caused by typhoon Morakot. Table 7-3 shows the rates of gravity changes at the AGTO sites. The rates are computed without using the anomalous gravity values caused by typhoons. The gravity rates are compared with vertical displacement rates from GPS. The gravity rate varies from one station to another. The average gravity and vertical rates are $-1.39 \pm 4.21 \mu\text{gal year}^{-1}$ and $0.50 \pm 0.94 \text{ cm year}^{-1}$, respectively, leading to an average gravity-height ratio ($2.78 \mu\text{gal cm}^{-1}$). This ratio is different from the ratio of $2.0 \mu\text{gal cm}^{-1}$ based on a vertical displacement a Bouguer plate with a rock density of 2.67 g cm^{-3} . The difference between the observed and theoretical ratios (2.78 and $2.0 \mu\text{gal cm}^{-1}$) is a subject of future study

Table 7-2: Gravity changes relative to observations in 2006

Sites	2006 (μgal)	2007 (μgal)	2008 (μgal)	2009 (μgal)	2010 (μgal)
AG1	0	6.15	1.28	-2.6	-0.23
AG2a	0	3.11	-0.64	-1.68	4.01
AG2b	0	5.47	-1.17	-7.74	-5.37
AG3	0	-8.1	-14.44	38.35	61.21
AG4	0	-0.77	5.82	-6.86	1.25
AG5	0	-0.84	1.94	--	--
AG6	0	1.46	2.93	30.01	27.65
AG7	0	3.44	-1.79	-6.86	-6.9
AG8	0	-45.87	-7.84	-13.92	-9.28
AG9	--	0	-1.61	-4.45	-0.36

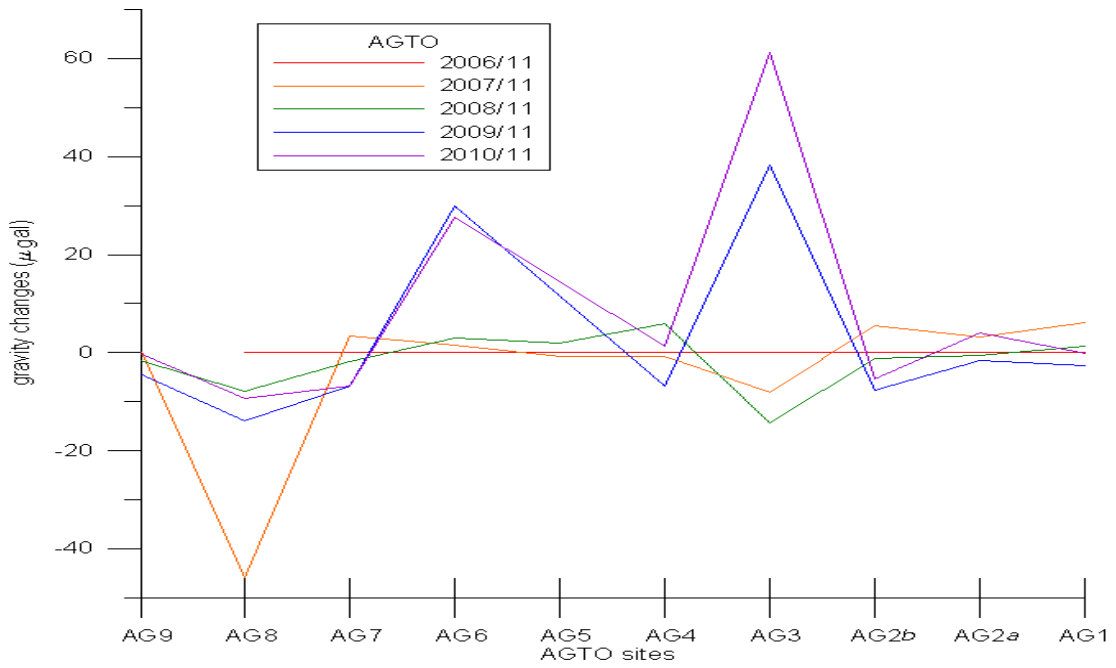


Fig. 7-6 Gravity changes relative to observations in 2006 at AGTO sites (each curve represents a year)

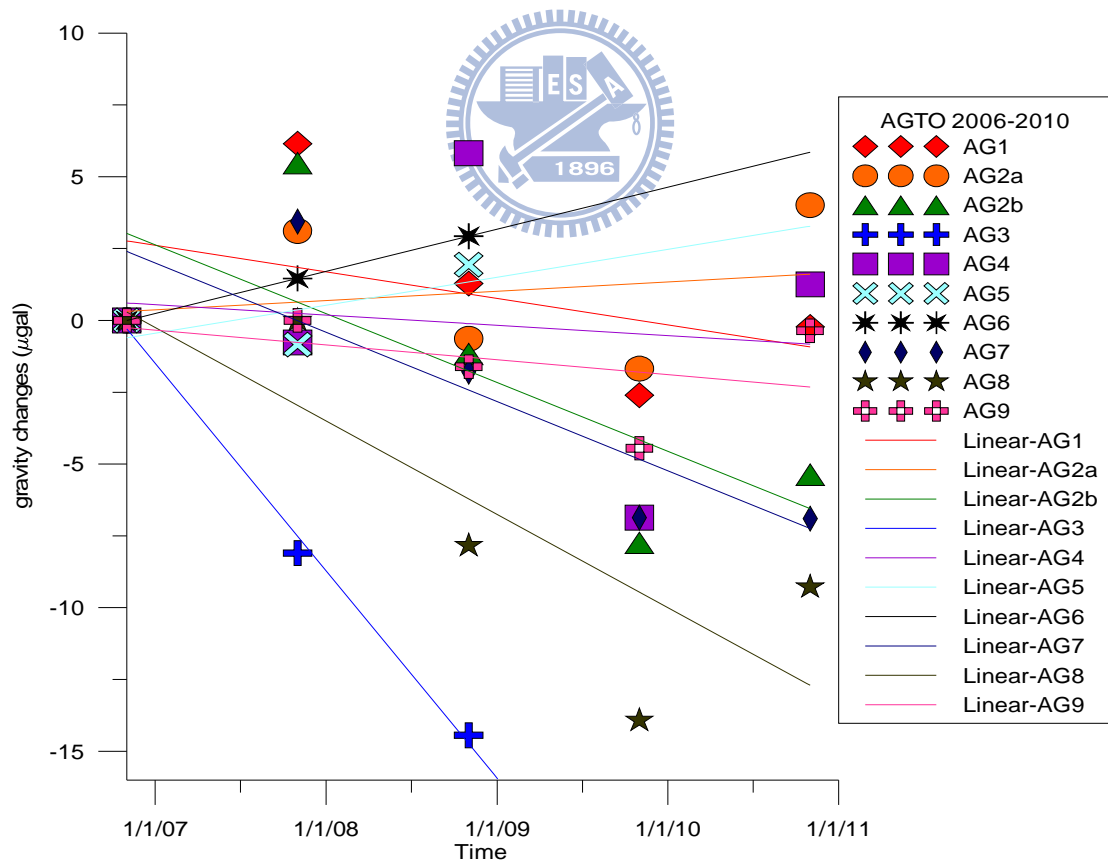


Fig. 7-7 Gravity changes relative to the observations in 2006 at the AGTO sites (each curve represents a site)

Table 7-3: Gravity changes relative to observations in 2006

Sites (AG/GPS)	Gravity rate ($\mu\text{gal year}^{-1}$)	GPS rate (cm year^{-1})
AG1/LANB	-0.92±3.24	-0.07±1.10
AG2a/TUNH	0.32±2.47	0.09±0.84
AG2b/TAPO	-2.39±5.11	1.11±0.87
AG3/WULU	-7.21±7.24	0.82±1.04
AG4/MOTN	-0.36±4.56	0.25±1.07
AG5/TENC	0.97±1.43	0.05±0.99
AG6/PAOL	1.46±1.47	1.02±0.89
AG7/LNCH	-2.41±4.49	1.59±0.99
AG8/CK01	-2.82±5.79	0.30±0.88
AG9/PANG	-0.52±2.02	-0.14±0.57
AVERAGE	-1.39±4.21	0.50±0.94

7.3 Gravity changes from MOI AG campaigns

In addition to the AGTO sites, we also collected AG data at 15 MOI-defined gravity sites over the entire Taiwan and some offshore islands (Fig. 6-4). Some of sites were just visited once. At the MOI sites, we also observed gravity gradients for AG data reductions (Chapter 2), and the result is given in Table 7-4. Most of the gravity gradients are different from the normal gradient of $-0.3086 \text{ mgal m}^{-1}$, suggesting that the rock densities at these sites are different from 2.67 g cm^{-3} and large gravity anomalies may have further caused the substantial deviations of the observed gradients from the normal gradient.

Table 7-5 lists the gravity values in 2005 and 2008. Fig. 7-8 to Fig. 7-22 shows the gravity values from 2005 to 2010. Table 7-6 shows the rates of gravity change from 2004 to 2010. The average rate of gravity change is $-0.58 \mu\text{gal year}^{-1}$.

Table 7-4: Gravity gradients at 15 MOI sites

Site	gradient ($\mu\text{gal cm}^{-1}$)
18PG	-3.26 ± 0.11
CYIG	-3.15 ± 0.06
DSIG	-3.31 ± 0.07
FLNG	-2.90 ± 0.03
HCHG	-2.60 ± 0.06
JSIG	-2.90 ± 0.06
KDNG	-3.39 ± 0.02
LYUG	-4.30 ± 0.28
PKGG	-2.72 ± 0.03
SMLG	-3.52 ± 0.01
TAES	-3.09 ± 0.04
TCHG	-2.72 ± 0.15
TLGG	-2.31 ± 0.02
WFSG	-4.00 ± 0.05
YHEG	-2.44 ± 0.01
YLIG	-2.32 ± 0.06
YMSG	-3.61 ± 0.06

Table 7-5: Absolute gravity values and uncertainties in 2005 and 2008 at MOI sites

Site	2005		2008	
	Gravity ¹ (μgal)	uncertainty (μgal)	gravity (μgal)	uncertainty (μgal)
18PG	--	--	820.2	2.1
CYIG	906.5	2.2	--	--
CYIG	--	--	694.3	2.2
DSIG	684.4	2.2	675.6	2.1
FLNG	--	--	165.4	2.1
HCHG	698.6	2.2	008.7	2.0
JSIG	627.5	2.1	618.7	2.0
KDNG	504.9	2.2	512.5	2.0
LYUG	--	--	130.4	2.1
PKGG	--	--	864.0	2.1
SMLG	464.6	2.1	442.4	2.0

TAES	--	--	793.2	2.2
TCHG	510.2	2.1	477.4	2.1
TLGG	583.2	2.1	581.5	2.1
WFSG	887.6	2.1	894.0	2.1
YHEG	735.3	2.1	710.5	2.0
YDIG	891.7	2.1	894.4	2.1
YMSG	909.0	2.1	888.7	2.0

¹relative to the mean value

Table 7-6: Rates of gravity change at MOI sites

Site	Duration	Times	Gravity rate ($\mu\text{gal year}^{-1}$)
DSIG	2005-2009	2	-2.14
FLNG	2006-2009	8	0.72
HCHG	2004-2009	4	-1.37
JSIG	2005-2009	2	-2.63
KDNG	2004-2009	8	-6.98
LYUG	2004-2009	2	-0.73
PKGG	2006-2009	7	6.49
SMLG	2005-2009	2	-5.91
TAES	2004-2009	6	16.23
TCHG	2005-2009	2	-8.99
TLGG	2005-2008	2	-0.58
WFSG	2005-2008	2	0.71
YHEG	2005-2009	2	-6.06
YDIG	2005-2008	2	0.93
YMSG	2004-2010	10	1.68

Some of the gravity changes given in Fig. 7-8 to 22 are explained below. TAES is located in Yunlin County and is over an area of large subsidence. Here the gravity rate is $16.2 \mu\text{gal year}^{-1}$, corresponding to a subsidence rate of 8.1 cm year^{-1} , provided that the rock density is about 2.67 g cm^{-3} and there is no significant plate motion here. Like TAES, PKGG is also situated over an area of subsidence, and the gravity change here is

largely caused by subsidence, but with a smaller subsidence of 3.2 cm year^{-1} compared to that of TAES. YMSG is visited most frequently among all stations. Here the gravity rate is $1.68 \text{ } \mu\text{gal year}^{-1}$ and it has been hypothesized that this gravity increase is potentially caused by the rise of magma in the Tatun volcano groups. More evidence is needed to support this hypothesis.

Virtually all gravity sites along the Central Range show negative rates ranging from $-5.91 \text{ } \mu\text{gal year}^{-1}$ (SMLG) to $-6.06 \text{ } \mu\text{gal year}^{-1}$ (YHEG). Station TCHG is situated in the city center of Taichung and also experiences a large, negative rate of $-8.99 \text{ } \mu\text{gal year}^{-1}$. Despite fact that the gravity point density is low, in Fig. 7-23 we show a two-dimensional (also lateral) distribution of gravity rates over the entire Taiwan. In order to correlate the gravity changes with vertical displacements, in Fig. 7-24 we show the rates of horizontal displacement and vertical displacement derived from more than 300 continuous GPS stations (see Appendix 1). Because mass transfer originating from the orogeny of Taiwan is at the sub- μgal level (Mouyen et al., 2009), the gravity rates in Fig. 7-23 are largely explained by the vertical displacements given in Fig. 7-24, based on a simple Bouguer model that translates a one-cm plate uplift to a $2 \text{ } \mu\text{gal}$ gravity decrease. However, deviations from such a simple Bouguer model can occur under the following conditions:

- (1) Man-made movement of gravity site
- (2) Large subsidence such as TAES
- (3) Large hydrological effect not removed from the gravity observation
- (4) Data errors
- (5) Anomalous subsurface mass movement such as magma at YMSG

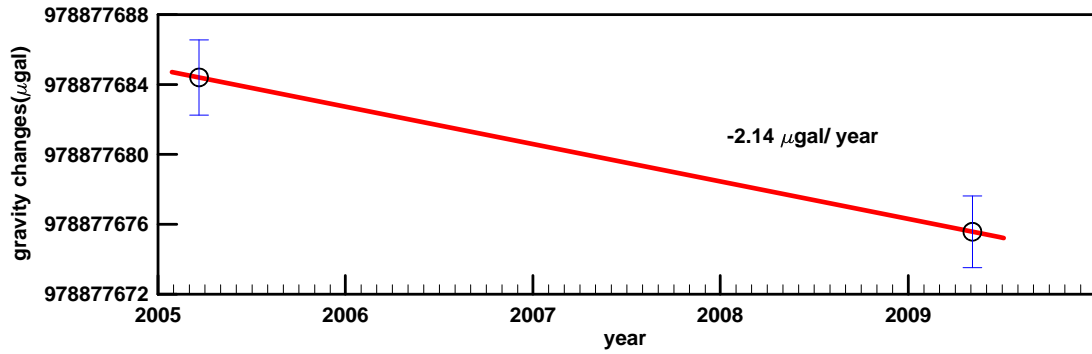


Fig. 7-8 Absolute gravity values and rate at DSIG

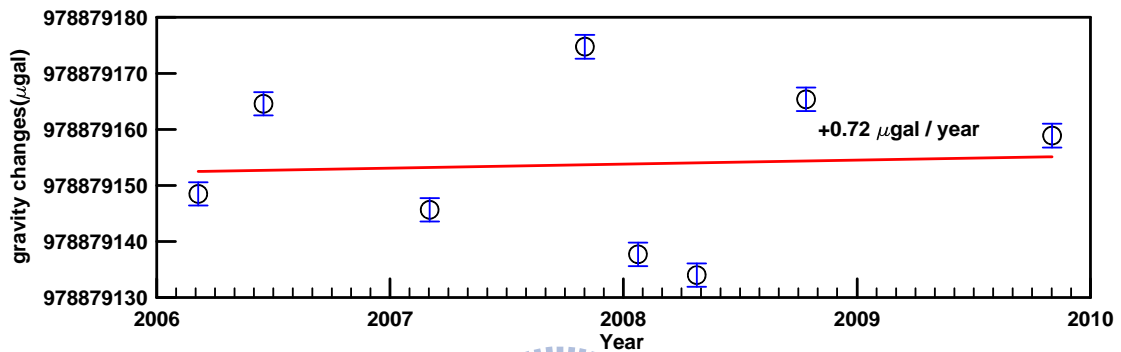


Fig. 7-9 Absolute gravity values and rate at FLNG

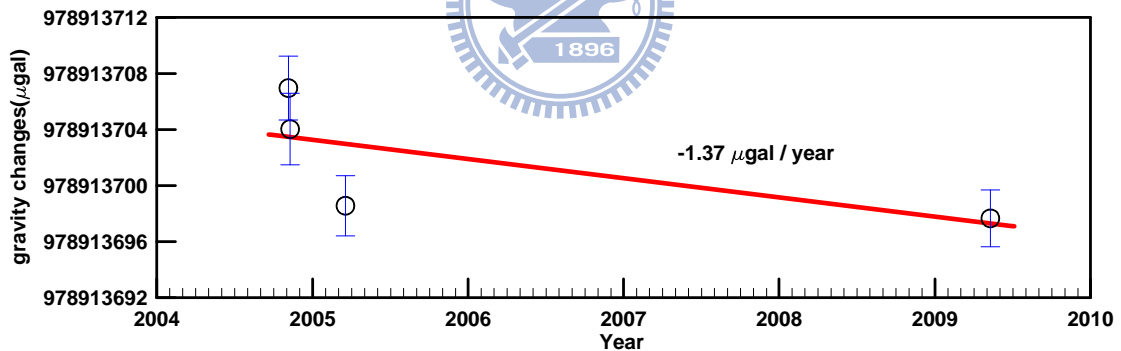


Fig. 7-10 Absolute gravity values and rate at HCHG

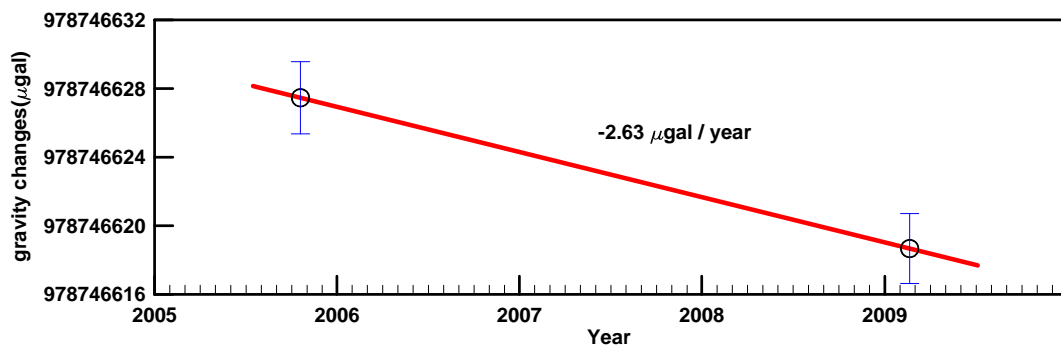


Fig. 7-11 Absolute gravity values and rate at JSIG

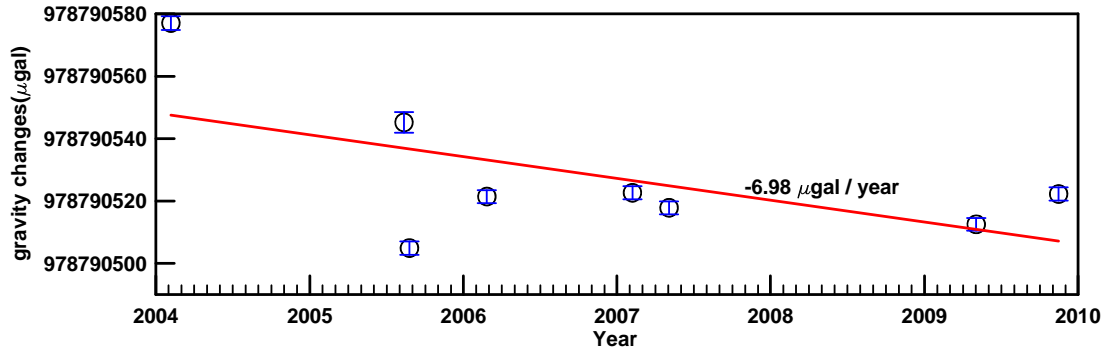


Fig. 7-12 Absolute gravity values and rate at KDNG

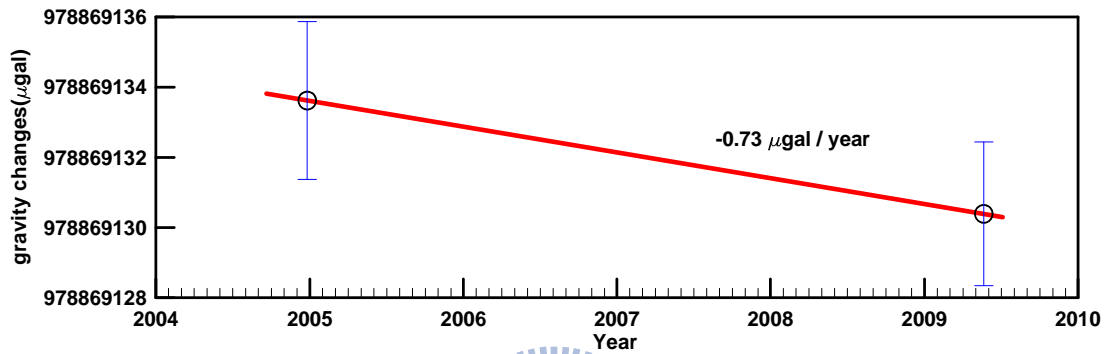


Fig. 7-13 Absolute gravity values and rate at LYUG

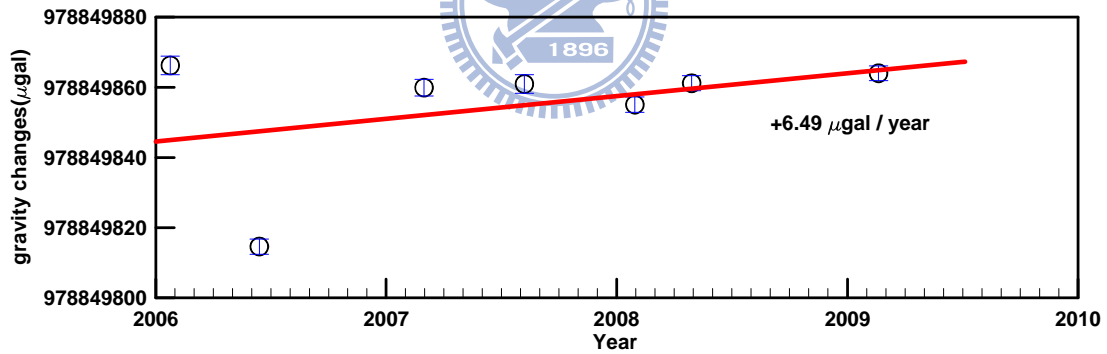


Fig. 7-14 Absolute gravity values and rate at PKGG

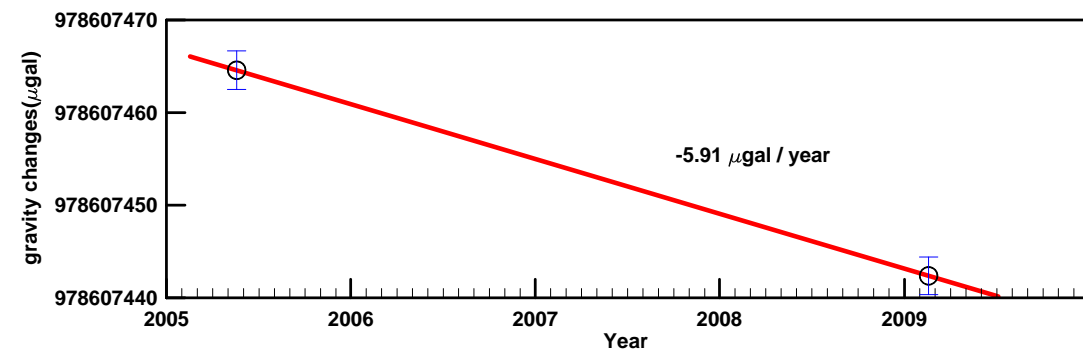


Fig. 7-15 Absolute gravity values and rate at SMLG

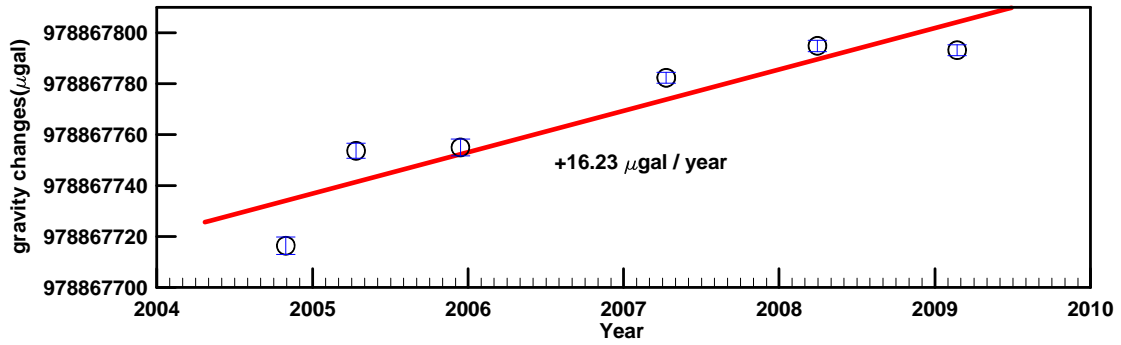


Fig. 7-16 Absolute gravity values and rate at TAES

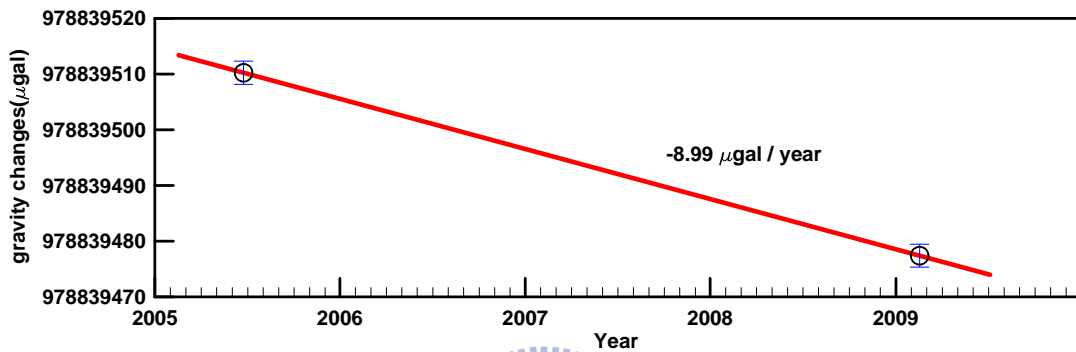


Fig. 7-17 Absolute gravity values and rate at TCHG

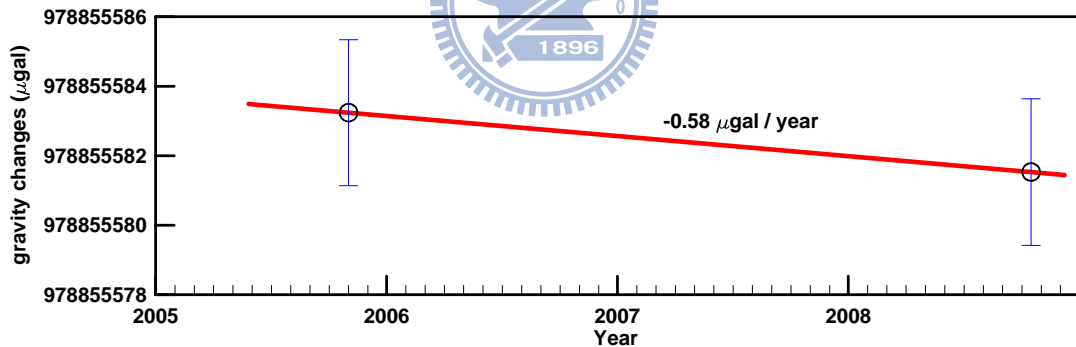


Fig. 7-18 Absolute gravity values and rate at TLGG

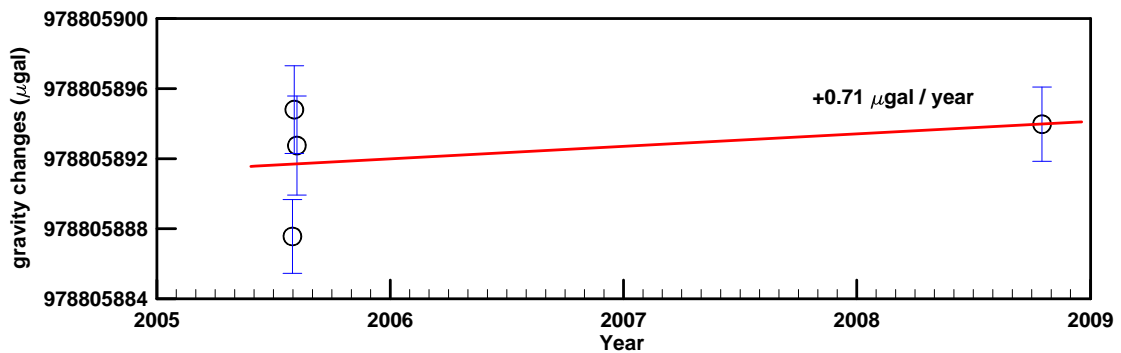


Fig. 7-19 Absolute gravity rate of WFSG station

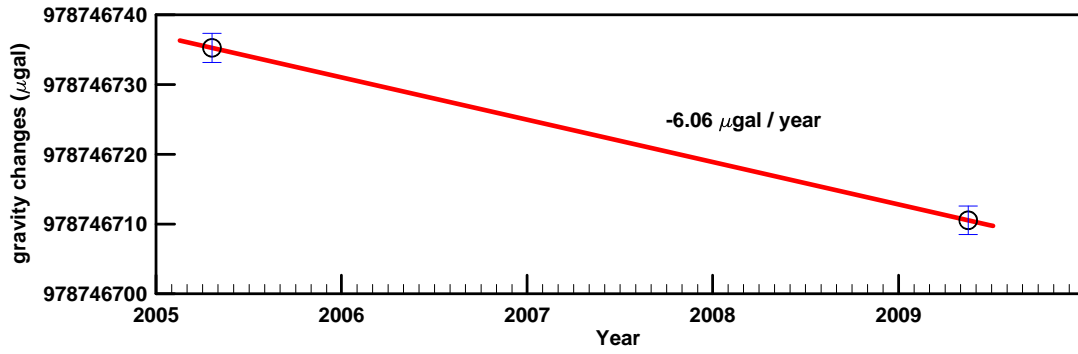


Fig. 7-20 Absolute gravity rate of YHEG station

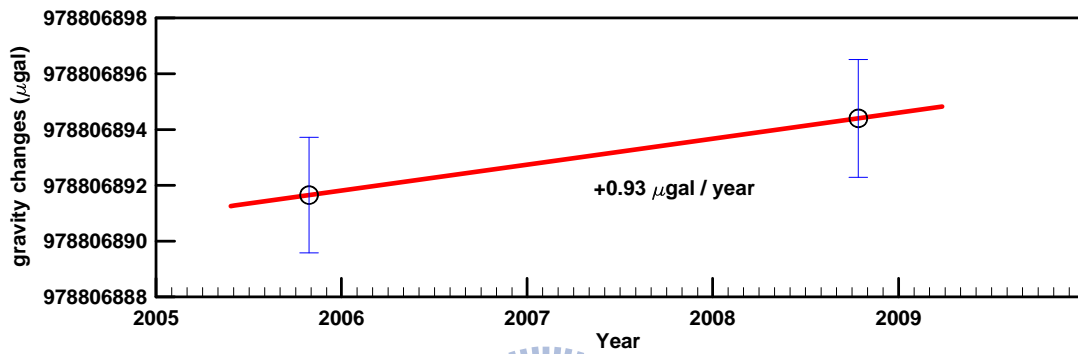


Fig. 7-21 Absolute gravity values and rate at YLIG

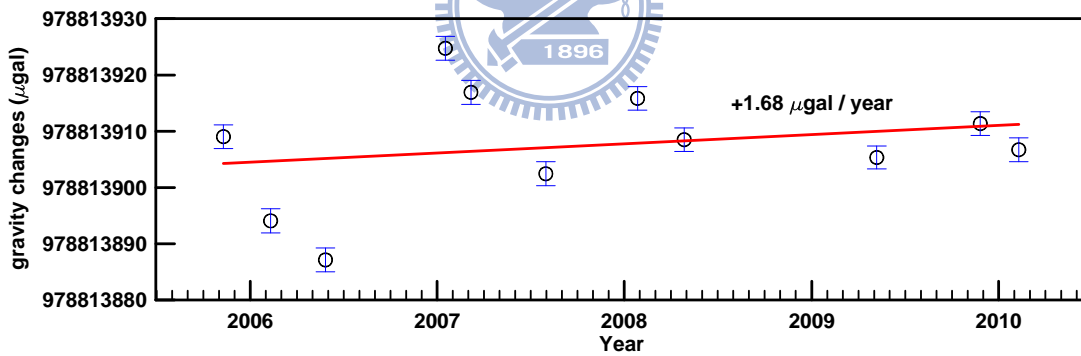


Fig. 7-22 Absolute gravity values and rate at YMSG

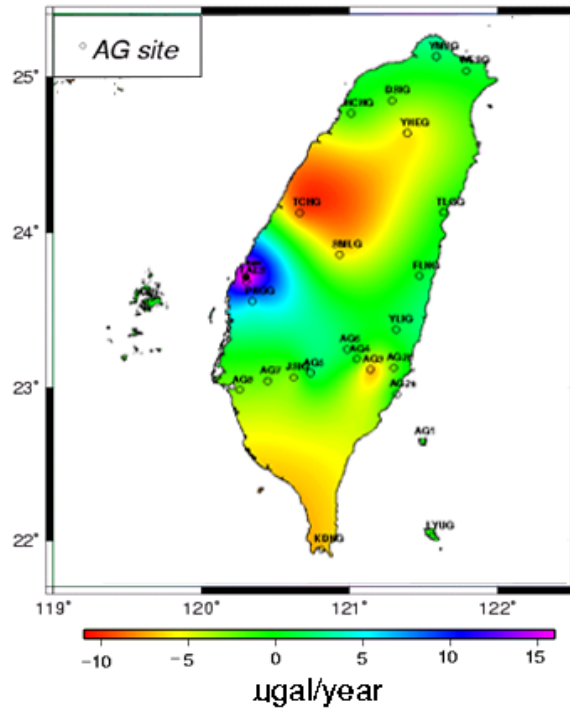


Fig. 7-23 Two-dimensional (lateral) distribution of gravity rates interpolated from the rates at AG sites

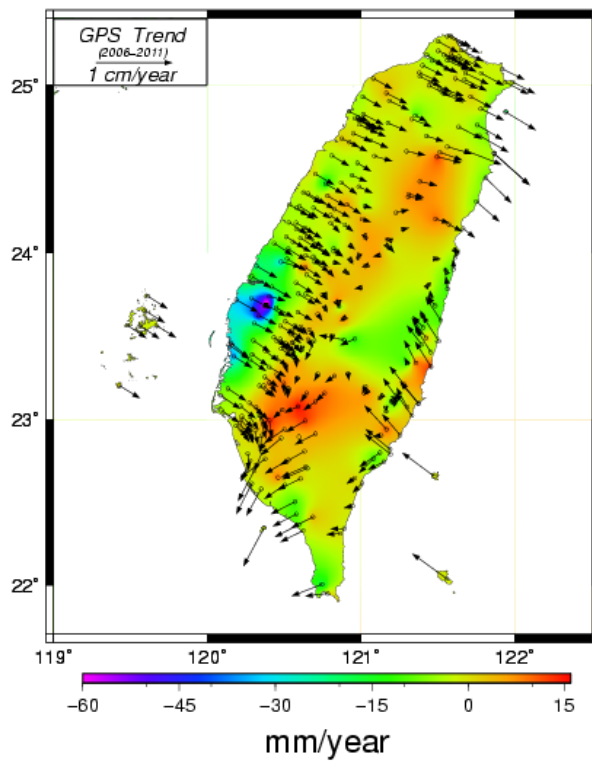


Fig.7-24 Horizontal displacement rates (arrows) and vertical displacement rates (color) from GPS. An arrow corresponds to a continuous GPS station.

Chapter 8 Gravity changes caused by typhoon and earthquake

8.1 Observed gravity effects due to typhoons

On average, three typhoons make landfalls on Taiwan in one year (Central Weather Bureau, Taiwan; <http://www.cwb.gov.tw>). A typhoon is an extremely low pressure system with abundant precipitating waters within the system. This anomalous atmospheric condition leads to an anomalous mass variation that is sensed by the SG in HS. The anomalous mass variations are best explained by the anomalous gravity-atmosphere admittances from the SG records. Table 8-1 lists such admittances associated with selected typhoons up to August 2010. For example, Typhoon Morakot made landfall on southern Taiwan on August 8 and created large rainfalls during 5-8 August, 2009 (Fig. 8-1). Its admittance of $-0.68 \mu\text{gal hPa}^{-1}$ differs substantially from the average value of $-0.35 \mu\text{gal hPa}^{-1}$ (Chapter 5). Another example is Kalmaegi (Fig. 8-2), which is also associated with a distinct admittance of $-0.65 \mu\text{gal hPa}^{-1}$. The eyes of these two typhoons passed through Hsinchu.

In fact, Typhoon Kalmaegi is less intensive than Typhoon Morakot, but the admittances associated with them are almost identical. An intuitive explanation is that Typhoon Kalmaegi (Fig. 8-1) traveled right through Hsinchu, while Typhoon Morakot (Fig. 8-2) made a landfall near southern Taiwan and created intensive rainfalls. Since the gravity effect of atmosphere on a station increases with decreasing distance, the two typhoons result in similar gravity effects in Hsinchu, despite the fact that Kalmaeg is less intensive.

Table 8-1: Gravity changes due to typhoons and gravity-atmosphere admittances at HS

Typhoon	Date	Lowest pressure in HS (hPa)	Category	Pressure change (hPa)	Gravity change (μgal)	Admittance ($\mu\text{gal hPa}^{-1}$)
Chanchu	May 16, 2006	991	2	11	5.5	-0.47
Bilis	July 12, 2006	969	1	28	8.6	-0.45
Kaemi	July 23, 2006	976	2	19	8.0	-0.43
Bopha	August 7, 2006	986	1	4	1.5	-0.48
Shanshan	September 14, 2006	993	2	7	3.0	-0.45
Wutip	August 8, 2007	984	1	5	2.2	-0.41
Sepat	August 16, 2007	973	3	23	8.5	-0.52
Krosa	October 4, 2007	967	3	35	12.5	-0.40
Kalmaegi	July 15, 2008	984	2	15	10.2	-0.65
Fung-Wong	July 26, 2008	970	2	34	13.1	-0.43
Nuri	August 19, 2008	993	2	9	4.4	-0.40
Sinlaku	September 11, 2008	981	3	21	7.9	-0.46
Jangmi	September 27, 2008	973	3	29	13.9	-0.51
Morakot	August 5, 2009	958	2	45	29.9	-0.68
Namtheun	August 29, 2010	989	-	11	8.5	-0.45
Fanapi	September 18, 2010	975	2	31	12.5	-0.47

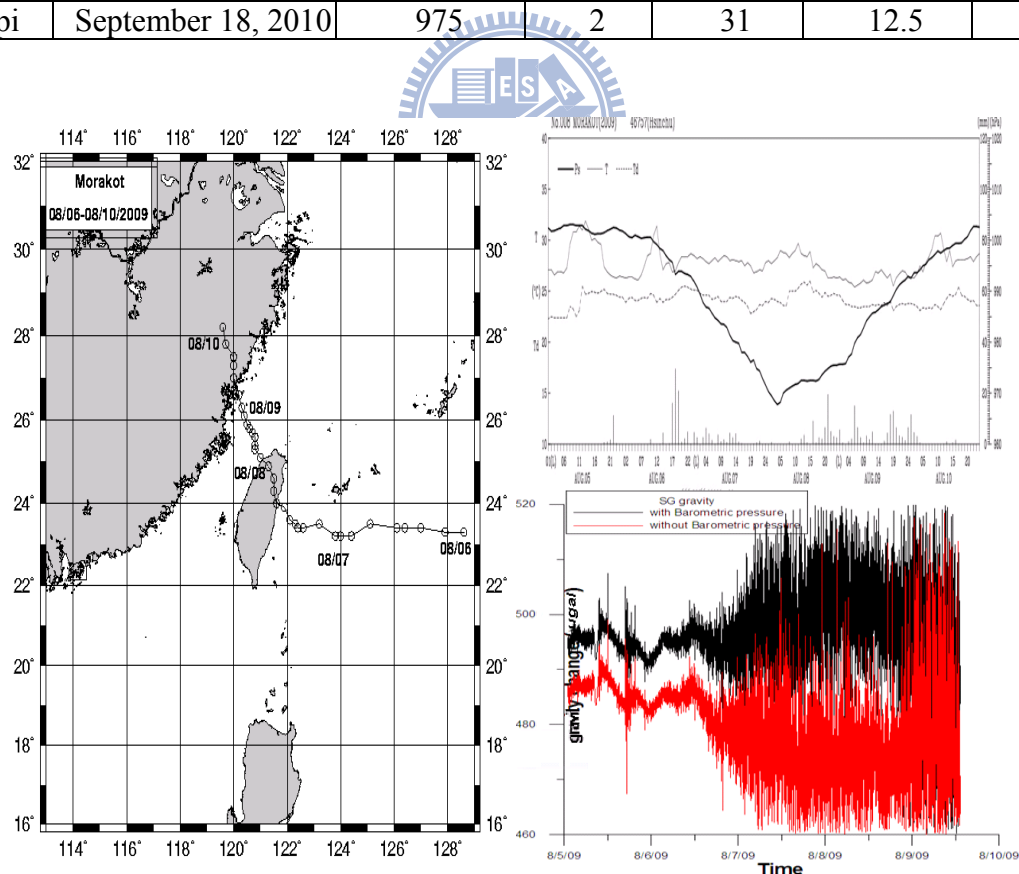


Fig. 8-1 Weather sensor outputs during Typhoon Morakot (top) and SG gravity data in Hsinchu with and without atmospheric pressure effects.

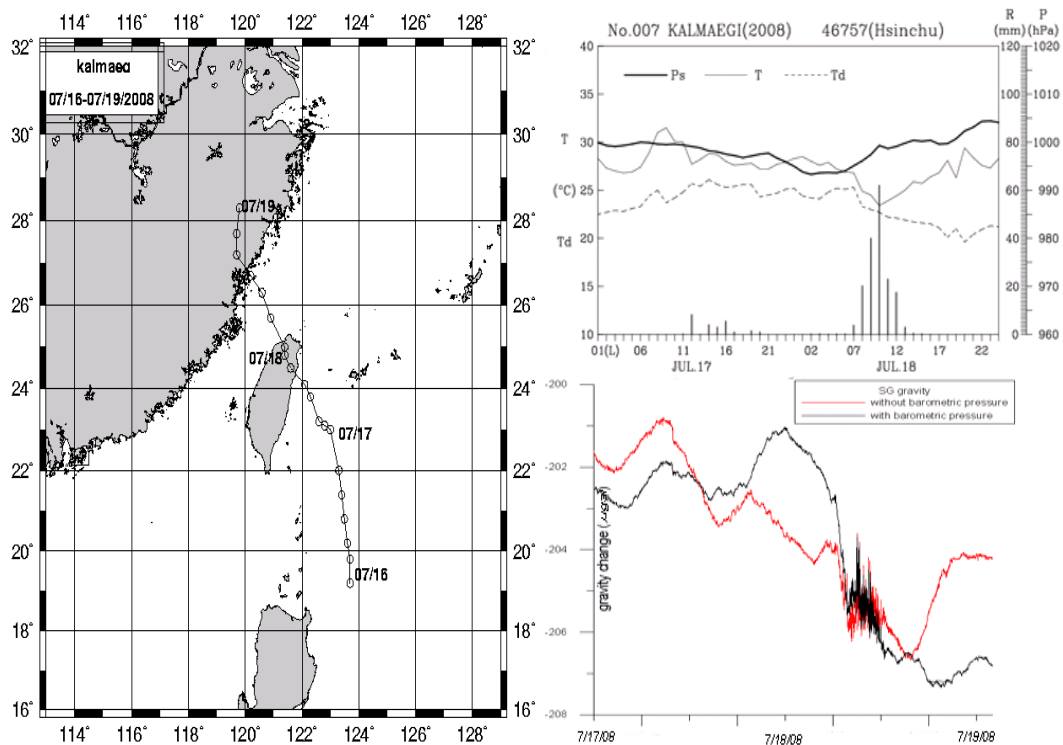


Fig. 8-2 Weather sensor outputs during Typhoon Kalmaegi (top) and SG gravity data in Hsinchu with and without atmospheric pressure effects.

8.2 Interpretations of typhoon-induced gravity changes

The observed gravity-atmosphere admittances in the previous section were explained by the atmospheric loading models below. As shown in previous studies (e.g., Spratt, 1982; Mukai et al., 1995; Boy et al., 1998 and Boy et al., 2002), the global atmosphere produces on two gravity effects, i.e., direct Newtonian effect and indirect elastic effect. About 90% of the atmospheric gravity effects are caused by atmospheric pressure variations within 50 km of a given station (Boy et al., 2002). We estimate the atmospheric effect in the spatial domain using the Green's function approach, and show different models of Newtonian attraction effects for the computation of atmosphere. Finally, the elastic influence is estimated.

8.2.1 Direct Newtonian effect

The atmospheric pressure gradient in the vertical direction is balanced with the gravity in the downward direction, leading to the hydrostatic equilibrium:

$$dP = -g\rho_a dz \quad (8-1)$$

Where g is gravity, ρ_a is density of atmosphere, and dP and dz are differential changes in pressure and altitude. If the atmospheric pressure is the perfect gas, the following equation gives the relation between pressure P , density ρ_a and temperature T as follow,

$$P = \rho_a RT \quad (8-2)$$



With Eq. (8-1) and Eq. (8-2), we can find out the relation of atmospheric pressure and dynamic height as follows

$$\frac{dP}{P} = -\left(\frac{g}{RT}\right)dz \quad (8-3)$$

$$g dz = -RT d(\ln P) \quad (8-4)$$

If we integrate from point a (z_a, P_a) to point b (z_b, P_b) as follows

$$\int_a^b g dz = -\int_a^b RT d(\ln P) \quad (8-5)$$

Assuming g is constant and using an average temperature, we get

$$\Delta z = z_b - z_a = \left(R \frac{\bar{T}}{g} \right) \ln \left(\frac{P_a}{P_b} \right) \quad (8-6)$$

where Δz is the thickness between the point a and b . \bar{T} is the average temperature between points a and b . Using $R = 287 \text{ (JKg}^{-1} \text{ K}^{-1})$ and $g = 9.8 \text{ (ms}^{-2})$, we obtain the dynamic height as:

$$\Delta z = K \bar{T} \ln \left(\frac{P_a}{P_b} \right) \quad (8-7)$$

$$K = \frac{R}{g} \quad (8-8)$$

where K is the ratio of thickness and the average temperature in different layer. Integrating Eq. (8-7) from the sea surface z_a ($z_a = 0$) to the point z_b leads to

$$z_b = K \bar{T} \ln \left(\frac{P_a}{P_b} \right) \quad (8-9)$$

where

$$P_a = P_b \exp \left(\frac{z_b}{K \bar{T}} \right) = P_b \exp \left(\frac{g z_b}{R \bar{T}} \right) \quad (8-10)$$

We can estimate the density variation with dynamic height by the model of atmospheric effect with pressure and temperature at the global surface, which 10 km are the upper limit used in the study.

The pseudo-stratified Newtonian Green's function $GN(\psi)$ is

$$GN(\psi) = \int \left[GS(\psi, z) \frac{1}{RT} \exp\left(-\frac{gz_g}{RT}\right) \right] dz \quad (8-11)$$

where $GS(\psi, z)$ is the Green's function of the Newtonian effect in a stratified atmospheric model. The direct Newtonian gravity effect at (θ, λ) is the convolution of the Green's function and pressure variation of the atmospheric thickness as

$$\delta g_N(\theta, \lambda) = \iint GN(\psi) p_0(\theta', \lambda') ds' \quad (8-12)$$

where $\delta g_N(\theta, \lambda)$ is the Newtonian effect, $p_0(\theta', \lambda')$ is the pressure variation of the atmospheric thickness, $ds' = a^2 \sin \theta' d\theta' d\lambda'$ is the surface element of integration (a is the mean radius of the earth).



8.2.2 Indirect elastic effect

This section presents the indirect (loading) gravity effect based on the Love numbers of vertical atmospheric structure. The elastic effect of atmosphere is used to calculate the Earth's response to the surface pressure changes (Boy et al., 2002). We compute this contribution in the Green's function formalism (Farrell, 1972). In a hybrid model, the thin layer of the atmosphere at the Earth surface is based on a stratified loading process. We use the load Love numbers h_n and k_n from the Preliminary Reference Earth Model (Dziewonski & Anderson 1981).

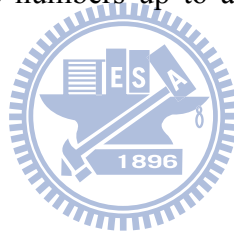
The elastic Green's function can be expressed as (e.g. Farrell 1972; Boy et al., 1998)

$$GE(\psi) = -\frac{G}{ga^2} \sum_{n=0}^{+\infty} [2h_n - (n+1)k_n] P_n(\cos \psi) \quad (8-13)$$

where G and g are the universal constant of gravitation and the mean surface gravity, respectively, a mean radius of the earth, $P_n(\cos \psi)$ is the Legendre polynomial of degree n . The elastic effect at (θ, λ) is

$$\delta g_E(\theta, \lambda) = \iint GE(\psi) p_0(\theta', \lambda') ds' \quad (8-14)$$

where $g_E(\theta, \lambda)$ is the elastic effect, $p_0(\theta, \lambda)$ is the pressure variation of the atmospheric thickness. In this study, the numerical estimates of Green's functions require the computation of Love numbers up to a high spherical harmonic degree ($n=9000$).



8.2.3 Global atmospheric effect

The global atmosphere data used in this study are from ECMWF on a $1.5^\circ \times 1.5^\circ$ grid at a 6-h interval. However, such coarse resolutions in space and time will not be able to show the rapid gravity changes during a typhoon event. This resolution program is illustrated at Appendix 2. Fig. 8-3 shows the track of Typhoon Morakot around Taiwan during August 5-8, 2009. Fig 8-4 shows the track of Typhoon Kalmaegi during July 15-19, 2008. Gravity change images based on the formulae presented above have been made at a 6-h interval (not shown in this dissertation). With these images, it is easy to understand and visualize gravity changes due to a typhoon. Fig 8-5 shows the gravity changes from different atmospheric contributions. The blue line is the global atmospheric effect, the purple line is the local atmospheric effect and the brown line is total amount of these two effects. Compared to residual gravity (black), the largest

atmospheric effect occurred on July 18, 2008. This gravity low is due to the atmospheric pressure that concurred with the time when the eye of the Typhoon Kalmaegi passed through Hsinchu. Before the arrival of Typhoon Kalmagei in Hsinchu, the local atmospheric effect based on an admittance of $-0.35 \mu\text{gal hPa}^{-1}$ (red) matches well with the residual gravity. As Typhoon Kalmagei passed through Hsinchu, using an admittance of $-0.65 \mu\text{gal hPa}^{-1}$ leads to a best agreement between the residual gravity and the atmospheric gravity effect. In conclusion, global atmospheric grids from ECMWF and the atmospheric loading above can partly explain the gravity changes during a typhoon, and a SG-derived admittance based on the gravity-atmosphere admittance can best explain the gravity variation during a typhoon.

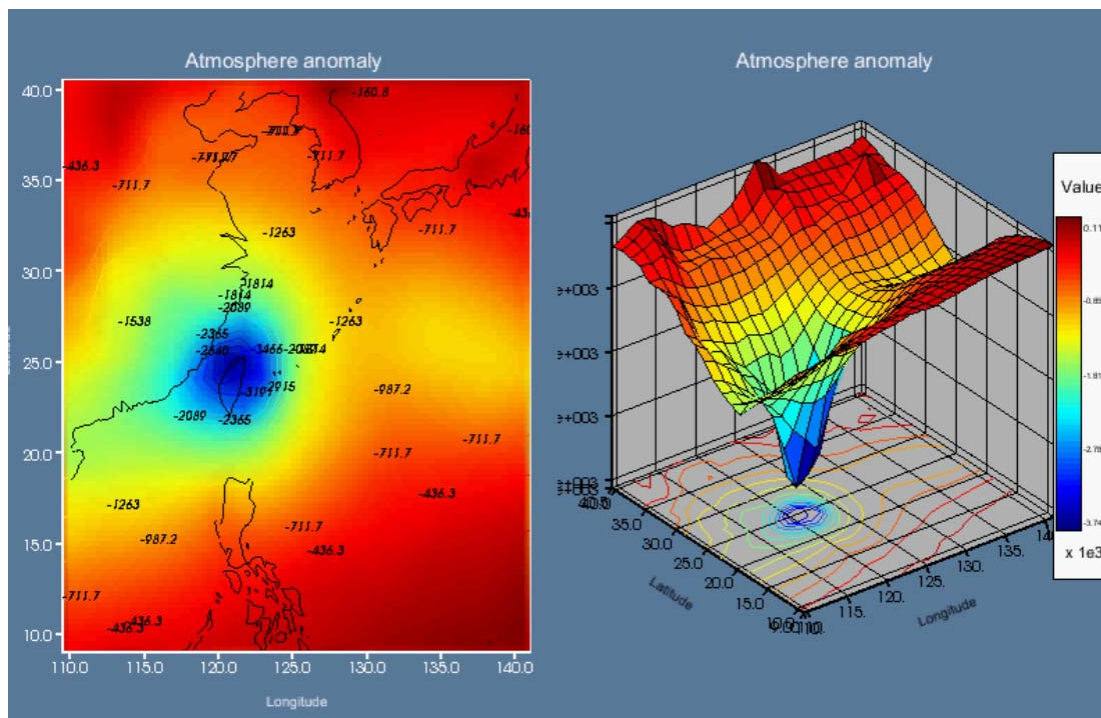


Fig. 8-3 A plane view (left) and perspective view of the 3-D atmospheric pressure model for Morakot

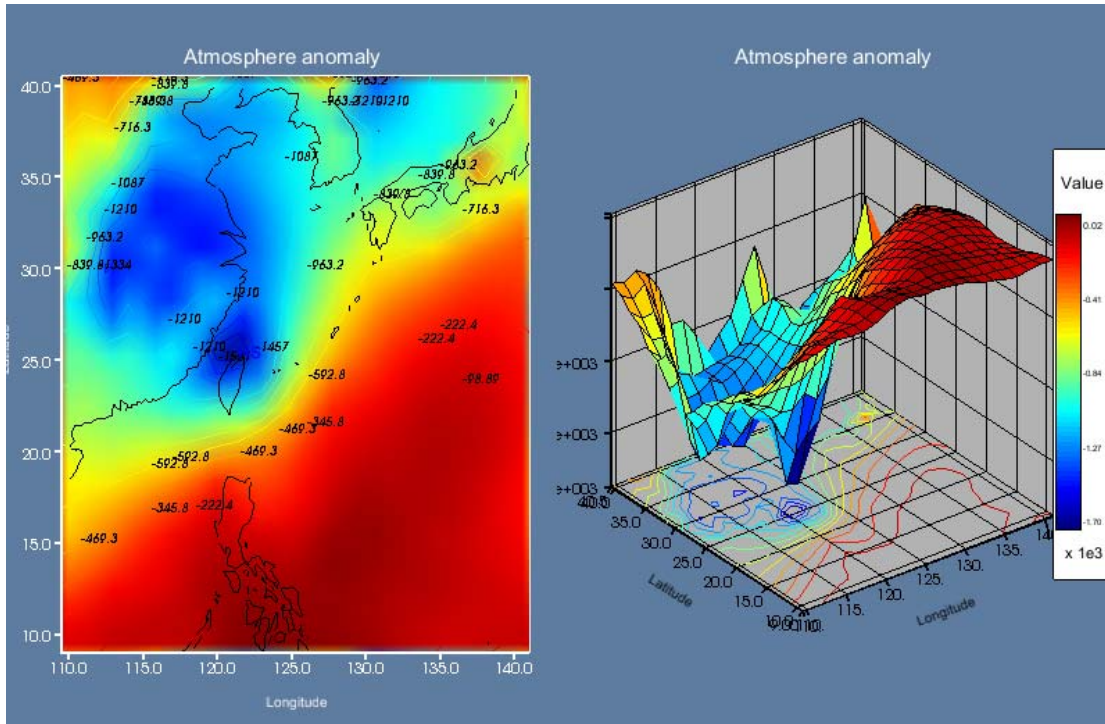


Fig. 8-4 A plane view (left) and perspective view of the 3-D atmospheric pressure

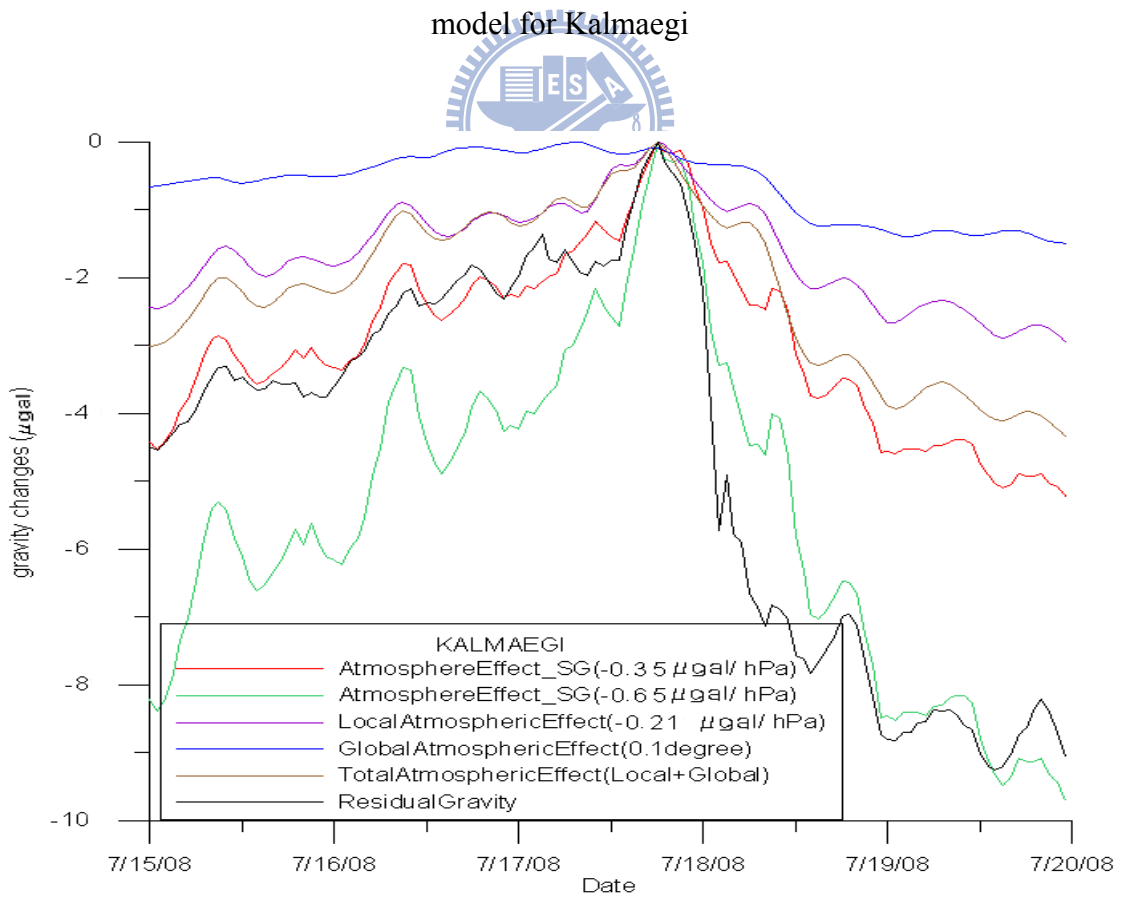


Fig. 8-5 Atmospheric gravity effects of Typhoon Kalmaegi from different contributions

8.3 Observed co-seismic gravity changes due to earthquake

The co-seismic gravity change at Hsinchu due to a nearby earthquake will help to validate the fault parameters associated with the earthquake (Imanishi et al., 2004). HS is close to an active earthquake zone belonging to the ring of fire in the western Pacific. Near real-time records of earthquakes around Taiwan is found at <http://www.cwb.gov.tw/V5/seismic/quake.htm/>.

An earthquake will introduce oscillations in the gravity records. Depending on the magnitude, depth and distance to HS, the oscillation may last from few minutes to few hours. Such oscillations are considered as anomalous records and are often excluded from such analyses as solid earth tide and ocean tide gravity effects. Hidden in the oscillations is a permanent gravity change that is caused by mass change and surface dislocation. The detection of such a permanent gravity change will require the modeling of a step function before and after the earthquake (Imanishi et al., 2004). Following the method used by Imanishi et al. (2004), we used the T48 records to determine permanent gravity changes due to earthquakes around Taiwan in 2006 and 2007, which are listed in Table 8-2.

As an example, Fig. 8-7 shows the permanent gravity change at HS due to earthquake on September 6, 2007. The magnitude of this earthquake is 6.6 and the depth is 54 km. Situated at the Pacific Ocean northeast of Taiwan, the earthquake's epicenter is at latitude=24.28°, longitude=122.25° and 155 km away from HS. The gravity change due to the co- and post-seismic deformations was theoretically studied (e.g., Wang et al., 2006; Fu and Sun, 2008). Although we must carefully check the instrumental instability as a possible source to make the gravity offset shown in Table 8-2 by comparing the observed offsets to the amplitudes and the directions which are expected from the theoretical estimations and the GPS observations carried out at HS and nearby sites to it. However, Table 8-2 can be used to validate the theoretical models

that estimate co- and post-seismic gravity changes, and therefore help to refine the fault parameters associated with an earthquake. Furthermore, it is noted that cumulative gravity offsets due to earthquakes will be a possible significant source of the secular gravity rate changes at HS. The latest major earthquake recorded by HS SG was the March 11, 2011 Japan earthquake (Fig. 8-8), which was preceded by a series of large foreshocks two days before this earthquake. On March 9, 2011, a Mw 7.2 earthquake occurred approximately 40 km from the epicenter of the March 11 earthquake, followed by three earthquakes greater than Mw 6 on the same day.

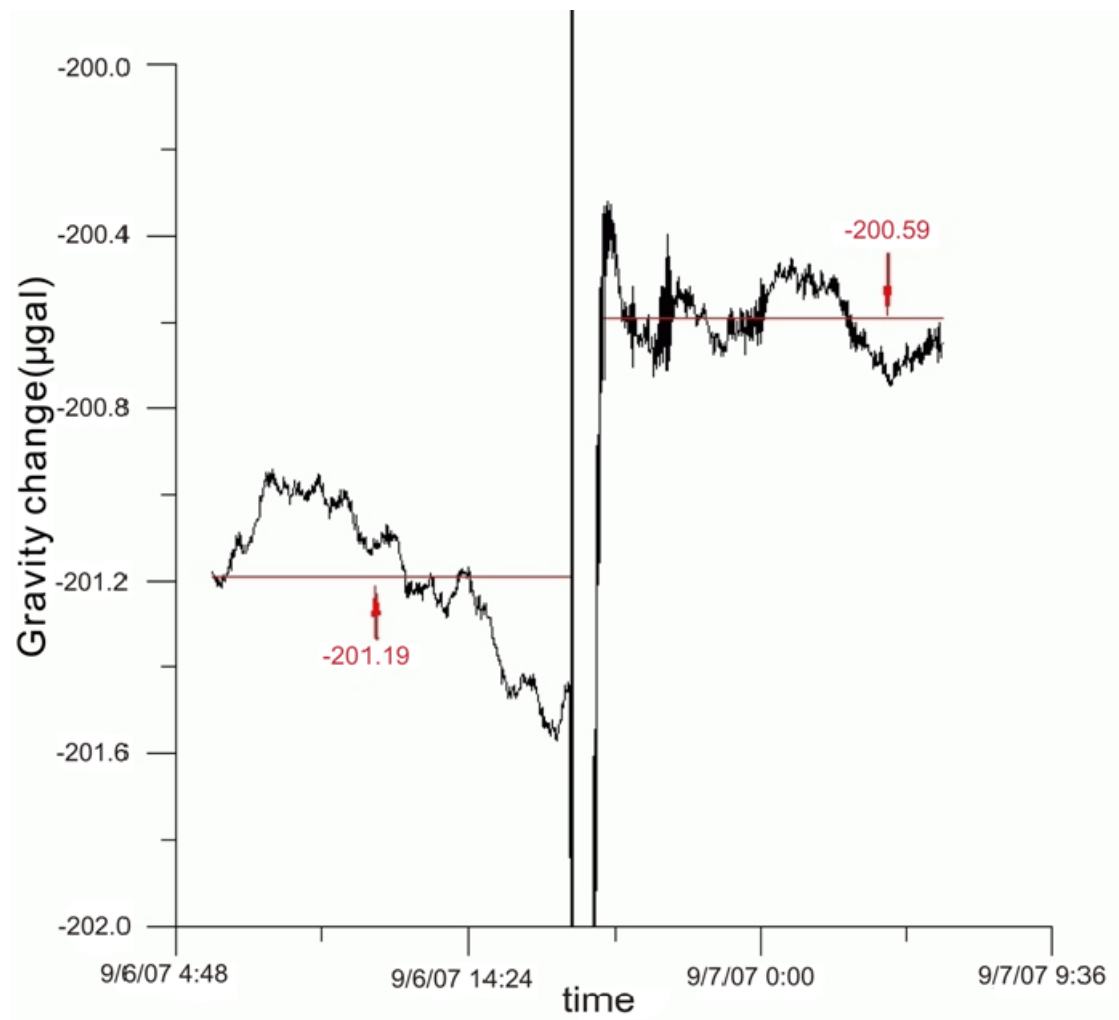


Fig. 8-6 Co-seismic gravity change, given as a jump (step function) in the SG gravity records at HS, due to the earthquake on September 6.

Table 8-2: Gravity shifts due to earthquakes around Taiwan at HS (2006-2009)

Date	Distance (km)	Depth (km)	Magnitude of earthquake	Gravity shift (μgal)
April 1, 2006	214	9	6.2	1.19
April 15, 2006	223	17	6.0	-0.17
April 28, 2006	109	8	5.2	-0.61
July 28, 2006	170	49	6.0	1.01
August 27, 2006	197	145	6.0	0.00
October 12, 2006	181	44	5.8	-0.13
December 14, 2006	120	7	4.8	-1.10
December 23, 2006	138	10	5.4	0.48
December 26, 2006	296	44	7.0	-0.41
January 16, 2007	191	21	5.4	0.10
January 25, 2007	226	26	6.2	-0.31
May 12, 2007	101	44	4.9	-0.41
July 23, 2007	155	31	6.0	-0.41
August 9, 2007	201	4	5.9	-1.41
September 6, 2007	155	54	6.6	0.60
October 11, 2007	92	80	5.2	0.27
October 17, 2007	176	42	5.7	0.01
November 28, 2007	91	69	5.4	-0.94
March 5, 2008	161	11.3	5.2	-0.07
April 14, 2008	191	27.2	5.1	-0.05
April 23, 2008	202	11.1	5.6	-0.05
June 1, 2008	312	41.9	6.4	0.1
November 8, 2008	171	35.1	5.9	-0.12
January 4, 2009	102	7.5	5.1	-0.9
August 17, 2009	362	43.3	6.8	0.08
September 12, 2009	218	25.1	5.1	0.3
November 5, 2009	125	24.1	6.2	-0.2
December 19, 2009	130	43.8	6.9	10.91
February 7, 2010	327	88	6.6	0.42
March 4, 2010	205	22.6	6.4	5.80
April 26, 2010	407	73.4	6.8	6.17
October 4, 201	272	35	6.6	-1.96
November 21, 2010	128	46.9	6.1	-0.65

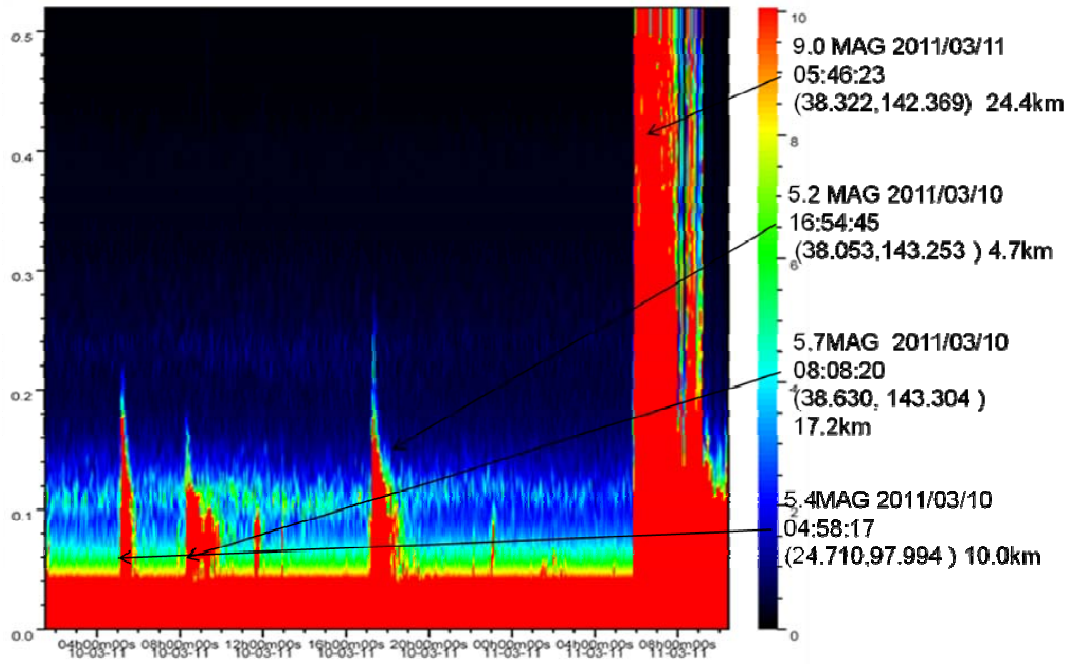


Fig. 8-7 Magnitude 9.0 – near the east coast of Honshu, Japan earthquake on March



Chapter 9 Summary and future work

This study summarizes the findings from the observations of two SG (serial no. 48 and 49) three FG5 (serial no. 224, 228, and 231) and a regional GPS network around Taiwan. The main objectives of this study are:

1. The introductions of SG and AG in Taiwan, including individual devices and the procedures of operation.
2. The analyses of the SG's critical parameters and the potential applications to related studies, such as solid earth tide, ocean tide loading, atmospheric effect, hydrologic effect, typhoon and earthquake.
3. The preliminary results from the AGTO project in connection to the result of GPS.

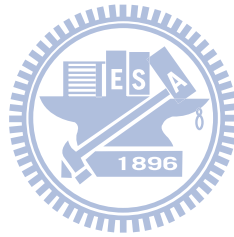
The major findings of this study are listed below:

1. Establishing procedures to determine many different types of detided gravity enabling to analyze solid earth tide, ocean tide loading, atmospheric effect, hydrological effect, polar motion effect and other gravity changes caused by environmental changes.
2. The drifting rate of AG and T48 are $2.2 \pm 0.3 \mu\text{gal year}^{-1}$ and $1.3 \pm 0.1 \mu\text{gal year}^{-1}$ from the AG and T48 measurements from 2006 to 2011. Based on the parallel observations of AG and SG, the CF and the different rate between AG and T48 were $-76.087 \pm 0.067 \mu\text{gal voltage}^{-1}$ and $-0.8 \pm 1.3 \mu\text{gal year}^{-1}$, respectively. The observed drifting rate of T48 is smaller than the nominal drift-rate of $6 \mu\text{gal year}^{-1}$ reported by the SG manufacturer.
3. The north area of HS is a groundwater-rich alluvium with evident gravity variations. A vertical site motion of $-0.22 \pm 0.97 \text{ cm year}^{-1}$ at HS was found and not directly related to the movement of the Hsinchu Fault.

4. The gravity-atmosphere admittances during typhoons are 30% larger than the mean value. In modeling gravity change due to atmosphere, the global atmospheric pressure model is suitable over a large area, especially for the long period variation. Short period atmosphere-induced gravity change is only well predicted by high frequent atmospheric data.
5. The relative errors between the gravimetric amplitude factors determined with T48 (corrected by NAO.99b) and the model factors of Dehant et al. (1999) range from 99.95 to 96.07%. The Newtonian part contributes a significant portion to ocean tide loading gravity effects (about 20% for M_2 at HS) at HS. The largest Newtonian gravity effect of ocean tide is found around Matzu.
6. The gravity offset generated by the earthquake of September 6, 2007 reached 0.6 μgal , which contributes 0.3 $\mu\text{gal year}^{-1}$ to the gravity rate at HS over 2006-2011.
7. The mean gravity and vertical rates at AGTO sites are $-1.39 \pm 4.21 \mu\text{gal year}^{-1}$ and $0.50 \pm 0.94 \text{ cm year}^{-1}$. The sediment thicknesses changes near AG6 and AG3 due to landslides caused by Typhoon Morakot are 2.45 m and 1.25 m.
8. Using repeated absolute gravimetric measurements to determine gravity changes at islandwide (Taiwan) stations, and the preliminary causes of such changes are identified with the help of GPS and other data. The average rate of gravity change from 2005 to 2008 is $-0.58 \mu\text{gal year}^{-1}$ in Taiwan.

In this study, the SG and AG gravimeter measurements have been applied to tidal analysis, geodynamics, typhoon and atmosphere. Potential applications of these instruments of methodologies are listed below.

1. The SG gravimeter, T49, is currently at Hsinchu, but it can be deployed in a new location (other than Hsinchu) that has a different geodynamic feature. With two SG at two locations, many research opportunities can be explored. For example, a proposed new site for T49 is Mt. Yangming (see Fig. 6-4, YMSG), where possible volcano eruptions can occur and hydrological changes will induce large mass and gravity changes. Records from two SG can be used to study gravity changes in sea level ocean circulation associated with the Kuroshio Current.
2. Use of gravimetry to study groundwater in central Taiwan. Since 90 % of all unfrozen fresh water is hidden underground, it is difficult to determine its volume. The volume can be estimated with a network of AG sites around central Taiwan.



References

- Boy, J.P., J. Hinderer, and P. Gegout, 1998. Global atmospheric loading and gravity, *Phys. Earth planet. Inter.*, 109, 161–177.
- Boy, J.P., P. Gegout, and J. Hinderer, 2002. Reduction of surface gravity data from global atmospheric pressure loading. *Geophys. J. Int.* 149, 534–545.
- Boy, J. P., M. Llubes, R. Ray, J. Hinderer, N. Florsch, S. Rosat, F. Lyard, and T. Letellier, 2004. Non-linear oceanic tides observed by superconducting gravimeters in Europe, *J. Geodyn.*, 38, 391-405.
- Boy, J. P., and J. Hinderer, 2006. Study of the seasonal gravity signal in superconducting gravimeter data, *J. Geodyn.*, 41, 227-233.
- Chojnicki, T., 1973. Ein Verfahren zur Erdzeitenanalyse in Anlehnung an das Prinzip der kleinsten Quadrate. *Mitt. Inst. F. Theor. Geod. Univ. Bonn*, Nr. 15.
- Crossley, D., O. Jensen, and J. Hinderer, 1995. Effective barometric admittance and gravity residuals. *Phys. Earth planet. Int.*, 90, 355-358
- Dal Moro, G. and M. Zadro, 1998. Subsurface deformations induced by rainfall and atmospheric pressure: tilt/strain measurements in the NE-Italy seismic area. *Earth and Planetary Science Letters*, 164, pp. 193-203
- Dehant, V., P. Defraigne, and J. M. Wahr, 1999. Tides for a convective Earth. *J. Geophys. Res.*, 104, 1035-1058.
- Dziewonski, A. D., and D. L. Anderson, 1981. Preliminary reference Earth model, *Phys. Earth Planet. Inter.*, 25, 297-356.
- Eanes, R., and S. Bettadpur, 1996. The CSR3.0 global ocean tide model: Diurnal and Semi-diurnal ocean tides from TOPEX/POSEIDON altimetry, CRS-TM-96-05, University of Texas, Centre for Space Research, Austin, Texas.
- Falk, R., M. Harnisch, G. Harnisch, I. Novak, and B. Richter, 2001. Calibration of the

- Superconducting Gravimeter SG 103, C023, CD029 and CD030. *Journal of Geodetic Society of Japan*, 47, 22–27.
- Farrell, W. E., 1972. Deformation of the earth by surface loads, *Rev. Geophys. Space Phys.*, 10, 761-797.
- FG5 Absolute Gravimeter User's Manual, December 2006. <http://www.microglacoste.com/>
- Francis, O., T. M. Niebauer, G. Sasagawa, F. Klopping, and J. Gschwind, 1998. Calibration of a superconducting gravimeter by comparison with an absolute gravimeter FG5 in Boulder, *Geophys. Res. Lett.*, 25, 1075-1078.
- Fu, G. Y., and W. K. Sun, 2008. Surface coseismic gravity changes caused by dislocations in a 3-D heterogeneous earth, *Geophys. J. Int.*, 172, 479-503, doi: 10.1111/j.1365-246X.2007.03684.x
- GWR instruments, inc. 2011. GWR Observatory Superconducting Gravimeter and Support Systems. <http://www.gwrinstruments.com/index.html>
- Hwang, C., R. Kao, C. C. Cheng, J. F. Huang, C. W. Lee, and T. Sato, 2009. Results from parallel observations of superconducting and absolute gravimeters and GPS at the Hsinchu station of Global Geodynamics Project, Taiwan. *J. Geophys. Res.*, 114, B07406, doi: 10.1029/2008JB006195.
- Imanishi, Y., T. Higashi, and Y. Fukuda, 2002. Calibration of the superconducting gravimeter T011 by parallel observation with the absolute gravimeter FG5 #210 - a Bayesian approach, *Geophys. J. Int.*, 151, 867-878.
- Imanishi, Y., T. Sato, T. Higashi, W. K. Sun, and S. Okubo, 2004. A network of superconducting gravimeters detects submicrogal coseismic gravity changes, *Science*, 306, 476 – 478, doi: 10.1126/science.1101875.
- Jacob, T., R. Bayer, J. Chery, H. Jourde, N. Le Moigne, J. P. Boy, J. Hinderer, B. Luck, and P. Brunet, 2008. Absolute gravimetry monitoring of water storage variation in

- a karst aquifer on the larzac plateau (Southern France), *J. Hydrol.*, 359, 105-117.
- Jan, S., C. S. Chern, J. Wang, and S. Y. Chao, 2004. The anomalous amplification of M2 tide in the Taiwan Strait, *Geophys. Res. Lett.*, 31, L07308, doi:10.1029/2003/GL019373.
- Kim, J. W., J. Neumeier, T. H. Kim, I. Woo, H. J. Park, J. S. Jeon, and K. D. Kim, 2009. Analysis of superconducting gravimeter measurements at MunGyung station, Korea. *J. Geodyn.*, 47, 180-190, doi: 10.1016/j.jog.2008.07.008.
- Kim, S. Y., and H. Y. Chun, 2011. Impact of typhoon-generated gravity waves in the typhoon development, *Geophys. Res. Lett.*, 38, L01806, doi: 10.1029/2010GL045719.
- Lyard, F., F. Lefevre, T. Letellier, and O. Francis, 2006. Modeling the global ocean tides: modern insights from FES2004, *Ocean Dynamics*, 56, 394-415.
- Matsumoto, K., T. Takanezawa, and M. Ooe, 2000. Ocean tide models developed by assimilating TOPEX/POSIDON altimeter data into hydrodynamical model: A global model and a regional model around Japan, *J. Oceanogr.*, 56, 567-581.
- Mouyen, M., F. Masson, C. Hwang, C.-C. Cheng, R. Cattin, C.W. Lee, N. Le Mogine, J. Hinderer, J. Malavieille, R. Bayer and B. Luck, 2009. Expected temporal absolute gravity change across the Taiwanese Orogen, a modeling approach, *J. Geodynamics*, 48, 284-291.
- Mukai, A., T. Higashi, S. Takemoto, I. Nakagawa and I. Naito, 1995. Accurate estimation of atmospheric effects on gravity observations made with a superconducting gravity meter at Kyoto, Volume 91, Issues 1-3, pp. 149-159.
- Naujoks, M., A. Weise, C. Kroner, and T. Jahr, 2008. Detection of small hydrological variations in gravity by repeated observations with relative gravimeters, *J. Geod.*, 82, 543-553.
- Nawa, K., N. Suda, I. Yamada, R. Miyajima, and S. Okubo, 2009. Coseismic change

- and precipitation effect in temporal gravity variation at Inuyama, Japan: A case of the 2004 off the Kii peninsula earthquakes observed with a superconducting gravimeter. *J. Geodyn.*, 48, 1-5, doi: 10.1016/j.jog.2009.01.006.
- Nerem, R. S., E. Leuliette, and A. Cazenave, 2006. Present-day sea-level change: A review, *Comptes Rendus Geoscience*, 338, 14-15.
- Neumeyer, J., J. Hagedoorn, J. Leitloff, and T. Schmidt, 2004. Gravity reduction with three-dimensional atmospheric pressure data for precise ground gravity measurements, *J. Geodyn.*, 38, 437-450.
- Neumeyer, J., F. Barthelmes, C. Kroner, S. Petrovic, R. Schmidt, H. Virtanen, and H. Wilmes, 2008. Analysis of gravity field variations derived from superconducting gravimeter recordings, the GRACE satellite and hydrological models at selected European sites, *Earth Planets Space*, 60, 505-518.
- Peterson, J., 1993. Observations and modelling of background seismic noise. Open-file report 93-322, U. S. Geological Survey, Albuquerque, New Mexico.
- Penna, T. N., M. A. King, and M. P. Stewart, 2007. GPS height time series: Short-period origins of spurious long-period signals, *J. Geophys. Res.*, 11, B02402, doi: 10.1029/2005JB004047.
- Richter, B., H. Wilmes, and I. Nowak, 1995. The Frankfurt Calibration System for Relative Gravimeters. *Metrologia*, 32, 217–224
- Sato, T., Y. Tamura, S. Okubo, and S. Yoshida, 1996. Calibration of scale factor of superconducting gravimeter at Esashi using an absolute gravimeter FG5. *Journal of Geodetic Society of Japan*, 42, 225–232.
- Segall, P., and J. L. Davis, 1997. GPS applications for geodynamics and earthquake studies. *Annu. Rev. Earth Planet. Sci.* 25, 301–336.
- Shiomi, S., 2006. Geophysical test of the universality of free-fall, *Phys. Rev. D: Part. Fields*, 74, 027101.

- Spratt, R. S., 1982. Modelling the effect of atmospheric pressure variations on gravity, *Geophys. J. R. astr. Soc.*, 71, 173–186.
- Tamura, Y., T. Sato, M. Ooe, and M. Ishiguro, 1991. A procedure for tidal analysis with a Bayesian information criterion, *Geophys. J. Int.*, 104, 507-516.
- Tamura, Y., T. Sato, Y. Fukuda, and T. Higashi, 2005. Scale factor calibration of a superconducting gravimeter at Esashi Station, Japan, using absolute gravity measurements, *J. Geod.*, 78, 481-488.
- Torge, W., 1989. *Gravimetry*. De Gruyter, Berlin.
- TSoft Manual, 2010. <http://seismologie.oma.be/TSOFT/tsoft.html>
- Van Ruymbecke, M., 1989. A calibration system for gravimeters using a sinusoidal acceleration resulting from a vertical periodic movement. *Journal of Geodesy*, 63, 223–236.
- Virtanen, H., and J. Makinen, 2003. The effect of the Baltic sea level on gravity at the Metsahovi station, *J. Geodyn.*, 35, 553-565.
- Wang, R. J., F. Lorenzo-Martín, and F. Roth, 2006. PSGRN/PSCMP- a new code for calculating co- and post-seismic deformation, geoid and gravity changes based on the viscoelastic-gravitational dislocation theory, *Comput. Geosci.*, 32, 527-541.
- Warburton, R. J., and E. W. Brinton, 1995. Recent developments in GWR Instrument's superconducting gravimeters, *Proc. 2nd Workshop in Non-tidal Gravity Changes: Intercomparison Between Absolute and Superconducting Gravimeters*. Cahiers du Centre Européen de Géodynamique et de Séismologie, Luxembourg, ed. Poitevin, C., 11, 23-56.
- Warburton, R. J., and Goodkind, J. M., 1977. The influence of barometric pressure variations on gravity. *Geophys. J. R. astr. Soc.*, 48, 281-292.
- Wenzel, H. G., 1996. The nanogal software: Earth tide processing package ETERNA 3.30. *Bull. d'Inf Marées Terr.*, 124, 9425-9439.

Appendix 1

Table a: The information of GPS stations

Station(Institution ^a)	Lat.(deg.)	Lon.(deg.)	Height (m)
8118(IES)	23.46298	120.55298	228
AKND(CWB)	22.80331	120.35726	64
ALIS(CWB)	23.50817	120.81329	2438
ANKN(CWB)	24.95910	121.52472	45
BALN(CWB)	24.69948	121.42612	1715
BANC(CWB)	24.99765	121.44210	30
BANP(CWB)	22.69313	120.30540	122
BDES(WRA)	23.38057	120.17189	25
BEGN(NLS)	26.21562	119.97457	30
BLOW(CWB)	24.17175	121.57124	375
C001(IES)	23.41794	120.61239	680
C002(IES)	23.36174	120.57719	873
CAOT(NLS)	23.97938	120.68873	141
CHEN(CWB)	23.09740	121.37358	60
CHGO(NLS)	23.09833	121.37453	77
CHIA(CWB)	23.49597	120.43320	49
CHIH(CWB)	23.11584	121.20598	313
CHIN(CWB)	24.27101	120.58215	57
CHIU(CWB)	23.94538	120.82890	1067
CHKU(IES)	23.05584	120.09275	22
CHNT(CWB)	24.14921	121.66189	38
CHSG(WRA)	23.86034	120.28914	25
CHUA(CWB)	24.06605	120.55730	109
CHUL(CWB)	23.13236	121.12568	465
CHUN(CWB)	23.45285	121.39310	118
CHYI(MOI)	23.45076	120.14015	22
CHYN(IES)	23.39327	120.29080	40
CIME(NLS)	23.20463	119.42997	54
CISH(NLS)	22.88959	120.48123	90
CK01(CKU)	22.97589	120.21046	43
CKSV(NLS)	22.99885	120.22000	59
CLAN(CWB)	24.60225	121.51200	453
CLON(CWB)	22.43005	120.57960	49

CTOU(CWB)	22.75468	120.27784	25
CWEN(IES)	23.47304	120.45276	78
DAHU(CWB)	24.42288	120.87183	307
DAJN(CWB)	22.31130	120.86497	356
DASI(CWB)	22.47842	120.94441	386
DAWU(NLS)	22.34059	120.89004	41
DCHU(CWB)	23.21318	121.28057	251
DNAN(CWB)	23.67380	120.44799	48
DNFU(CWB)	23.68512	121.48228	133
DONA(IES)	22.91562	120.70351	522
DONY(NLS)	26.36769	120.48970	101
DOSH(NLS)	24.26268	120.82688	396
DPIN(CWB)	24.04308	120.93280	740
DSIN(CWB)	23.63121	121.39803	178
DULI(CWB)	23.02566	121.33059	49
ERLN(CWB)	23.79759	120.41955	44
ERPNI(IES)	22.94217	121.16611	221
FALI(NLS)	22.36525	120.59360	41
FENP(CWB)	23.59845	121.51942	39
FIVE(CWB)	25.07105	121.78107	775
FKDO(CWB)	23.68355	120.85627	560
FLNM(MOI)	23.74630	121.45335	138
FLON(CWB)	25.02037	121.93748	41
FNGU(IES)	24.03516	120.72445	170
FUGN(MOI)	22.79075	121.19216	31
FUNY(CWB)	23.92231	120.32017	24
FUQE(IES)	24.01115	120.82331	291
FUSI(NLS)	24.82120	121.35285	502
FUSN(CWB)	24.79904	121.33146	362
GAIS(CWB)	23.08029	120.59062	313
GFES(WRA)	23.74141	120.40248	45
GOLI(NLS)	25.02039	121.98742	45
GS01(CGS)	24.98199	121.50816	53
GS02(CGS)	24.80972	120.98233	53
GS03(CGS)	24.77660	121.04406	146
GS04(CGS)	23.59152	120.50679	91
GS05(CGS)	23.56710	120.56840	297

GS06(CGS)	23.46560	120.55421	240
GS07(CGS)	23.48290	120.65482	698
GS08(CGS)	25.20372	121.50149	283
GS09(CGS)	25.20860	121.65193	30
GS10(CGS)	25.14615	121.46154	52
GS11(CGS)	25.13356	121.49876	46
GS12(CGS)	25.05303	121.38276	272
GS13(CGS)	25.02000	121.45224	29
GS14(CGS)	24.80321	120.95945	50
GS15(CGS)	24.76664	120.99049	83
GS16(CGS)	24.74787	121.04160	165
GS17(CGS)	23.56115	120.60584	978
GS18(CGS)	23.48498	120.47378	96
GS19(CGS)	25.07225	121.67982	55
GS20(CGS)	24.84251	121.93997	25
GS21(CGS)	24.09730	120.51237	37
GS22(CGS)	24.09087	120.60627	45
GS23(CGS)	24.09459	120.64768	52
GS24(CGS)	24.02523	120.52608	34
GS25(CGS)	23.98651	120.64022	91
GS26(CGS)	23.86984	120.64602	287
GS27(CGS)	23.82475	120.57787	77
GS28(CGS)	23.08098	120.21436	26
GS29(CGS)	23.07513	120.31582	38
GS30(CGS)	23.02048	120.22628	53
GS31(CGS)	23.01890	120.27576	44
GS32(CGS)	23.02578	120.33709	57
GS33(CGS)	22.96442	120.18781	25
GS34(CGS)	22.93922	120.27513	37
GS35(CGS)	22.93552	120.30938	51
GS36(CGS)	24.36204	120.62533	72
GS37(CGS)	24.32857	120.71543	230
GS38(CGS)	24.27980	120.60058	199
GS39(CGS)	24.18441	120.52959	37
GS40(CGS)	24.18123	120.57630	263
GS41(CGS)	23.37755	120.44493	74
GS42(CGS)	23.27322	120.45201	133

GS43(CGS)	23.25716	120.37360	47
GS44(CGS)	23.22224	120.40039	160
GUKN(CWB)	23.64586	120.58878	192
GUKW(CWB)	24.20220	121.00655	777
HANS(CWB)	24.60951	121.68714	194
HCHM(MOI)	24.79252	120.98461	153
HENC(CWB)	22.00393	120.74645	46
HERI(CWB)	25.29444	121.58092	84
HLIU(CWB)	23.79303	120.99417	607
HNES(WRA)	23.94836	120.47914	42
HNSN(CWB)	24.33770	121.30806	2002
HOKN(IES)	23.18838	120.13488	30
HOPN(CWB)	24.17078	120.89488	563
HRGN(CWB)	23.55528	121.40510	257
HSIN(CWB)	24.82775	121.01425	48
HSUE(CWB)	24.28059	121.02645	2629
HUAL(CWB)	23.97538	121.61351	46
HUAN(CWB)	24.14347	121.27262	3421
HUAP(CWB)	24.30900	121.74944	43
HUSI(NLS)	23.56640	119.66941	44
HUWE(CWB)	23.72940	120.28662	28
HUYS(CWB)	24.09233	121.02941	855
ICHU(CWB)	23.36066	120.27930	32
ILAN(CWB)	24.76404	121.75662	28
JHCI(NLS)	23.51372	120.54742	150
JIBE(NLS)	23.74142	119.61336	31
JLUT(CWB)	22.32996	120.62278	29
JNHU(NLS)	24.41708	118.44738	43
JNSA(NLS)	24.50367	118.42175	35
JONP(IES)	23.42297	120.52400	168
JPEI(IES)	23.53160	121.37139	151
JPIN(IES)	23.34108	121.35889	587
JSUI(CWB)	23.49198	121.42389	119
JUNA(NLS)	24.68395	120.87537	45
JYAN(CWB)	24.24247	121.22634	1967
JYGU(NLS)	25.95971	119.97097	81
KAFN(NLS)	23.98758	121.11649	1584

KASH(MOI)	22.61449	120.28835	25
KASU(CWB)	22.81019	120.63298	189
KDNM(MOI)	21.94942	120.78202	58
KMNM(MOI)	24.46382	118.38857	49
KSHI(CWB)	24.77666	121.17603	168
KTES(WRA)	23.62661	120.33428	36
KUAN(CWB)	23.04968	121.16425	252
KULN(IES)	23.33098	120.50702	414
KYIN(CWB)	25.04105	121.08042	32
KZN1(IES)	23.94625	120.69798	130
LANY(CWB)	22.03731	121.55810	347
LAOL(CWB)	22.41192	120.68729	1059
LEYU(NLS)	24.44067	118.23926	76
LGUE(CWB)	22.99290	120.63538	268
LIKN(CWB)	22.75861	120.52790	63
LIUC(CWB)	22.34667	120.36907	62
LIYU(CWB)	24.34306	120.78180	334
LNCH(IES)	22.99458	120.40261	190
LNJS(WRA)	23.75745	120.59215	92
LNKO(CWB)	25.07637	121.37818	266
LONT(CWB)	22.90631	121.13056	203
LSAN(IES)	24.02934	121.18216	1497
LSB0(NLS)	24.15337	120.63422	121
LTUN(CWB)	24.70003	121.77162	28
LUDA(MOI)	22.65809	121.47589	29
LUGU(CWB)	23.75226	120.74769	496
LUKN(CWB)	24.06001	120.43513	24
LUSN(CWB)	24.03519	121.18605	1448
MAJA(NLS)	22.70764	120.65205	211
MATZ(CWB)	26.16939	119.92306	110
MESN(IES)	23.26363	120.82626	925
MFEN(CWB)	24.08216	121.17247	2236
MIAO(CWB)	24.58345	120.81026	171
MINS(IES)	23.27540	120.72090	751
MITO(CWB)	22.79585	120.26315	30
MOTN(IES)	23.20054	121.02685	1606
MZUM(MOI)	26.15710	119.93318	60

NAAO(CWB)	24.44934	121.81021	25
NANK(CWB)	23.10199	120.27439	26
NCKU(CWB)	22.93845	120.27581	40
NDHU(CWB)	23.89724	121.55081	57
NEMN(CWB)	22.90812	120.42008	104
NHSI(CWB)	23.40621	121.45301	137
NIUT(CWB)	24.63478	121.56158	386
NJOU(CWB)	22.50389	120.57141	52
NSAN(CWB)	24.42820	121.38280	1132
NSHE(CWB)	24.22579	120.80090	487
PAKU(IES)	23.91568	120.63603	432
PANG(CWB)	23.56520	119.56374	29
PAOL(IES)	23.10862	120.70287	431
PAOS(CWB)	24.71492	120.95028	96
PEIN(CWB)	22.80107	121.12313	76
PENL(CWB)	24.53884	120.97604	659
PEPU(CWB)	24.01788	121.61034	36
PINT(IES)	23.75606	120.64056	328
PKGM(MOI)	23.57989	120.30550	42
PLAN(CWB)	24.57895	121.08660	1122
PLIM(MOI)	23.97388	120.98200	582
PLIN(CWB)	24.93362	121.71395	271
PTUN(CWB)	22.64985	120.45968	40
PUSN(CWB)	23.96494	120.52011	39
RENI(CWB)	23.45894	120.50857	115
S011(IES)	23.20542	120.33945	67
S012(IES)	23.05947	120.48826	191
S016(IES)	24.17955	120.80286	854
S01R(IES)	23.65527	119.59237	49
S092(IES)	23.18490	120.52847	227
S101(IES)	25.04045	121.61385	59
S103(IES)	23.56437	120.47519	125
S104(IES)	22.82076	121.18938	42
S105(IES)	22.95165	121.11289	699
S106(IES)	23.05079	120.33409	52
S167(IES)	23.95442	120.93410	580
S169(IES)	22.94229	120.50331	145

S170(IES)	23.74596	120.76763	753
S23R(IES)	22.64498	120.60617	94
SALU(CWB)	24.14445	120.57830	297
SAND(CWB)	22.71727	120.64064	203
SANI(CWB)	24.41435	120.76873	335
SANJ(CWB)	25.26079	121.50087	74
SANL(CWB)	23.66448	120.76855	1691
SFON(CWB)	24.93289	121.01016	52
SGAN(CWB)	22.58127	120.34965	30
SGUN(CWB)	24.27163	120.69188	195
SHAN(IES)	23.10886	121.19949	319
SHJU(MOI)	24.84508	120.92195	24
SHMN(NLS)	25.29146	121.56215	46
SHUL(CWB)	23.78761	121.56273	58
SHWA(CWB)	23.02143	120.34781	89
SILN(IES)	23.16038	120.64604	488
SIND(NLS)	24.96680	121.54237	55
SINL(CWB)	22.90829	121.25462	96
SINY(NLS)	23.69649	120.85320	536
SJPU(IES)	23.42854	120.48126	77
SLIN(CWB)	23.81185	121.44140	202
SLNP(CWB)	24.75311	121.63563	491
SONA(CWB)	24.39781	120.98584	1353
SPAO(CWB)	24.20501	121.48486	984
SSUN(CWB)	23.41415	120.37777	44
STAN(CWB)	24.48728	120.87306	767
SUAB(CWB)	24.59391	121.86790	26
SUAN(CWB)	23.47757	120.29988	31
SUAO(CWB)	24.59239	121.86707	24
SUCH(CWB)	24.29107	120.90758	567
SUN1(CWB)	23.88124	120.90835	1035
SYAN(CWB)	23.24800	120.98675	2327
TACH(MOI)	24.29084	120.53513	33
TAIP(CWB)	25.03452	121.67317	527
TANS(CWB)	25.18150	121.42689	30
TAPE(IES)	23.12557	121.23087	303
TAPO(IES)	23.12706	121.23741	419

TAPU(IES)	23.25080	120.58541	669
TASI(NLS)	23.72027	120.18881	38
TATA(CWB)	23.48140	120.88705	2651
TAYN(NLS)	23.15934	120.76419	645
TCMS(NML)	24.79798	120.98739	77
TEGS(CWB)	24.35621	120.65498	255
TENC(IES)	23.27779	120.91567	2341
THAI(CWB)	24.60712	121.29559	1520
TIAN(NLS)	24.46503	120.94071	511
TKJS(WRA)	23.68799	120.38982	41
TMAL(CWB)	22.64892	120.95987	1189
TMAM(MOI)	22.61608	121.00748	58
TNML(NML)	24.79795	120.98734	77
TOFN(CWB)	24.66204	120.92480	128
TSHI(CWB)	25.25691	121.63276	50
TSIO(CWB)	24.47279	120.70410	63
TSLN(CWB)	23.63432	120.71938	1602
TTSH(IES)	22.74713	121.14762	48
TTUN(CWB)	22.76455	121.08070	100
TUCN(CWB)	24.57484	121.49613	394
TUNH(IES)	23.07516	121.30022	358
TUNM(CWB)	23.96521	121.49358	195
TUNS(CWB)	23.31724	120.40404	54
TWTF(CTL)	24.95356	121.16450	201
W021(IES)	23.53568	120.54951	182
W029(IES)	23.54079	120.66425	1065
W030(IES)	23.47410	120.69552	1312
WANC(CWB)	23.18684	120.52633	341
WANL(CWB)	25.16938	121.63756	370
WANS(CWB)	23.60750	120.88519	942
WDAN(CWB)	22.60606	120.50431	36
WFEN(CWB)	24.04194	120.69947	102
WIAN(NLS)	23.56753	119.48080	44
WIPN(CWB)	24.67463	121.05855	210
WUFN(IES)	24.04278	120.69939	109
WUKU(CWB)	25.11728	121.40066	225
WULI(NLS)	24.35228	121.30846	1790

WULU(NLS)	23.16926	121.04147	928
WUST(CWB)	23.20524	120.36817	89
YAME(CWB)	24.90845	121.18529	218
YENC(IES)	22.76351	120.37615	70
YENL(CWB)	23.90350	121.60184	88
YENL(CWB)	23.90350	121.60184	88
YM01(IES)	25.17888	121.53954	710
YM02(IES)	25.14838	121.56069	545
YM03(IES)	25.14661	121.60490	431
YM04(IES)	25.18760	121.58547	368
YM05(IES)	25.16400	121.56548	744
YMSM(MOI)	25.16571	121.57405	784
YNTS(CWB)	24.86174	121.77893	487
YSAN(CWB)	23.14655	120.08598	23
YULI(CWB)	23.34093	121.30113	208
YUNL(IES)	23.88388	120.79857	250
YUSN(CWB)	23.48730	120.95914	3879
ZEND(CWB)	22.94327	120.21756	35
ZWEN(CWB)	23.21974	120.49734	172

Institution^a : Central Weather Bureau (CWB), Institute of Earth Sciences (IES),
Central Geological Survey (CGS), National Land Surveying and Mapping (NLS),
Ministry of Interior (MOI), Water Resources Agency (WRA), National
Measurement Laboratory (NML), Chunghua Telecom Laboratory (CTL)

Appendix 2

```

!-----<*>-----C
! NAME                Draw Typhoon From ECMWF      C
! GENERIC NAME        --"--                      C
! MODIFIED BY         Ricky                       C
! PURPOSE             TO READ THE ECMWF AND PLOT IT
! CALLING SEQUENCE    CALL DATEIN(DA,NY,MM,ND,NH,NM,SEC)
! INPUT FILES         ****.TXT                   C
! OUTPUT FILES        NONE                       C
!-----<*>-----C

```

Program draw

use fml

use fgl

implicit none

integer :: i,n,k,yyyi,mi,di,yyye,me,de,sgstart,yyy0,m0,d0

integer*4 :: all

real*8 :: mjd,mjdi,mjde

character :: name,yes



! READ FORMAT FROM MATFOR

type (mfArray) ::

x,y,z,str,air,x1,y1,z1,x2,y2,z2,xa,ya,za,xa1,ya1,za1,za2,za3,ht,h,hsinchu,color
za3=mfOnes(22,22)*0

!call msGDisplay(air,'air',za3,'za3')

n=0

i=1

! THE GRID IS 22*22

k=484

! THE FREQUENCY IS 6 HR

all=484*7180 !7180-->200604201102,5844-->200604201003

str = mfFileDialog("", "*.txt")

air = mfLoadAscii(str)

```

! SG LOCATION
    hsinchu = (/120.9855d0,24.7926d0/)

! DRAW FIGURE
    call msFigure(1)

! READ FORMAT OF ATMOSPHERE
do n=0,(all-k),k
    za=mfMatSub(air,mf(n+1).to.mf(n+k).step.1,3)
    za1=mfReshape(za,22,22)
    za2=t.za1
    za3=za3+za2*k/all
end do
    yes = 'y'
!call msGDisplay(za,'za',za2,'za2',za3,'za3')

! DRAW TYPHOON FORM YYYYMMDD TO yyyymmdd
do while((yes .EQ. 'y') .OR. (yes .EQ. 'Y'))
    write(*,*) 'input start day: yyyy mm dd'
    read(*,*) yyyi,mi,di
    write(*,*) 'input end day: yyyy mm dd'
    read(*,*) yyye,me,de
    call DATEIN(mjd,yyyi,mi,di,0,0,0d0)
    mjdi= mjd
    !write(*,*) 'mjd1=',mjd,mjdi
    call DATEIN(mjd,yyye,me,de,0,0,0d0)
    mjde= mjd
    !write(*,*) 'mjd2=',mjd,mjde
    call DATEIN(mjd,2006,4,1,0,0,0d0)
    sgstart=mjd

    call DATEOUT(mjdi,yyy0,m0,d0)
    ! write(*,*) 'MJD, YYYY, MON, DAY = ',mjdi,yyy0,m0,d0
    !write(*,*) mjdi,mjde,sgstart,mjd,(mjdi-sgstart)*k*4,(mjde-sgstart)*k*4,k

do n=(mjdi-sgstart)*k*4,(mjde-sgstart)*k*4-k,k
    if (i==2) then

```

```

        call msViewPause()
    end if
    x=mfMatSub(air,mf(n+1).to.mf(n+k).step.1,2)
    x1=mfReshape(x,22,22)                !1*(m*n)-->m*n
    x2=.t.x1                             !Transpose

    y=mfMatSub(air,mf(n+1).to.mf(n+k).step.1,1)
    y1=mfReshape(y,22,22)
    y2=.t.y1

    z=mfMatSub(air,mf(n+1).to.mf(n+k).step.1,3)
    z1=mfReshape(z,22,22)
    z2=.t.z1
    z2= z2 - za3
    !call msMeshgrid(mfOut(x2,y2),x1,y1)
    call msSubplot(1,2,1)
    call msClearSubplot()
    call msFastPcolor(z2,mf((/109.5d0,141d0,40.5d0,9d0/)))
    call msCircle(hsinchu, mf((/1,0,0/)), mf((/1d0/)))
! call msCircle(hsinchu, mf((/0,1,0/)), rad2)

    call msHold('on')
    h = mfContour(x2,y2,z2)

    call msGSet(h,mf('label'),mf('on')) !Draw the label on Contour
    call msHold('on')
    call msAnnotation(mf('HS'),mf((/120.90,24.90,0.00/)),mf((/0,0,1/)),mf(10))
    !call msGDisplay(air,'air',x2,'x2',y2,'y2',z2,'z2',x3,'x3',y3,'y3',z3,'z3')

!Create 2D coastline data
call msCreateCoastlineData( mfOut(x,y), 110, 141, 9, 40 )

call msTitle('Atmosphere anomaly')
call msYLabel('Latitude')
call msXLabel('Longitude')

!plot 2D linear graph
call msPlot(x,y)

```

```

!call msGetCurrentDraw()

call msSubplot(1,2,2)
call msColorbar('on')
call msTitle('Atmosphere anomaly')
call msXlabel('Longitude')
call msYlabel('Latitude')
call msSurfc(x2,y2,z2)

call msDrawNow()
i=i+1
end do ! n
write(*,*) 'Do you want to restart? (Y or N)'
read(*,*) yes
end do ! while

!call msPlot(x2,y2)
call msViewPause()
call msFreeArgs(x, y ,z, str, air, x1, y1, z1,x2,y2,z2)

```



end Program draw

SUBROUTINE DATEIN(DA,NY,MM,ND,NH,NM,SEC)

```

!-----<*>-----C
! NAME                DATEIN                C
! GENERIC NAME        --"--                C
! ORIGINAL FROM       EG & G - WASC  VIA RON KOLENKIEWICZ
! VERSION              8305.1                C
! MODIFIED BY         ERRICOS C. PAVLIS        C
!                     DEPT. OF GEODETIC SCI. & SURVEYING
!                     THE OHIO STATE UNIVERSITY
!                     1958 NEIL AVE.,          C
!                     440 COCKINS HALL,       C
!                     COLUMBUS OHIO  43210    C
!                     TEL. (614) - 422-6753   C
! PURPOSE              TO COMPUTE THE MJD BASED ON THE VIGESIMAL
!                     DATE .                  C

```

```

! CALLING SEQUENCE  CALL DATEIN(DA,NY,MM,ND,NH,NM,SEC)
!  SYMBOL  TYPE  DESCRIPTION  C
!  NY      I    INPUT - YEAR (2002 --> 2002)  C
!  MM      I    INPUT - MONTH (MAY --> 5)  C
!  ND      I    INPUT - DAY OF THE MONTH  C
!  NH      I    INPUT - HOURS  C
!  NM      I    INPUT - MINUTES  C
!  SEC     DP   INPUT - SECONDS  C
!  DA      DP   OUTPUT - MJD OF NY/MM/ND - NH:NM:SEC
! INPUT FILES      NONE  C
! OUTPUT FILES     NONE  C
!-----<*>-----C

```

IMPLICIT REAL*8(A-H,O-Z)

DIMENSION MONTH(13)

DATA MONTH/0,31,59,90,120,151,181,212,243,273,304,334,365/

DA=365*(NY-1958)+(NY-1957)/4+104+ND+MONTH(MM)+NH/24.D0+NM/1440.
D0+SEC/86400.D0

IF (NY.EQ.4*(NY/4).AND.MM.GT.2) DA=DA+1

!.....CHANGE DODS TIME TO MJD

DA = DA + 36099.D0

! write(*,*) DA,NY,MM,ND,NH,NM,SEC

RETURN

END

SUBROUTINE DATEOUT(DA,NY,MM,ND)

!-----<*>-----C

! C

! NAME DATEIN C

! GENERIC NAME --"-- C

! ORIGINAL FROM EG & G - WASC VIA RON KOLENKIEWICZ

! VERSION 8305.1 C

! MODIFIED BY ERRICOS C. PAVLIS C

! DEPT. OF GEODETIC SCI. & SURVEYING

! THE OHIO STATE UNIVERSITY

! 1958 NEIL AVE., C

! 440 COCKINS HALL, C

```

!           COLUMBUS OHIO  43210      C
!           TEL. (614) - 422-6753      C
! PURPOSE           TO COMPUTE THE MJD BASED ON THE VIGESIMAL
!           DATE .                      C
! CALLING SEQUENCE  CALL DATEIN(DA,NY,MM,ND,NH,NM,SEC)
!  SYMBOL  TYPE  DESCRIPTION          C
!  NY      I    OUTPUT - YEAR (2002 --> 2002)
!  MM      I    OUTPUT - MONTH (MAY --> 5)
!  ND      I    OUTPUT - DAY OF THE MONTH
!  DA      DP   INPUT - MJD OF NY/MM/ND - NH:NM:SEC
! INPUT FILES      NONE                C
! OUTPUT FILES     NONE                C
!-----<*>-----C

```

```

IMPLICIT REAL*8(A-H,O-Z)

```

```

INTEGER*4 :: y1,m1,k,y2,m2

```

```

y1 = ((DA-15078.2)/365.25)

```

```

y2 = y1*365.25

```

```

m1 = ((DA-14956.1-y2)/30.6001)

```

```

m2 = m1*30.6001

```

```

ND = DA-14956-y2-m2

```

```

if ((m1 .EQ. 14 ) .OR. (m1 .EQ. 15)) then

```

```

k=1

```

```

else

```

```

k=0

```

```

end if

```

```

NY = y1+k+1900

```

```

MM = m1-1-k*12

```

```

! write(*,*) DA,NY,MM,ND

```

```

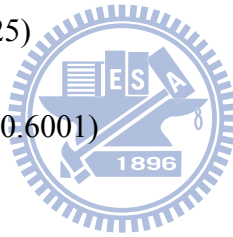
RETURN

```

```

END

```



Curriculum Vitae

Kao, Ruei-Chi (Kao, Ricky)

Gender: Male

Address: 2F. No. 539-3, Sec. 2, Jingguo Rd. North Dist., Hsinchu City 300,
Taiwan (R.O.C.)

Phone: +886-3-5751202 (office)

Fax: +886-3-5734967 (office)

Email: ricky.kao@gmail.com

WWW: <http://space.cv.nctu.edu.tw>

Date of birth: February 24, 1976

Place of birth: Taipei city, Taiwan

Education:

2006~2011 National Chiao Tung University, Taiwan, R.O.C.

PH.D. "Dept of Civil Engineering"

1999~2001 National Chiao Tung University, Taiwan, R.O.C.

MS, "Dept of Civil Engineering"

1995~1999 National Cheng Kung University, Taiwan, R.O.C.

B.S. "Dept of Surveying Engineering"

Licensure and Professional experience:

Licensed of Technician Survey, Taiwan, R.O.C. (2006)

Licensed of ISO 17025 (Certificate in Laboratory Quality Management, 2010)

Research Assistant, Taiwan Ocean Research Institute (2001)

Data processing of TOPEX/Poseidon

Research Assistant, National Space Program Office (2002-2005)

Design the Planning and Scheduling System of Formosat-2

Research Assistant, National Space Organization (2005-2006)

Data processing of Formosat-2

Deputy Engineer, Industrial Technology Research Institute (2001-2011)

Data processing of Superconducting Gravimeter and Absolute Gravimeter

Publications:

- (1) Hwang, C. and R. Kao, 2002. TOPEX/POSEIDON-derived space-time variations of Kuroshio Current: applications of a gravimetric geoid and wavelet analysis, *Geophysical Journal International*, 151, pp. 835-847. (IF=2.353)
- (2) Hwang, C., C. R. Wu and R. Kao, 2002. The kinematics of mesoscale eddies from TOPEX/POSEIDON altimetry, *Proc. International Workshop on Satellite Altimetry for Geodesy, Geophysics and Oceanography*, pp. 183-190 Wuhan, Sep 8-13.
- (3) Hwang, C, R. Kao, C. C. Cheng, J. F. Huang, C. W. Lee , and T. Sato, 2009. Results from parallel superconducting and absolute gravimetric observations and GPS at the Hsinchu (HS) station of GGP , Taiwan, *Journal of Geophysical Research-solid earth*, Vol. 114, B07406. Doi: 10.1029/2008JB006195 (IF=3.147)
- (4) Kim, K. D., J. W. Kim, J. Neumeyer, R. Kao, C. Hwang, H. J. Park, I. Woo, Y. W. Lee, 2009. Determination of Gravity at MunGyung superconducting gravity at Observatory , Korea. *Geosciences Journal Korea*, Vol. 13, No.2, 141-150. DOI: 10.1007/s12303-009-0013-5 (IF=0.412)
- (5) Lee, C. W., W. C. Hsieh, J. F. Huang, R. Kao, M. H. Peng, C. Hwang, J. Z. Chen, 2009. Study on Absolute Gravity Monitoring Stations for Taiwan Gravity Datum, *Journal of Cadastral Survey*, Vol. 28 No.3, pp. 51-58.
- (6) Lan, S. C., T. T. Yu, C. Hwang, and R. Kao, 2011. An Analysis of Mechanical Constraints when Using Superconducting Gravimeters for Far-Field Pre-Seismic Anomaly Detection, *Atmospheric and Oceanic Sciences*. Doi: 10.3319/TAO.2010.11.12.01(IF=0.594)
- (7) Lan, S. C., T. T. Yu, C. Hwang, and R. Kao, 2011. Analysis of the Constraints in Using Superconducting Gravimeters for Far-Field Pre-seismic Anomaly

Detection, Terrestrial, Atmospheric and Oceanic Sciences, in press. (IF=0.643)

Conference papers

- (1) Hwang, C., S. A. Chen and R. Kao, 2000. Kuroshio Upstream Dynamics Experiment: satellite altimeter observations of Kuroshio upstream, Proceedings of Ocean Science Meeting of NSC, pp. 83-95, Taipei, Taiwan. (in chinese)
- (2) Hwang, C., R. Kao, 2002. Kuroshio Upstream Dynamics Experiment, KUDEX—project 5: TOPEX/POSEIDON-derived on KUDEX (3), Workshop for 2002 Oceanographic Research Programs, pp. 3-9, Taitung, Taiwan. (in chinese)
- (3) Liu S. J., P. T. Lin, H. Y. Chen, Y. Y. Lee, R. Kao, A. M. Wu, 2003. Qualification Test of ROCSAT-2 Image Processing System, ACRS 2003, pp. 540.
- (4) A. M. Wu, Y. Y. Lee, P. Kuo and R. Kao, 2003. ROCSAT-2 Imaging Planning And Scheduling, The first Taipei international conference on digital earth, Taipei, Taiwan.
- (5) Chen C. S., C. H. Wang and R. Kao, 2006. The Study of disaster management for the earth quake of south Asia by applying the remote sensing resource of FORMOSAT-2, The 25th Conference on Surveying and Geomatics: 2006, Taoyuan, Taiwan, pp. 697. (in chinese)
- (6) C. H. Wang, T. K. Yeh, C. S. Chen, C. Hwang, R. Kao, C. W. Lee, 2007. Evaluate the impact of ocean loading by using GPS and Superconducting Gravimeter, The 26th Conference on Surveying and Geomatics: 2007, Yilan, Taiwan, pp. 399-406. (in chinese)
- (7) Kao, R., M. H. Peng, W. C. Hsieh, C. W. Lee, C. Hwang, C.C. Cheng, J. F. Huang, Evaluation of the superconducting gravimeter SG048, Saint Petersburg, Russia, 20-23 August, 2007.
- (8) Kao, R., C. C. Cheng, C. W. Lee, C. Hwang, 2007. Analysis of SG T048 observations at Hsinchu: signal and noise, First Asia Workshop on superconducting gravimetry, Hsinchu, Taiwan, pp. 23.
- (9) Kao, R., C. C. Cheng, C. W. Lee, F. Y. Xiao, C. W. Chang, 2007. The earthquake models of superconducting gravity changes, 5th Across-the-strait Geomatics Conference, Hsinchu, Taiwan, p.p. 83. (in chinese).
- (10) Hsieh, W. C., C. W. Lee, R. Kao, M. H. Peng, C. Hwang, M. Yang, F. Masson, and N. Le Moigne, 2008. Absolute gravity measurements in Taiwan, Asia Oceania Geosciences Society, Korea, June 16-20.
- (11) Kao, R., C. Hwang, C. W. Lee, M. H. Peng, W. C. Hsieh, 2008. Correction and application of Superconducting Gravimeter (SG) at National Gravity Datum

- Service, The 27th Conference on Surveying and Geomatics: 2008, Tainan, Taiwan, pp. 40.
- (12) Peng, M. H., C. W. Lee, W. C. Hsieh, R. Kao, J. F. Huang, C. Hwang, 2008. Evaluation of ocean tide loading effects for gravity: the SG measurements at Hsinchu, Taiwan, The 27th Conference on Surveying and Geomatics: 2008, Tainan, Taiwan, pp. 41.
- (13) Kao, R., C. Hwang, C. W. Lee, M. H. Peng, W. C. Hsieh, 2009. Atmospheric pressure effect of SG measurements, The 28th Conference on Surveying and Geomatics: 2009, Taoyuan, Taiwan.
- (14) Kao, R., C. Hwang, C. W. Lee, 2010. Atmosphere Loading effects of SG48 in Hsinchu (HS), 2nd Asia Workshop on Superconducting Gravimetry, Taipei.
- (15) Cheng, C., R. Kao, N. Hsieh, and C. Hwang, 2010. Monitoring the gravity changes of seismic deformation by the absolute gravimetric network, 2nd Asia Workshop on Superconducting Gravimetry, Taipei.
- (16) Hwang, C., C. Cheng, J. Huang and R. Kao, 2010. Superconducting and absolute gravity observations for geodynamic applications, APSG 2010, Shanghai, China.
- (17) Kao, R., C. Hwang, C. W. Lee, M. H. Peng, W. C. Hsieh, 2010. Using Superconducting Gravimeter Data to Promote and Apply in National Gravity Datum Service, The 29th Conference on Surveying and Geomatics : SG2010, Taipei, Taiwan, September 2-3.
- (18) Kao, R., C. Hwang, C. W. Lee, M. H. Peng, W. C. Hsieh, 2010. Taiwanese Orography From Absolute Gravimetry: Comparison of Observation and Model, The 29th Conference on Surveying and Geomatics : SG2010, Taipei, Taiwan, September 2-3.